Forschungszentrum Jülich
in der Helmholtz-Gemeinschaft

Institute of Bio- and Nanosystems

Interfacial Electrochemistry and in situ SEIRAS investigations of Self-Assembled Organic Monolayers on Au/Electrolyte Interfaces

Bo Han

Jül-4236

Interfacial Electrochemistry and in situ SEIRAS Investigations of Self-Assembled Organic Monolayers on Au/Electrolyte Interfaces

Bo Han

Berichte des Forschungszentrums Jülich; 4236
ISSN 0944-2952
Institute of Bio- and Nanosystems
D 82 (Diss., RWTH Aachen, 2006)

Zu beziehen durch: Forschungszentrum Jülich GmbH, · Zentralbibliothek, Verlag
D-52425 Jülich · Bundesrepublik Deutschland
☎ 02461/61-5220 · Telefax: 02461/61-6103 · e-mail: zb-publikation@fz-juelich.de

Abstract

Electrified solid/liquid interfaces offer unique opportunities for the fabrication and characterization of 2D supramolecular nanostructures. The combination of macroscopic electrochemical methods with structure sensitive techniques, such as scanning probe microscopy (SPM) or vibrational spectroscopy enables the development of a detailed knowledge on structure and functionality of the created molecular assemblies. In the present dissertation, the steady state and dynamic properties of self-assembled adlayers of trimesic acid and thioalkylviologens were investigated on gold/electrolyte interfaces employing surface enhanced IR absorbance spectroscopy (SEIRAS) in combination with various electrochemical methods.

The double layer properties of the Au/aqueous electrolyte interface were investigated first for massive Au(111) single crystal electrodes and Au(111-20 nm) film electrodes in contact with 0.1 M H_2SO_4 and 0.1 M $HClO_4$. Cyclic voltammetry revealed that the response of the film electrodes resembles that of a massive Au (111) electrode with a low step density. The potential-dependent adsorption of anions and interfacial water was investigated in detail by in situ SEIRAS.

As the second topic, the adsorption and phase formation of trimesic acid (TMA) on Au(111) and Au(111-20 nm) electrodes were comprehensively investigated by electrochemical techniques, scanning tunneling microscopy and SEIRAS. Depending on the applied electrode potential, TMA molecules form several highly ordered 2D adlayers: two physisorbed phases, one characterized by a hexagonal honeycomb pattern and the other by close-packed linear-dimers of planar oriented molecules; and one stripe-like chemisorbed adlayer of perpendicularly oriented molecules. Weakly hydrogen-bonded, strongly hydrogen-bonded and isolated water species are co-adsorbed. The potential-induced formation of chemisorbed TMA starts with a fast orientation change from planar, physisorbed molecules to tilted and/or perpendicular in a disordered chemisorbed phase. Subsequently, the chemisorbed TMA molecules align slowly into the highly ordered stripe-like structure. Both substrate/adsorbate and intermolecular hydrogen-bonding interactions are strongly dependent on the electrode potential.

The comparison with benzoic acid (BA) and isophthalic acid (IA) shows that each TMA molecule is chemisorbed via one carboxylate group in an “atop” configuration, while the two other -COOH side groups are directed towards the electrolyte and therefore available for further hydrogen-bonding between neighboring TMA molecules. The orientation of BA and IA molecules in the respective adlayers showed a similar potential dependence as TMA.

The third topic of the dissertation is focused on the self-assembly and interfacial reactivity of redox-active thioalkylviologens immobilized on gold/electrolyte interfaces. Voltammetric experiments revealed two one-electron redox processes of the surface confined adlayer, the reduction of the viologen dication V^{2+} to the radical cation $V^{\bullet+}$, and the reduction of the radical cation to the neutral species V^0. The first redox process $V^{2+} \leftrightarrow V^{\bullet+}$ is reversible, while the second redox process $V^{\bullet+} \leftrightarrow V^0$ is only quasi reversible. A complete monolayer of V^{2+} exhibits a sandwich-like structure: the van der Waals interaction between the alkyl chains leads to two well-ordered hydrophobic layers, with the redox-active bipyridinium layer enclosed in between. The alkyl chains are aligned in an all-trans configuration in a tilted orientation with respect to the surface normal. However, they exhibit conformational disorder up to some extent. The long axis of the central bipyridinium unit is also tilted. The alignment of V^{2+} is stabilized by inter-planar $\pi - \pi$ and coulombic interactions. The SAM of $V^{\bullet+}$ is composed of coexisting monomers $V^{\bullet+}$ and dimers $(V^{\bullet+})_2$. The alignment of $V^{\bullet+}$ is stabilized by a strong vibronic coupling within the dimers as well as the $\pi - \pi$ stacking between the monomers. The dimerization and the alignment are both favored by the more tilted bipyridinium units with an increase of the alkyl chain lengths.

Attempts to investigate the kinetic behavior of the redox electron-transfer process $V^{2+} \rightarrow V^{\bullet+}$ lead to qualitative conclusions. The overall redox process starts with an interfacial electron transfer (tunneling mechanism) from the electrode to the V^{2+} moiety through the alkyl chains. In a subsequent slow process, the dimerization of $V^{\bullet+}$, the delocalization of the radical electrons, and the migration of ClO_4^- take place simultaneously. The overall rate of the redox reaction is determined by the dissociation of the ion-pair complex and the migration of the ClO_4^- anions.

Kurzfassung

Elektrochemische fest/flüssig Grenzflächen eröffnen neuartige Möglichkeiten zur Herstellung und Charakterisierung 2D supramolekularer Nanostrukturen. Die Kombination makroskopischer elektrochemischer Methoden mit strukturensitiven in situ Techniken, wie z.B. Rastersondenmikroskopie (RSM) oder die Familie der Schwingungsspektroskopien ermöglicht die Entwicklung detaillierter Kenntnisse zu Struktur und Funktionalität der hergestellten molekularer Assemblies. In der vorliegenden Dissertation wurden steady state und dynamische Eigenschaften selbstorganisierter Adsorbatschichten von 1,3,5-Tricarboxylbenzensäure (TMA) und einer Serie von Thioalkyviologenderivaten an Gold/Elektrolyt Grenzflächen unter Verwendung von oberflächenverstärkter Infrarotspektros-kopie (SEIRAS) in Kombination mit verschiedenen elektrochemischen Methoden studiert.

Zunächst wurden die Eigenschaften der elektrochemischen Doppelschicht Au/wässriger Elektrolyt für massive Einkristalle Au(111) und Goldfilmelektroden Au(111-20 nm) im Kontakt mit 0.1 M H_2SO_4 und 0.1 M $HClO_4$ studiert. Messungen mittels zyklischer Voltammetrie zeigten, daß die präparierten Filmelektroden ähnliche elektrochemische Eigenschaften wie massive Au(111) Einkristallelektroden mit einer kleinen Stufendichte aufweisen. Die Potentialabhängigkeit der Anionenadsorption und von Grenzflächenwasser wurde mittels SEIRAS studiert.

Als zweite Fragestellung wurden die Adsorption und Strukturbildung von 1,3,5-Tricarboxylbenzensäure an Au(111) und Au(111-20 nm) Elektroden mittels elektrochemischer Techniken, Rastertunnelmikroskopie und SEIRAS untersucht. TMA Moleküle bilden, abhängig vom angelegten Elektrodenpotential, mehrere wohlgeordnete 2D Adsorbatschichten: Zwei physisorbierte Phasen, eine hexagonale Honigwabenstruktur und eine dichte Packung linearer Dimere von planar orientierten Molekülen sowie eine chemisorbierte Streifenphase senkrecht orientierter Moleküle. Die spektroskopischen Untersuchungen zeigen, dass sowohl schwach als auch stark gebundene Wasserspezies und isolierte Wassermoleküle co-adsorbiert sind. Die potentialinduzierte Bildung der chemisorbierten Adsorbatschicht beginnt mit einem Wechsel der physisorbierten, planar angeordneten Moleküle in einer gekippte oder senkrechte Orientierung. In einem Folgeschritt assemblieren die chemisorbierten TMA Moleküle in eine geordnete Streifenstruktur. Diese Struktur wird stabilisiert durch Substrat/Adsorbat Wechselwirkungen sowie durch inter-molekulare Wasserstoffbrückenbindungen.

Der Vergleich mit Benzensäure (BA) und 1,3-Dicarboxylbenzensäure (IA) ergab, daß TMA über eine deprotonierte Carboxylatgruppe in atop Position chemisorbiert ist, während die anderen beiden Carboxylgruppen in Elektrolytrichtung orientiert sind, und daher Wasserstoffbrücken zu benachbarten TMA Molekülen ausbilden können. Adsorbatschichten von BA und IA auf Au(111) bzw. Au(111-20 nm) Elektroden zeigen eine ähnliche Potentialabhängigkeit im elektrischen Feld wie TMA.

Eine dritte Fragestellung fokussierte auf die Selbstorganisation und Grenzflächenreaktivität von redox-aktiven Thioalkylviologenderivaten immobilisiert an Gold/Elektrolyt Grenzflächen. Aus voltammetrischen Experimenten konnten zwei Einelektronenredoxprozesse der immobilisierten Adsorbatschichten identifiziert werden. Diese können der Reduktion des Viologendikations V^{2+} zum Radikalkation $V^{\bullet+}$, sowie der Reduktion des Radikalkations zur neutralen Spezies V^{0} zugeordnet werden. Eine vollständig ausgebildete Monoschicht von V^{2+} zeigt eine „sandwich"-artige Struktur: Die „stacking" Schicht der redoxaktiven Bipyridiniumgruppen wird eingeschlossen von zwei parallelen Reihen von Alkylketten. Die Alkylketten sind präferentiell in einer all-trans Konformation ausgerichtet, zeigen eine schwache Unordnung und sind verkippt zur Oberflächennormalen. Die lange Achse der zentralen Bipyridiniumeinheit ist ebenfalls verkippt. Die Anordnung der V^{2+} Spezies wird bestimmt durch Substrat-Adsorbat- sowie interplanare $\pi - \pi$ „stacking" und Coulomb-Wechselwirkungen. Die Adsorbatschicht der Radikalcationen $V^{\bullet+}$ besteht aus Monomeren $V^{\bullet+}$ und Dimeren $(V^{\bullet+})_2$. Die Ausrichtung der $V^{\bullet+}$ Spezies ist stabilisiert durch eine starke Schwingungskopplung zwischen den Dimeren als auch durch $\pi - \pi$ „stacking" zwischen den Monomeren. Die Dimerisation und die Ausrichtung der Thioalkylviologen-Spezies werden unterstützt durch den Kippwinkel der Bipyridineinheit sowie durch die zunehmende Länge der Alkylketten.

Versuche zum Studium der Kinetik des Elektronentransferprozesses $V^{2+} \rightarrow V^{\bullet+}$ führten zu den folgenden qualitativen Schlüssen: Der Gesamtprozess wird initialisiert durch den Elektronentransfer (Tunnelmechanismus) von der Elektrode zur Viologengruppe durch die Alkylketten. Daran schließt sich eine Serie von langsamen Prozessen an: die Dimerisation von $V^{\bullet+}$, die Delokalisierung des Radikalelektrons und die Migration der Perchlorationen. Die effektive Rate des Gesamtprozesses wird bestimmt durch die Dissoziation eines Ionenpaarkomplexes und die Migration der Perchlorationen.

Contents

Chapter 1. Introduction

1.1 2D Supramolecular Self-Assembled Structures

1.1.1 From molecules to supramolecular assemblies

Defined by J. M. Lehn as the “chemistry of the inter-molecular bonds, which involves recognition, transformation and translocation of information” [1], *Supramolecular Chemistry* represents the concept of bringing molecules together to form the secondary structures beyond elementary structures of individual molecules. Rapidly expanding at the interdisciplinary frontiers of chemical science with physical and biological phenomena, supramolecular chemistry has opened up a broad path to create and fabricate diverse nanoscale architectures via *recognition* by molecules themselves, which implies the storage and read-out of molecular *information*, such as the complementary interaction sites, binding units, and molecular fragments within an individual molecular structure [1].

Derived from the concepts of supramolecular chemistry, “*Self-assembly*” of chemical species is defined as "the spontaneous assembly of molecules into structured, stable, non-covalently bound aggregates" [2], or "the non-covalent interaction of two or more molecular subunits to form an aggregate whose novel structure and properties are determined by the nature and positioning of the components" [3]. Such spontaneous construction of supramolecular architectures from molecular constituents is usually achieved by selective and directional non-covalent interactions [4], which involve intermolecular electrostatic interactions (positive/negative, charge/dipole, dipole/dipole, π-stacking, and metal ion/ligand coordination, etc.), hydrogen-bonding or van der Waals interactions [1]. The relative intensities of intermolecular interactions are quantitatively sketched, as an example in Fig. 1-1, relative to several types of hydrogen-bonds.

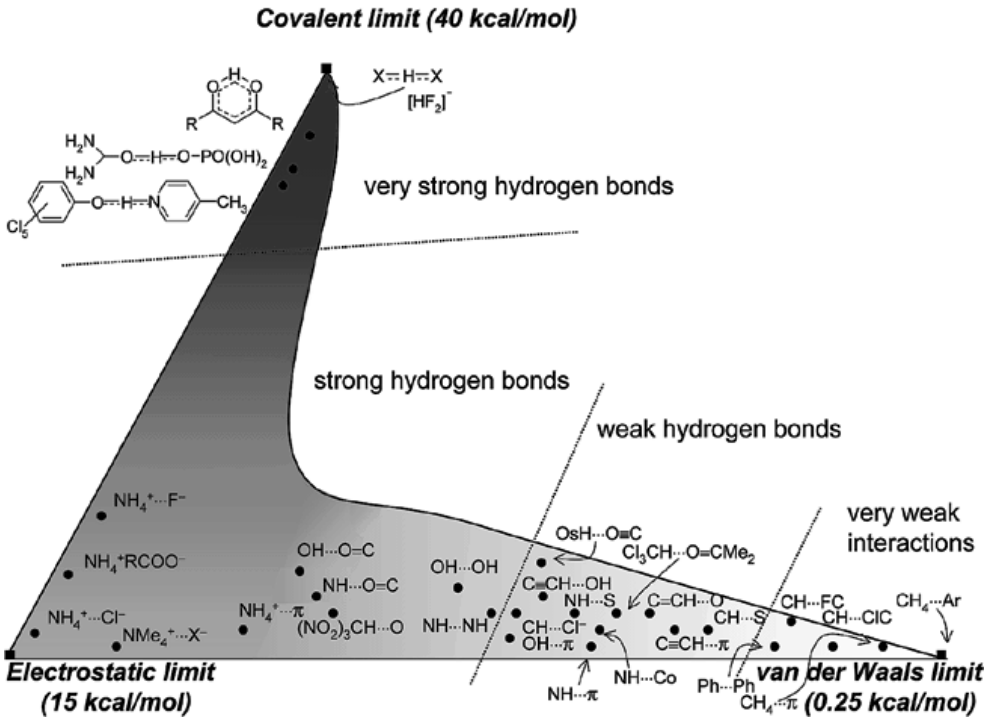

Fig. 1-1: Classification of different hydrogen-bonding interactions, with respect to the bond energy of electrostatic, van der Waals, and covalent interactions [5].

Various types of supramolecular self-assemblies have been revealed both in life sciences (e.g., double helix crosslinking of DNA, protein folding, formation of lipid bilayers), and in chemical systems (e.g., crystallization, formation of vesicles, adsorption on surfaces) [2]. Although the understanding of supramolecular self-assembly was initially developed from 3D crystal or solution phases, most of the recent investigations focus on 2D supramolecular self-assembly on surfaces or interfaces, whose formation and stability depend not only on intermolecular forces, but also on the interactions between the individual component molecules and the solid substrate or support [6]. One of the most important applications of 2D supramolecular self-assembly is in the *"bottom-up"* approach for fabricating nanoscale patterns and devices on 2D substrates.

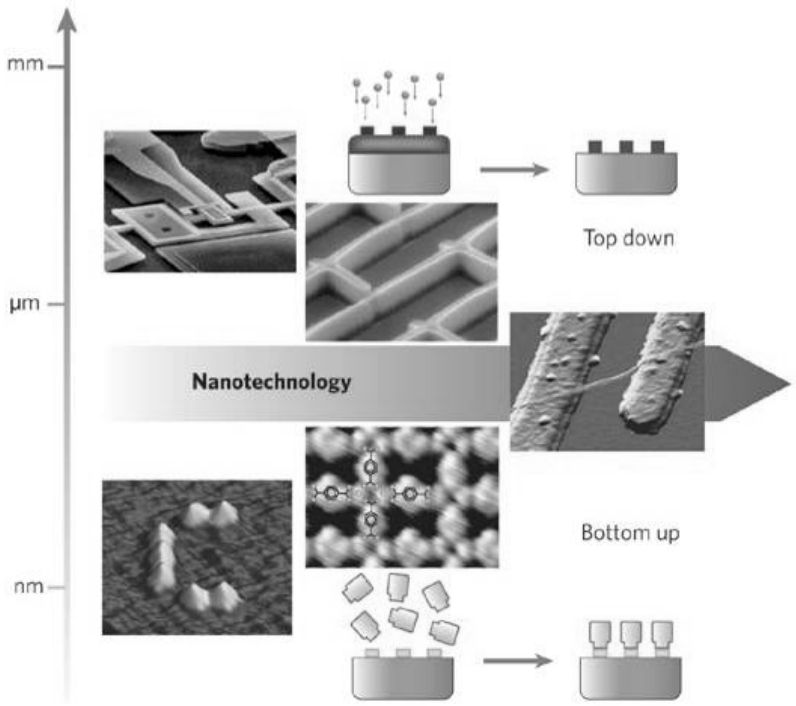

Fig. 1-2: "Top-down" and "Bottom-up" approaches for controlling matter at the nanoscale [4].

1.1.2 2D fabrication

The two basic approaches for creating 2D patterns and devices are the "top-down" and "bottom-up" techniques (see Fig. 1-2). Compared with "top-down" methods to "imposed" a structure down to a sub-100 nm range, "bottom-up" methods aim to guide the assembly of small molecular constituents into organized surface structures through ordering processes inherent in the manipulated system, such as the self-assembly of supramolecular building blocks. The bottom-up construction of molecular nanostructures has several unique advantages due to the nature of individual molecules [7,8]:

i) Molecules are essentially nanoscale objects (1 ~ 100 nm), which may play an important role as building blocks in future nanoelectronic devices (Moore's law [9]);

ii) High reproducibility due to self-assembly and recognition;

iii) Dynamical stereochemistry for possibilities of switching;

iv) Versatile implementation of localized functions with optical, electrical, magnetic, ion-binding, etc. properties, leading to applications in molecular optics, electronics, magneto, and ionics etc. [1].

The parameters crucial for 2D supramolecular fabrication are the surface mobility of molecules, their lateral interactions and their coupling to the substrate atomic lattice, depending on the chemical nature of the system, the atomic environment, and the symmetry of a substrate [4]. These various effects provide the possibility for building desired structures by adjusting the delicate balance between the lateral interactions and the molecule-substrate coupling. In all the physical and chemical methods for guiding the 2D supramolecular assembly, *Electrochemistry* offers a unique approach for 2D supramolecular fabrication on conductive substrates, because the electrode potential can act as a central tuning source.

1.1.3 Electrochemical approach

As a branch of science with a long history, electrochemistry is not only a technique for characterizing the thermodynamic and kinetic properties, but also a powerful method for stimulating and controlling a system through the application of electrical signals [6]. For example, the free energy of a surface system is directly correlated with the electrochemical potential [10]. Redox-active functional groups incorporated in molecular assemblies can be manipulated, and intermolecular interactions can be adjusted by changing the alignment of molecular dipoles via the electric field in the interfacial region.

All the topics in this dissertation are focused on studies of 2D supramolecular assembled systems on potential-controlled electrode surfaces, in which electrochemistry plays a central role in fabrication and manipulation. Several important concepts and topics of interfacial electrochemistry, which are closely related to the studies of 2D supramolecular assembly structures, will be briefly introduced in Section 1.2. For instance, the model of an electrochemical interface, adsorption, 2D phase transitions, and the interfacial electron transfer reactions.

1.2 An Electrochemical Approach to 2D Supramolecular Assembly

1.2.1 Model of the electrochemical double layer

The interface between the electrode and the electrolyte is the “heart” of interfacial electrochemistry [7]. It is the place where charge transfer takes place, where gradients in electrical and chemical potentials constitute the driving force for electrochemical reactions. This region is called “*Electric Double Layer*” (EDL).

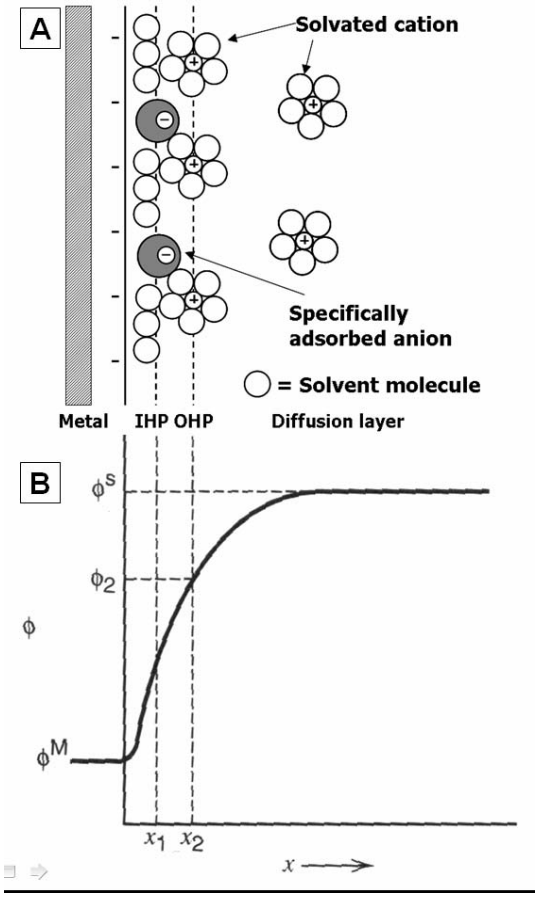

Fig. 1-3: (A) Schematic diagram of the metal/electrolyte interface. The charge build-up at the OHP along with the charge build-up at the surface of the metallic electrode comprises the electric double layer which can be modeled as a parallel plate capacitor; (B) Potential profile across the EDL region in the absence of specific adsorption of ions. ϕ^M, ϕ_2 and ϕ^S represent the potentials in the metal electrode, OHP, and bulk electrolyte, respectively [11,12].

The simplest *Helmholtz model* of the EDL is shown in Fig. 1-3, in which the excess ions in the solution side of the EDL line up in planes ("*Helmholtz planes*") close to the electrode surface. Fig. 1-3A shows two planes of closest approach of the ions: the "*outer Helmholtz plane*" (OHP), and the "*inner Helmholtz plane*" (IHP). Ions in the OHP are hydrated with their solvation shell intact. Ions in the IHP have lost their solvation shell partially or completely, and hence are in direct contact with the

electrode, which is often called contact or specific adsorption [12]. The sharp potential drop in the corresponding potential profile (see Fig. 1-3B) indicates a strong electric field exists in the region between the electrode surface and the OHP.

Considering the non-uniform distribution of the excess ions in the vicinity of the electrode, the concentration of ions is the greatest at the surface of the electrode, and decreases non-linearly until the bulk concentration is reached. The *Gouy-Chapman model* assumes a “diffusion layer” extending from the OHP to the bulk solution through a certain thickness, which is determined by the ion concentration [10]. For example, a 0.1 M electrolyte gives approximately 1 nm thickness of the diffuse layer. The properties of the diffuse layer can have a significant impact on the rate of electron transfer since the actual potential felt by a reactant close to the electrode is dependent on it.

The Gouy-Chapman model assumes that the ions are infinitely small and can get infinitely close to the surface of the electrode. However, this model is not realistic. For example, the ions cannot approach the surface any closer than the ionic or solvated radius. Stern extended the Gouy-Chapman model by considering the finite size of ions, and introducing a "plane of closest approach" [12]. The *Gouy-Chapman-Stern* model combines both the Helmholtz and the Gouy-Chapman models.

A characteristic feature of metal/aqueous electrolyte interfaces is their remarkably high capacity, which ranges from 20 to 50 $\mu F\ cm^{-2}$. These values are much smaller in the case of organic self-assembled monolayers (SAM) on the electrode surfaces due to the large thickness and the lower dielectric constant of the organic materials compared to water. The properties of the EDL in the presence of organic SAMs on electrode surface will be discussed separately in Section 1.3.3.

1.2.2 Adsorption

As discussed in the previous section, building up the EDL often involves adsorption processes. When the concentration of an ion species is higher than that predicted by electrostatic interactions, we speak of *specific adsorption*. Most specific adsorptions are *chemisorption*, i.e. the adsorption caused by chemical interactions between the adsorbate and the electrode. In some cases the adsorption is caused by weaker interactions such as van der Waals forces, and then we speak of *physisorption*.

The amount of adsorbed species is usually given in terms of the *coverage* (θ), which is the fraction of the electrode surface covered with the adsorbate [10].

Considering the adsorption of a species A, the coverage θ is dependent on the bulk concentration c_A in the solution. The relations describing the variation of θ with c_A are known as the *adsorption isotherms*. Based on different considerations, there are several models of adsorption isotherms. Using the absolute rate theory at equilibrium, we can obtain the following relation between θ and c_A:

$$\frac{\theta}{1-\theta} = c_A \exp\left(-\frac{\Delta G_{ad}}{RT}\right) \tag{1.1}$$

with

$$\Delta G_{ad} = G_A - G_{ad} \tag{1.2}$$

where G_A is the molar Gibbs energy of the species A in solution, and G_{ad} that of the adsorbate. Therefore ΔG_{ad} represents the Gibbs energy of adsorption, i.e. the driving force of adsorption lowering the surface free energy. If ΔG_{ad} is considered to be independent on the coverage, Eqs. 1.1 is known as the *Langmuir isotherm*, which is applied when the interaction between adsorbates is small, e.g. at low surface coverage ($\theta << 1$).

If the adsorbate-adsorbate interactions have to be considered in general cases, the ΔG_{ad} is a function of the coverage θ. For a linear relation $\Delta G_{ad} = \Delta G_{ad}^0 + \gamma\theta$, where the constant γ is positive (negative) if the adsorbates repel (attract) each other, one obtains the *Frumkin isotherm*:

$$\frac{\theta}{1-\theta} = c_A \exp\left(-\frac{\Delta G_{ad}^0}{RT}\right) e^{-g\theta} \tag{1.3}$$

where $g = \gamma/RT$, and the Gibbs energy ΔG_{ad}^0 depends on the electrode potential ϕ [10,12].

1.2.3 2D structure transitions

Under equilibrium conditions, the properties of an adlayer are determined by the variation of thermodynamic parameters, such as temperature, pressure, bulk concentration or substrate potential. Changing these parameters can drive *phase transitions* of a system towards a new thermodynamic equilibrium. Considering an electrode/electrolyte interface where the ΔG_{ad} depends on the electrode potential, electrochemistry provides a unique method to control the structure and dynamic properties of adlayers [10].

In addition, the strong electric field in the EDL also considerably influences the lateral ordering of adsorbed molecules by regulating their dipole orientations. An example is shown in Fig. 1-4: the adlayer structures of 4,4'-bipyridine on a Au(111) surface are strongly dependent on the substrate potential [13].

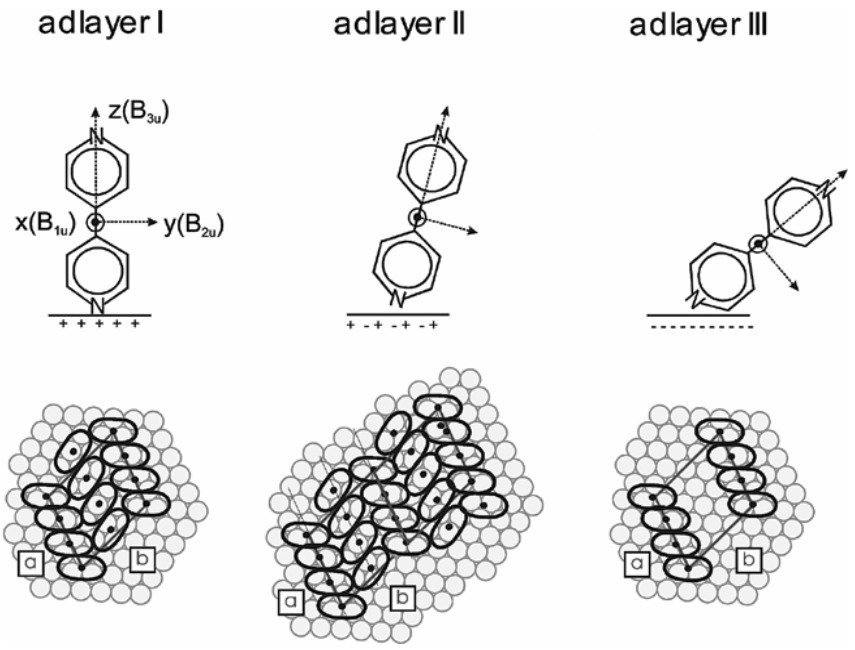

Fig. 1-4: Orientation (derived from SEIRAS experiments) and packing (STM) models of 4,4'-bipyridine on Au(111) at different potentials (from left to right: 0.17 V, -0.21 V, -0.32 V vs. SCE) [13].

The above discussions in Section 1.2.2 and 1.2.3 were focused on phenomena and processes taking place at an ideally polarized electrode/electrolyte interface. In

the following, we will extend the discussion to faradaic processes, which involve electron transfer across the electrode/electrolyte interface.

1.2.4 Interfacial electron transfer reaction

An electrode surface acts as a source or sink of electron (charge) to drive electrochemical reactions. *Electron transfer* (ET) is involved in almost every type of electrochemical reaction. Understanding the nature of ET is of fundamental importance to investigate and manipulate the processes in chemistry, biology, and material sciences.

1.2.4.1 Mechanism

The mechanism of a potential-induced redox reaction on an electrode surface is illustrated in Fig. 1-5. By driving the electrode potential to more negative values, the energy of the electrons in the metal electrode (Fermi level) is raised. When it approaches the LUMO level of adsorbed or solution-based redox molecules, electrons flow as reductive current from the electrode to the molecules. On the other hand, shifting the potential to more positive values can generate an oxidative current from the HOMO of the adsorbed or solution species to the electrode. These two opposite ET processes are defined as reduction and oxidation, respectively.

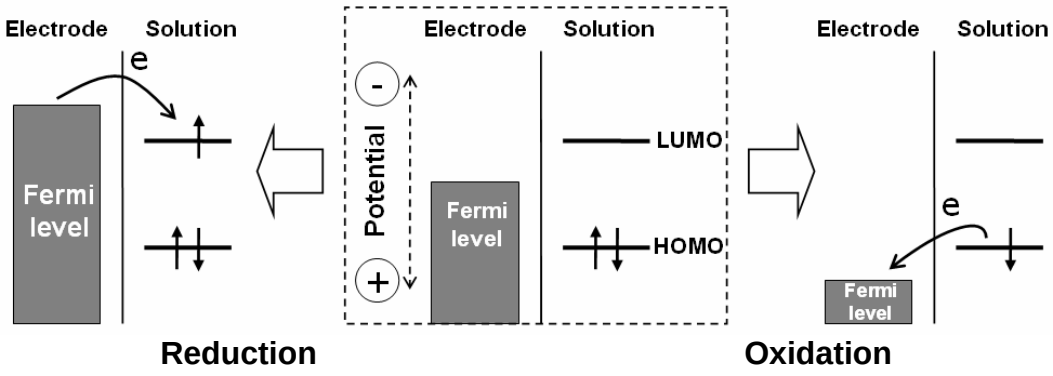

Fig. 1-5: Representation of electrochemical reduction (left) and oxidation (right) of a species adsorbed on the electrode surface or in the solution close to the electrode surface.

1.2.4.2 Equilibrium state: Nernst equation

An electrode reaction involving ET can be written as

$$Ox + ne \Leftrightarrow Red$$

where *Ox* and *Red* represent the oxidized and reduced partners of the redox couple, respectively. The equilibrium potential of this reaction is given by the *Nernst equation*:

$$E = E^0 + \frac{RT}{nF} \ln \frac{a_{Ox}}{a_{\mathrm{Re}d}} \tag{1.4}$$

where E^0 is the standard potential, n the total number of transferred electrons, F Faraday's constant, a_{Ox} and a_{Red} the activities of the oxidized and reduced species. The Nernst equation describes a fundamental relationship between the potential applied to an electrode and the activities of the redox species at the electrode surface [12].

1.2.4.3 Kinetics of electron transfer reactions

As shown in Fig. 1-6, the overall electrode reaction is composed of a series of steps, such as the mass transport to and from the electrode, the intrinsic ET reaction, and chemical reactions (e.g., protonation / deprotonation, disproportionation / comproportionation). Adsorption and desorption processes are also often involved.

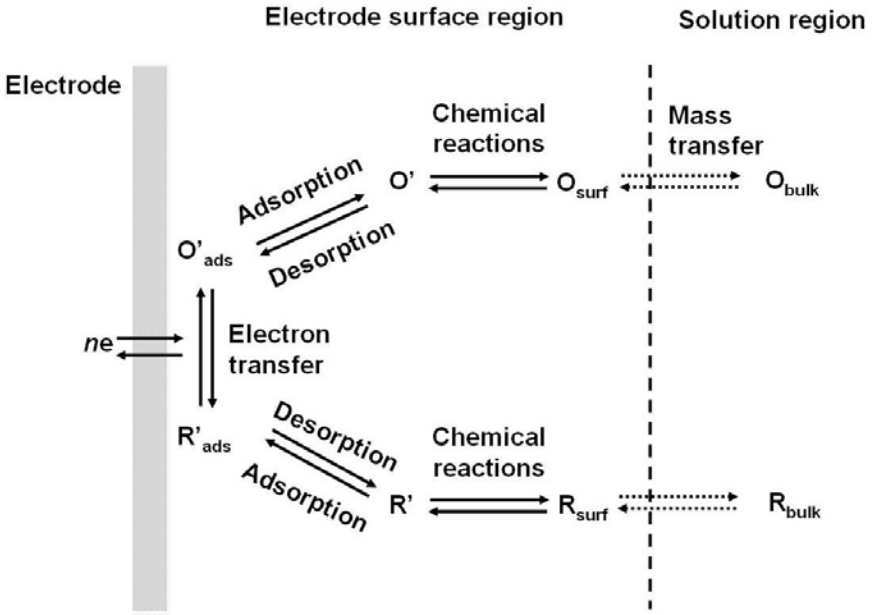

Fig. 1-6: Pathways of a general electrode reaction with redox active species in solution [12].

Consider the same electrode reaction:

$$Ox + ne \underset{k_b}{\overset{k_f}{\Leftrightarrow}} Red$$

in which k_f and k_b represent the rate constant of the forward (reductive) and backward (oxidative) reaction, respectively.

The intrinsic ET reaction can be phenomenological described by the *Butler-Volmer equation*:

$$i = i_0 \cdot \left\{ e^{-\alpha n F \eta / RT} - e^{(1-\alpha) n F \eta / RT} \right\} \tag{1.5}$$

with the *exchange current* i_0:

$$i_0 = F k_0 \cdot \left[C_{Ox}(0,t) \right]^{1-\alpha} \cdot \left[C_{\mathrm{Re}d}(0,t) \right]^{\alpha} \tag{1.6}$$

where α is the transfer coefficient, η the overpotential. C_{Red}(0,t) and C_{Ox}(0,t) represent the oxidized reactant and reduced reactant concentration at the electrode surface, respectively.

The overall oxidation and reduction currents are given by

$$i = i_c - i_a = nFA\left\{ k_f \cdot C_{Ox}(0,t) - k_b \cdot C_{\mathrm{Re}d}(0,t) \right\} \tag{1.7}$$

in which i_c is the cathodic current, and i_a the anodic current.

Under equilibrium conditions, i.e. $i = 0$, Eqs. 1.7 reduces to the Nernst equation.

The Butler-Volmer model represents a phenomenological treatment, and does not consider microscopic details of the ET processes [12]. Marcus [14], Hush [15], Levich [16] and Gerischer [17] developed the fundamentals of a microscopic ET theory by considering molecular vibrations and environmental (solvent) effects [12].

As the simplest form of the Marcus expression, the electron-transfer rate coefficient can be given by:

$$k_{ET} = Z \exp\left[-\frac{\lambda(1 + \frac{\Delta G^0}{\lambda})^2}{4RT} \right] \tag{1.8}$$

with λ representing the reorganization free energy of the reactants to yield the products, ΔG^0 the standard thermodynamic free energy of the reaction, Z an arbitrary

frequency factor (Z ~ 10^4 cm^{-1} for heterogeneous electrode reactions) [14]. The reorganization free energy λ is the sum of the solvation λ_0 and the vibrational λ_i contributions:

$$\lambda = \lambda_0 + \lambda_i \tag{1.9}$$

ET processes are a fundamental issue for the application of electrochemistry to nanoelectronic systems. *Self-assembled monolayers* (SAM) on electrode/electrolyte interfaces provide an important approach for addressing several basic functionalities, such as ultrafast heterogeneous electron tunneling through insulating barriers [18], or the switching behaviors of immobilized functional centers [6]. The concepts and several important issues of SAMs will be introduced in Section 1.3.

1.3 Electrode Surfaces Modified by SAMs

1.3.1 Definition and classification

As discussed in Section 1.2, the heterogeneous kinetics and molecular recognition processes, which are key factors for the performance of functional structures, can be adjusted by electrode potentials. Modification of the electrode can also alter the reactivity of the surface, for example, by reducing the size and accessibility of reactive sites at the interface [6].

Two common strategies for modifying electrodes are based on the *Langmuir-Blodgett* (LB) and *self-assembly* techniques. The LB method generates monolayers, bilayers and multilayers on solid substrates by repeated movement of the substrate across a molecule-modified liquid/gas interface. Self-assembly methods are typically exploited to prepare monolayers on surfaces to form "*self-assembled monolayers*" (SAM). SAMs can be defined as organic assemblies formed by the adsorption of molecular constituents from solution or the gas phase onto a solid surface. The structure of the SAM is determined by substrate/adsorbate and adsorbate/adsorbate interactions, and can be tuned by the chemical nature of the monomeric constituents as well as the substrate surface composition and crystallography [2,11]. A schematic model of a typical SAM is presented in Fig. 1-7. Compared with LB films, SAMs are more flexible to functionalize and fabricate electrodes because they are easy to prepare, and more stable in contact with electrolyte solutions [2]. They have been

applied in numerous studies aiming to tailor the properties of solid/liquid interfaces, including an electrochemical environment. In various examples of SAMs, the ω-functionalized alkanethiols on Au(111) represent a particular universal SAM sample. A schematic model is shown in Fig. 1-7.

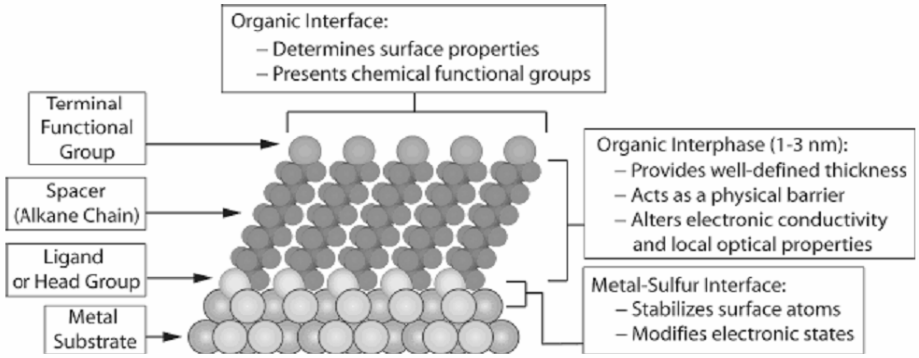

Fig. 1-7: Schematic diagram of an ideal, single-crystalline SAM of alkanethiolates supported on a gold surface with a (111) texture. The anatomy and characteristics of the SAM are highlighted [2].

1.3.2 Formation and structure

The formation of alkanethiol-based SAMs usually starts from the adsorption of the thiol species from the gas phase or from solution. Coordination onto the surface takes place via the formation of covalent Au-S bonds. The formation of Au-S bonds involves two steps: oxidative addition of the S-H bond onto the gold surface and reductive elimination of hydrogen:

$$RS\text{-}H + Au \rightarrow RS\text{-}Au + (1/2)\ H_2$$

which is usually irreversible. Subsequently, a slow long-range ordering process takes place. The intermolecular interactions in the lateral direction are of major significance and are responsible for the organization of the densely packed 2D supramolecular assemblies. Within the most commonly used SAM of alkyl thiols, the alkyl chains are aligned by van der Waals interactions into a close-packed “all-trans” structure with a tilted angle of approximately 30^{o} relative to the surface normal. The corrugation of a Au(111) surface leads to a commensurate ($\sqrt{3} \times \sqrt{3}$)R30 adlayer motif. Such a closed-packed monolayer enables the thickness of the SAM to be tuned by varying the length of the alkyl spacer. Functional groups can be attached onto the SAM either during the synthesis of the monomers or after the completion of a self-assembled matrix. Among

applications in nanofabrication, this feature can be used to incorporate functional groups at defined positions or distances onto a wide range of substrates [19,20].

Chemical modification of an electrode has been widely applied to generate barrier layers that inhibit the free diffusion of electroactive species to the electrode surface, or to functionalize SAMs with immobilized electroactive species.

1.3.3 SAM as a barrier layer for electron transfer

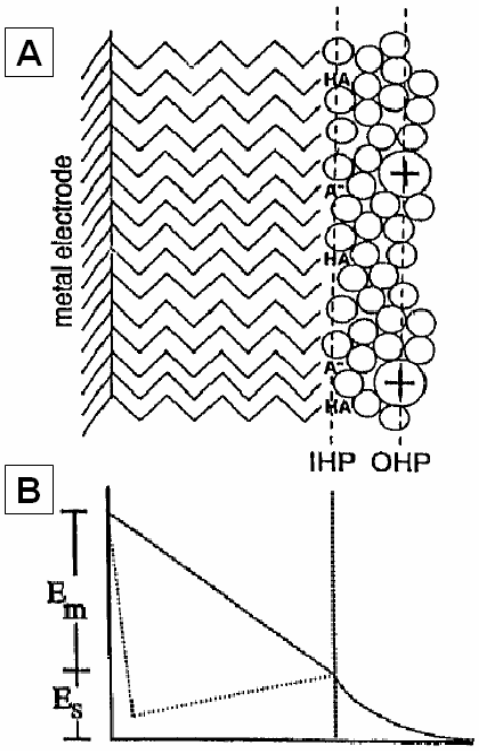

Fig. 1-8: (A) Structure model of the Au-SC_nCOOH electrolyte interface showing the IHP and the OHP. HA and A^- represent undissociated and dissociated COOH groups, respectively [21]; (B) The potential profile across the interface: the solid line assumes a linear potential drop across the alkanethiol portion of the monolayer, while the dotted line includes possible dipoles associated with the Au-S and S-C bonds. E_m: potential drop in the monolayer part, E_s: potential drop in solution part [11].

A close-packed alkanethiol-based SAM may act as a barrier between the electrode surface and the electroactive species in solution. Such an insulating barrier can be described by a modified EDL model, as shown in Fig. 1-8, in which both the IHP and the OHP shift further away from the electrode surface, resulting in a linearly decreasing potential profile within the alkyl chain layer [11]. The ET rate is strongly dependent on the thickness of the insulating layer (exponentially on alkyl chain length). Often, an elastic tunneling model is appropriate [18].

1.3.4 SAMs with tethered electroactive species

Not only can SAMs be designed as a blocking barrier, but also designed as holders for redox active species by fixing them through covalent attachment. The redox active groups can either be selectively adsorbed onto the SAM after self-

assembly, or pre-assembled together with alkanethiols as a mixed SAM where one molecular component contains or terminates with an electroactive group (for example, ferrocene or ruthenium pentaamine).

One important advantage of SAMs with covalently attached redox-active groups is the possibility of controlling the surface concentration of redox active centers via the preparation strategy, which allows a precise positioning and distribution. The effects of diffusion and pinholes on the reaction kinetics can be efficiently decoupled or completely eliminated [22]. Governed by inherent thermodynamics rather than the mass transport kinetics, the redox reactions within a tailored electroactive SAM may exhibit a high reversibility, which is, for instance, important for the design and the operation of switchable molecular devices.

1.4 Motivation

As a unique method of tuning the structure and chemical properties of molecular assemblies, electrochemistry has played an important role for the bottom-up fabrication of 2D supramolecular self-assembled nanostructures on electrode/electrolyte interfaces. The application of electrochemical techniques and concepts in developing 2D functional supramolecular architectures has become one of the most rapidly growing fields in nanotechnology.

Although a huge amount of progress has been made in the development of this interdisciplinary field, there are still many open questions for applications as well as fundamental aspects. For example, what kind of structure and chemical changes affect individual molecular units during assembly, how does the electrode potential influence the fabrication, functionalization and manipulation of supramolecular assemblies. In order to address these fundamental aspects at a molecular level, we carried out a comprehensive electrochemical and vibrational spectroscopic (in situ SEIRAS) study, focusing on the molecular structure, the chemical composition of the adlayer, the role of interfacial water and ions in the 2D supramolecular assembly of specifically tailored monolayers. By correlating the structure and functionalities, we hope to explore new concepts and strategies for the design, fabrication, and functionalization of 2D supramolecular assemblies with potential applications in modern nanotechnology.

1.5 Outline

The present dissertation is organized as follows: Electrochemical and spectroscopic techniques employed in this dissertation work will be introduced in Chapter 2. Experimental details will be summarized in Chapter 3. In order to calibrate some key issues of different characterization techniques, a case study on the structure of the EDL (0.1 M H_2SO_4/Au) will be given in Chapter 4. As the main parts of the dissertation, Chapter 5 and Chapter 6 present the results for two self-assembled systems: trimesic acid adlayers and viologen SAMs on well-defined gold electrodes, respectively.

1.5.1 Phase transitions of 2D supramolecular structures

Our first goal is the direct monitoring of the 2D assembly of tailored molecules on electrode surfaces. We choose aromatic carboxylic acids, such as benzoic acid, terephthalic acid, isophthalic acid, and trimesic acid. Their extended π-orbital tends to bind to the electrode surface in a flat geometry, which allows the exodentate carboxyl groups at the molecular periphery to approach each other in a favorable geometry to form long-range ordered hydrogen-bonded assemblies [4].

The respective carboxyl acid monomers are adsorbed from the bulk electrolyte solution onto the electrode surface, and subsequently assembled into long-range ordered patterns. Potential control is used to steer the adlayer into different structures (potential-induced 2D phase transition). The different adlayer structures are monitored by in situ IR spectroscopy under steady-state and time-resolved control.

1.5.2 Functionalized SAM

The second goal is focused on the molecular structure and interfacial properties of a redox-active SAM. We choose N-hexyl-N´-(6-thiohexyl)-4,4´-bipyridinium bromide as redox-active molecule. These species are composed of one thiol terminal group as an anchor to the electrode surface, symmetrically arranged alkyl spacer units of variable lengths and a central viologen moiety. Depending on the electrode potential applied, the viologen group may exist in three different oxidation states, the dication V^{2+}, the radical cation $V^{\cdot+}$, and the neutral form V^0 [23]. In the present work we employ IR-spectroscopy to investigate the self-assembly process, the structure of

the SAM, as well as the role of the solvent for tuning different redox states. The kinetics involved in the redox switching was investigated by time-resolved IR spectroscopy in combination with electrochemical methods.

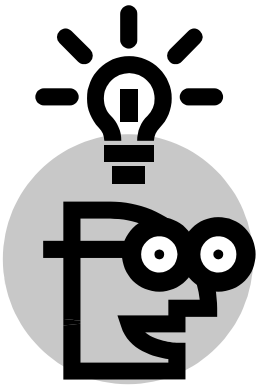

Chapter 2. Characterization Techniques in 2D Supramolecular Chemistry

2.1 Overview Characterization Methods

Many physical and chemical techniques have been employed to characterize supramolecular assemblies on 2D substrates, such as contact angle measurements, FT-IR/Raman Spectroscopy, X-ray Photoelectron Spectroscopy, Ellipsometry and Surface Plasmon Resonance, and SPM techniques. The presence of a conductive metal electrode as a conductive substrate makes electrochemistry a powerful approach for controlling and analyzing structures and chemical properties of 2D supramolecular assemblies. These techniques are summarized in Table 2-1 [6,11,24,25].

Table 2-1: Analytical techniques for 2D supramolecular assembled structure.

Analytical techniques	*Gained information*
Electrochemical	
Voltammetry (CV, LSV)	Electrochemical control, electrochemical reaction, structure transition
Chronoamperometry	
Chronocoulometry	
Impedance spectroscopy	
Spectroscopic/Optical	
FT-IR/Raman spectroscopy	Molecular vibrational/electronic structure, functional groups, chemical composition, local molecular interaction, surface coverage, layer thickness
SFG, INS	
UV-vis absorbance	
Fluorescence spectroscopy	
Ellipsometry	
Surface Plasmon Resonance	
High vacuum based surface methods	
XPS, AES	Chemical composition
SIMS	Molecular mass of adsorbate or fragment
HREEL, LEED	Surface pattern
EXAFS, XEANS	Atomic environment, coordination structure
Microscopic	
STM	Molecular organization, 2D structure
AFM	
Other	
QCM/EQCM	Mass change
Contact angle	Surface hydrophobicity, order
Molecular simulation	Support/interpretation of experiment results
DSC, DTA	Thermo-stability, chemical composition

Limited by individual principles, each technique can provide only one or several certain types of physical/chemical information of a given sample. In most cases, the combination of several different characterization methods is important for a comprehensive understanding. In the present dissertation work, electrochemical approaches, such as cyclic voltammetry (CV) and chronoamperometry have been combined with a special in situ IR technique, *ATR-SEIRAS* (Attenuated Total Reflection - Surface Enhanced Infrared Absorption Spectroscopy), to explore specific aspects of self-assemblies and reactivity at modified gold electrodes.

2.2 Interfacial Electrochemistry

Electrochemical methods for the study of 2D supramolecular structures on electrodes are usually focused on interfacial electrochemistry, which can be further classified into equilibrium and dynamic studies. Equilibrium methods deal with equilibrium conditions without net current flowing through the interface. In dynamic methods, measurements are made away from equilibrium conditions. In the general characterization of interfacial phenomena related to supramolecular chemistry, the current is often measured under potential control (potentiostatic condition). The potential control is usually applied as a potential sweep and a potential step.

2.2.1 Electrochemical cells

Electrochemical measurements are carried out in an electrochemical cell employing an appropriate electrolyte and electrodes connected to a potentiostat to give external potential control. In the simplest two-electrode cell (Fig. 2-1A), the electrodes have different functions. The *working electrode* (WE) is usually where the processes or reactions of interest take place. The second electrode, a combination of *reference electrode* (RE) and *counter electrode* (CE), controls the potential. However, this simple two-electrode configuration is not suitable for electrochemical measurements with current flow because of the polarization of the RE, which modifies the electrode potential. Alternatively, a third auxiliary electrode, or *counter electrode* (CE) is brought into the current loop, and the input impedance of RE is high, in order to force all the current through the CE instead of the RE. In such a three-electrode cell (Fig. 2-1B), an exact potential control can be maintained by the separation of potential and current measurements into RE and CE loops, respectively.

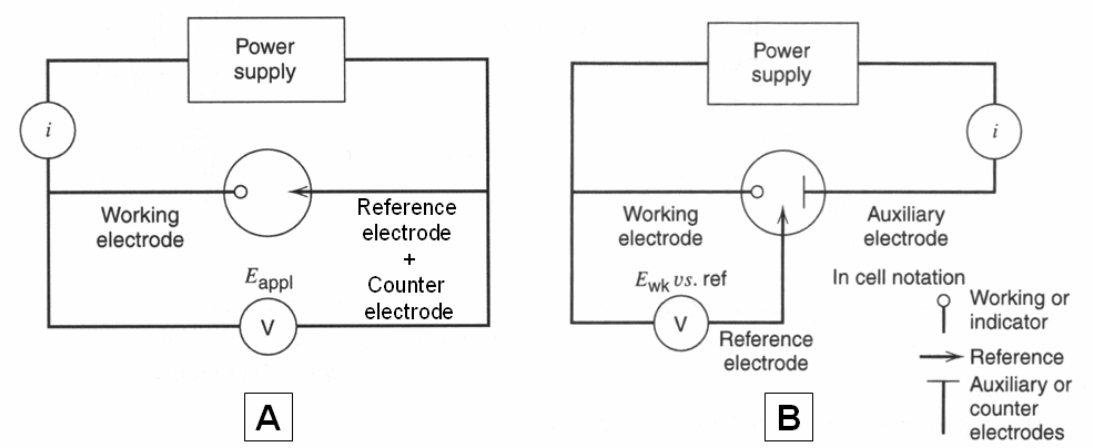

Fig. 2-1: (A) Two-electrode electrochemical cell; (B) Three-electrode electrochemical cell [12].

The design of the electrochemical cells used in this work will be described in Chapter 3.

2.2.2 Potential sweep method

2.2.2.1 Linear sweep and cyclic voltammogram

In potential sweep methods the potential of the WE (with respect to the RE) is varied continuously according to a predefined potential wave function. The current is measured as a function of the applied potential (*voltammogram*). The potential sweep technique, also named *voltammetry*, is the most commonly used electrochemical method to monitor characteristics of interfacial redox properties.

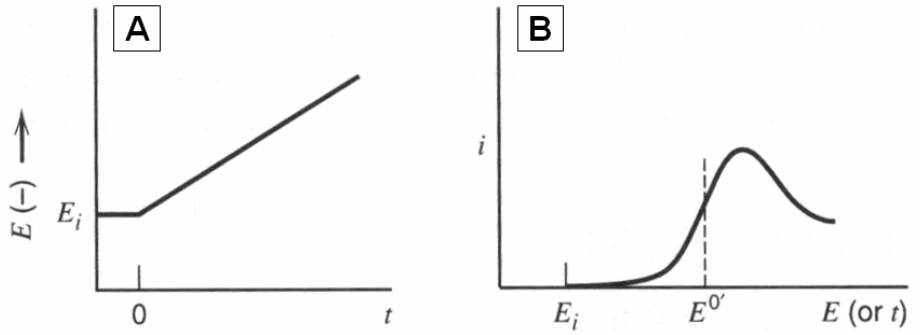

Fig. 2-2: LSV (A) Linear potential sweep or ramp starting at E_i. (B) Resulting *I-E* curve [12].

The simplest potential sweep method is the *linear sweep voltammetry* (LSV), in which the potential of the WE varies linearly with time in a certain potential range

(see Fig. 2-2A). Both capacitive (EDL charging) and faradaic currents contribute to the recorded signal.

If the reversible reaction $Ox + ne \Leftrightarrow Red$ takes place on a planar electrode under diffusion control, the LSV voltammogram measured exhibits a characteristic peaked shape (see Fig. 2-2B) [12] with a maximum current given by the Randles-Sevčik equation:

$$i_p = (2.69 \times 10^5) n^{3/2} A C_{Ox} (D_{Ox} v)^{1/2} \tag{2.1}$$

which applies for 25 °C, A is the electrode area in cm^2, D_{Ox} the diffusion coefficient in cm^2 s^{-1}, C_{Ox} the bulk concentration in mol cm^{-3}, and v the scan rate in V s^{-1}.

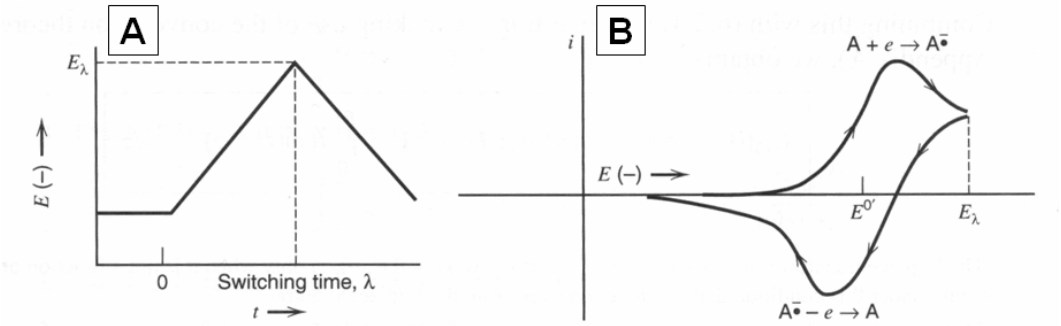

Fig. 2-3: CV (A) Cyclic potential sweep. (B) Resulting CV [12].

Cyclic Voltammetry (CV) is based on the same principle as LSV. However, the potential sweep is reversed at a certain potential value E_λ (Switching potential) after passing the reduction peak (Fig. 2-3A), and generates a reversed voltammogram having a similar shape as the forward one (Fig. 2-3B). The purpose of the reversed scan is to probe the stability of the reduced species and/or the reversibility of the ET reaction, because an unstable species will be converted to other species and therefore depleted from the vicinity of the electrode, thus gives no contribution in the reversed scan.

Depending on different shapes of a CV, the characteristics on the nature of electrode reactions can be derived from the peak current values (i_{pa}, i_{pc}), the peak potentials (E_{pa}, E_{pc}), or the voltage separation of anodic and cathodic current peaks (ΔE_p) in dependence of the potential scan rate (v) [12,26]. Selected applications, which are relevant to this thesis, will be briefly described next.

2.2.2.2 2D phase transitions in organic adlayers

The potential sweep range for a non-faradaic process on an "ideally" polarized interface is usually limited between the surface oxidation of OH^- and the evolution of H_2 species (*Double layer range*). The CV shows typically a continuous positive or negative "background" current during the anodic or cathodic sweep, respectively, sometimes with narrow current peaks indicating potential-dependent phase transitions within the adlayer or of the substrate surface. These phase transition peaks originate from the charging processes when the adlayer or substrate capacitance changes. The phase transitions may involve changes between gaslike adlayers, disordered physisorbed adlayers, ordered physisorbed adlayers, and chemisorbed adlayers [27,28]. The adlayer capacitance can be estimated by

$$\Delta i = 2\nu C \tag{2.2}$$

where Δi is the difference between the cathodic and the anodic current at each measured potential [6].

2.2.2.3 Electron transfer reactions under diffusion control

This situation represents a typical electrochemical process, in which a redox active couple in the bulk solution approaches the electrode surface via diffusion, reacts in the vicinity of an electrode surface or on the outer surface of a blocking monolayer such as an alkanethiol SAM. The CV of such a reversible electrochemical reaction shows the following characteristics, as illustrated in Fig. 2-4A:

i) The voltage separation between the current peaks is

$$\Delta E = E_{pa} - E_{pc} = \frac{59}{n}\ \text{mV} \tag{2.3}$$

ii) The positions of the peak potentials are independent on the voltage scan rate;

iii) The ratio of the peak currents is equal, i.e.

$$\left|\frac{i_{pa}}{i_{pc}}\right| = 1 \tag{2.4}$$

iv) The peak currents are proportional to the square root of the scan rate

$$i_{pa} \text{ and } i_{pc} \propto \sqrt{v} \tag{2.5}$$

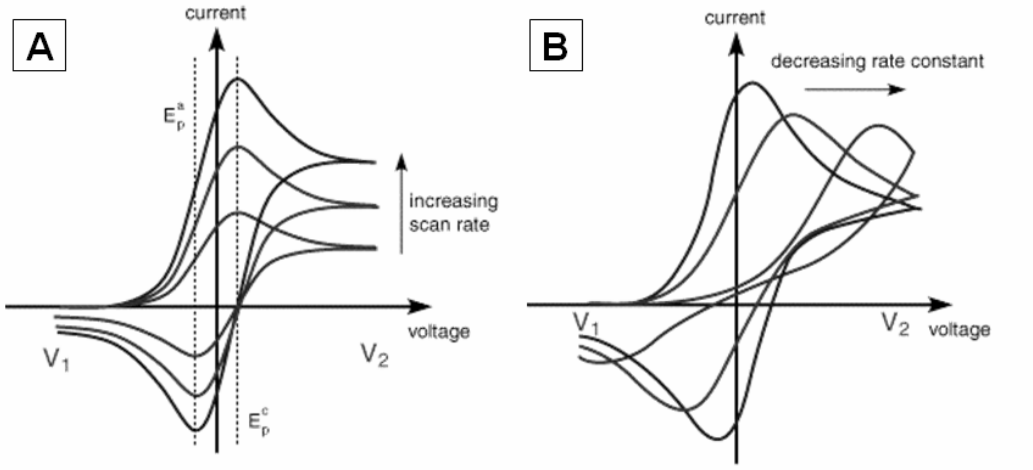

Fig. 2-4: (A) The influence of the voltage scan rate on the current for a reversible ET reaction; (B) irreversible ET reaction under diffusion control [29].

If the ET is irreversible, the CV shows different characteristics. Fig. 2-4B shows the voltammograms for a quasi-reversible reaction for different values of the reduction and oxidation rate constants. As the rate constants are lowered, the peak separation ΔE_p becomes larger and varies as a function of the scan rate, because the equilibrium at the surface cannot be rapidly established within the time window of the voltage scan. The ET rate constants can be estimated by analyzing the variation of the peak position as a function of the scan rate v [26].

2.2.2.4 Surface-immobilized redox active species

An SAM represents a simple but important example of this type of redox systems, in which both partners of the redox couple are immobilized covalently or electrostatically. A typical CV for a completely reversible system is shown in Fig. 2-5. The following characteristics can be derived:

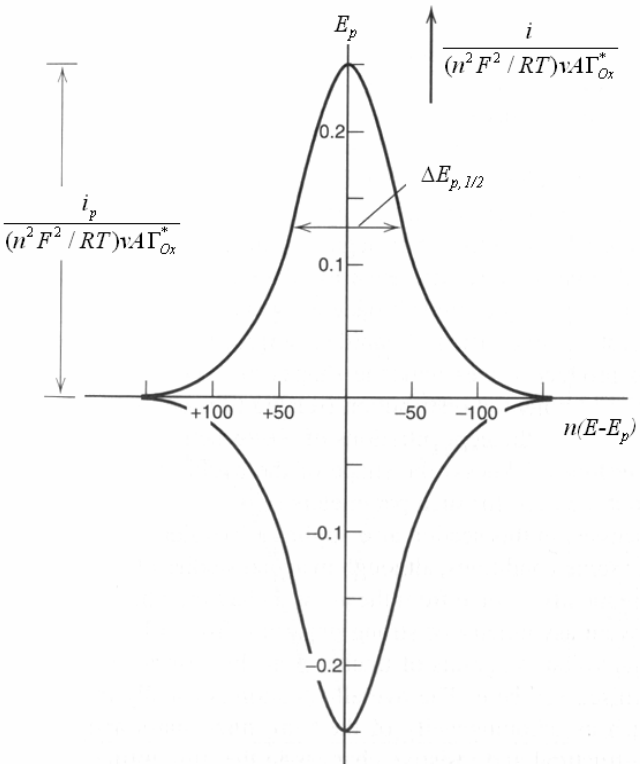

Fig. 2-5: CV for the reduction and the subsequent reoxidation of adsorbed *Ox* species. The current is given in a normalized form [12].

i) For an ideal reversible reaction obeying a Langmuir-type adsorption, the anodic and cathodic curves are symmetric to each other with equal i_p (i_{pa} = i_{pc}) and E_p ($\Delta E_p = 0$) [12]. However, in most cases small non-zero ΔE_p is observed but does not increase with increasing scan rate, indicating there is no kinetic limitation. This might be related to some intrinsic complexity in the ET reaction.

ii) The peak currents are proportional to the scan rate

$$i_p = \frac{n^2F^2}{4RT} vA\Gamma^*_{Ox} \tag{2.6}$$

where $\Gamma_{Ox}{}^*$ represents the surface coverage of the adsorbed oxidized species.

iii) The surface coverage of the redox active species $\Gamma_{Ox}{}^*$ can be estimated from the charge transfer *Q* (integration of the area under the CV curve):

$$\Gamma^*_{Ox} = \frac{Q}{nFA} \tag{2.7}$$

iv) The total width at half-height ($\Delta E_{p,1/2}$) of either anodic or cathodic wave is given by

$$\Delta E_{p,1/2} = 3.53\frac{RT}{nF} = \frac{90.6}{n} \text{ mV } (25\ ^{o}\text{C}) \qquad (2.8)$$

which represents the case of a non-interacting redox species. Larger or smaller values of $\Delta E_{p,1/2}$ indicate repulsive or attractive interactions between neighboring redox species, respectively. The limit of extremely sharp peaks usually indicates the coupling with a phase transition accompanied by dramatic capacitance changes.

2.2.3 Potential step method

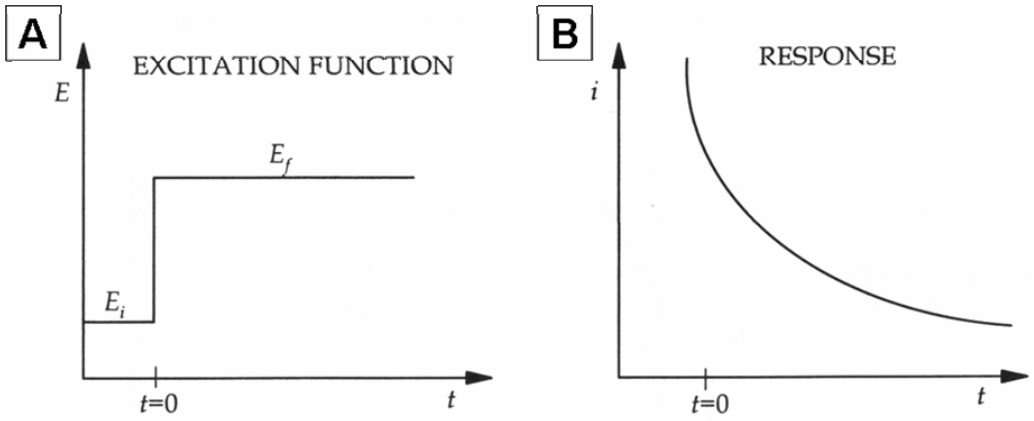

Fig. 2-6: (A) Typical potential excitation function (step); (B) Resulting current response in chronoamperometry [6].

As the simplest excitation function of an electrode process, a potential step means an abrupt change of the potential of the WE from an initially pre-conditioned value E_i, at which no current flows, to a final value E_f, at which a faradaic or non-faradaic process takes place at an appreciable rate [6]. The current transient response (*chronoamperometry*) is recorded with t = 0 as the time of the sudden potential change. A typical current transient and its potential step profile are shown in Fig. 2-6.

2.2.3.1 Electron transfer reaction under diffusion control

For a fast electrode reaction on a planar electrode under diffusion control (so-called *Cottrell condition*), the diffusion-limited current response is given by the *Cottrell equation*:

$$i(t) = nFAC_{Ox}\sqrt{\frac{D_{Ox}}{\pi \cdot t}} \tag{2.9}$$

Eqs. 2.9 implies that the diffusion-controlled current i is proportional to $t^{-1/2}$.

The integration of $i(t)$ gives the diffusional charge transfer transient (*chronocoulometry*) Q_d as

$$Q_d(t) = 2nFAC_{Ox}\sqrt{\frac{D_{Ox} \cdot t}{\pi}} \tag{2.10}$$

which implies that $Q_d(t) \propto t^{1/2}$. Taking the contributions from EDL charging, Q_{dl}, and the redox ET of the adsorbed species, Q_{ads}, the total charge transfer Q_t can be written as

$$Q_t = Q_d + Q_{ads} + Q_{dl} = 2nFAC_{Ox}\sqrt{\frac{D_{Ox} \cdot t}{\pi}} + nFA\Gamma_{Ox} + Q_{dl} \tag{2.11}$$

where the sum of Q_{dl} and Q_{ads}, which are time-independent, can be estimated by extrapolating the $Q \sim t^{1/2}$ plot to $t \rightarrow 0$ (see Fig. 2-7).

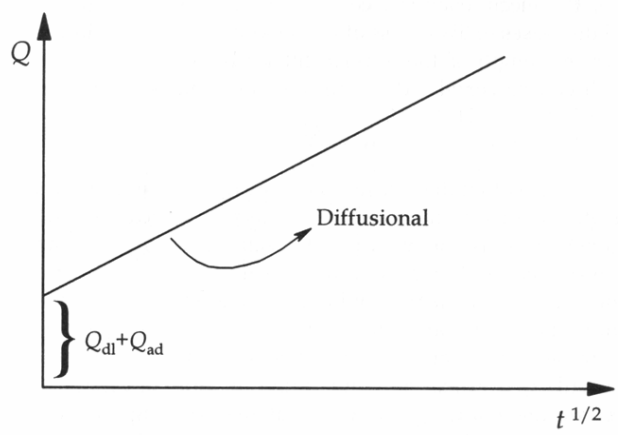

Fig. 2-7: Charge components in a chronocoulometric (Q *vs.* $t^{1/2}$) plot [6].

2.2.3.2 2D phase transitions in organic adlayers

The potential step technique is also a useful tool to study the kinetics of potential-induced 2D phase transition on electrode surfaces. The shape of transient curves depends on different mechanisms. If we assume a Langmuir-type (or random) adsorption/desorption kinetics without interactions between the neighboring adsorbed species, the corresponding chronoamperometric response can be expressed by the exponential decay function (Fig. 2-8A) [30]

$$i(t) = k_1 \exp(-k_2 t) \tag{2.12}$$

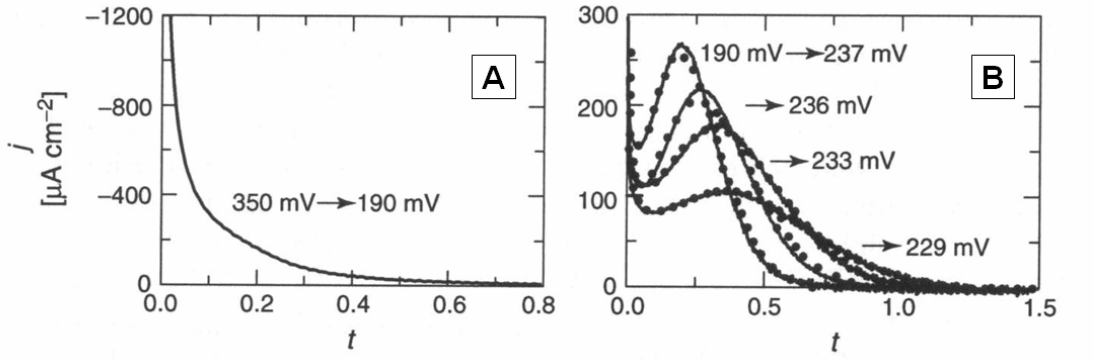

Fig. 2-8: Representative current transients of (A) Langmuir-type adsorption (Eqs. 2.12), and (B) instantaneous (hole) nucleation-and-growth kinetics (Eqs. 2.13). Measured for the 2D phase transitions for Cu UPD on Au(111) in 0.05 M H_2SO_4 + 1 mM $CuSO_4$ solution [31].

For a nucleation-and-growth process, one often observes a maximum in the current transient curve (Fig. 2-8B). A well-established and frequently used model for nucleation-and-growth processes is based on the Bewick–Fleischmann–Thirsk theory [32]). As an example:

$$i(t) = k_3 t^{n-1} \exp(-k_4 t^n) \tag{2.13}$$

where n = 2 if a fixed number of nuclei are formed immediately after the potential step and a linear growth law applies (instantaneous nucleation). On the other hand, n = 3 if nuclei are formed continuously during a linear growth process (progressive nucleation). [30]

In summary, the interfacial electrochemical characterization based on equilibrium and dynamic methods provides overall information on electrochemical

processes at the electrodes or within the adlayers, such as the stability, the reversibility of reactive species, or the mechanisms of non-faradaic and faradaic electrochemical reactions. However, it cannot directly probe the molecular structures and the chemical composition at and next to the interface (including anions, cations and solvent molecules). Other complementary characterization methods are needed to develop a detailed understanding of structure and functionality. Due to its sensitivity to the local molecular structure, infrared spectroscopy represents one of the most versatile complementary approaches.

2.3 Spectroelectrochemistry: FT-IR

Recent years have seen continuous interest in studying electrode processes by experiments that involve more than the usual electrochemical variables of current, charge, and potential [12]. The most important motivation is to obtain a more detailed structure or chemical information. In situ *Spectroelectrochemistry*, defined as a certain combination of classic electrochemical methods with surface-sensitive spectroscopic techniques, has become a powerful approach for the characterization of 2D supramolecular structures on electrode substrates.

As one of the most popular spectroelectrochemical techniques, in situ *Fourier Transform Infrared spectroscopy* (FT-IR) has been widely used, because it is structure-specific, non-destructive, easy-operating, and enables a rapid-detection. It provides detailed structure and chemical information of adsorbed molecules on electrode surfaces. This dissertation work will focus on the application of ATR-SEIRAS in the characterization of 2D supramolecular assembled structures on gold electrodes.

2.3.1 Considerations on IR setups in electrochemical research

Modern FT-IR spectroscopy usually uses three spectra-collecting approaches: *transmission*, *external reflection* and *internal reflection* [33]. The transmission approach is not suitable for detecting signals from electrode/electrolyte interfaces due to limitations on the minimum thickness of minigrids, and its low sensitivity to the adsorbed species on surfaces. Most electrochemical in situ FT-IR measurements are based on reflection configurations.

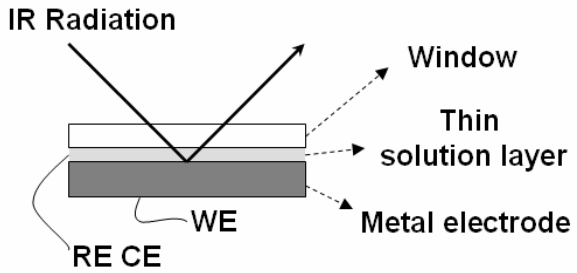

Fig. 2-9: External reflection configuration with a thin layer of electrolyte solution trapped between a WE and an IR window.

External reflection is the most often employed approach, where an electrochemical system is trapped in a thin layer of electrolyte (1~50 μm) between a reflective working electrode and an IR-transparent window (see Fig. 2-9). Examples of the external reflection include SNIFTIRS (*subtractively normalized interfacial FT-TR spectroscopy*) and IRRAS (*infrared reflection absorption spectroscopy*). The purpose for such a thin layer configuration is to minimize the interference from solvent absorption, which is usually much stronger than the interfacial signal from the adsorbed species of interest. However, the high solution resistance in such a thin layer solution allows only a very slow response to a potential modulation. Other limitations are the uneven potential distribution and the hindered mass transport. The external reflection is only suitable for steady-state or slow kinetic measurements, in contrast to internal reflection methods, such as *attenuated total reflection* (ATR) or *multiple internal reflection* (MIR) (see Fig. 2-10).

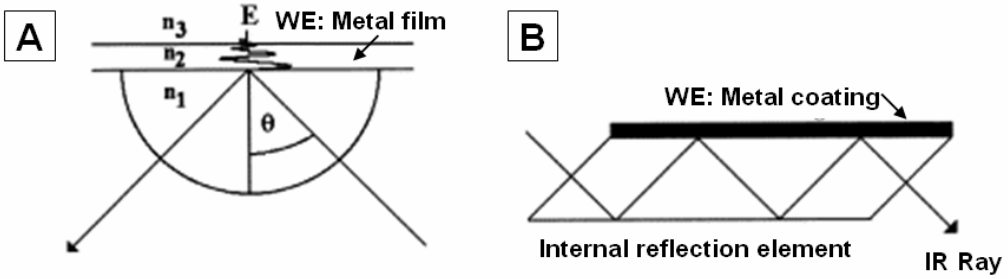

Fig. 2-10: (A) Kretschmann configuration adopted in an attenuated total reflection cell. *E* is the evanescent wave, θ the angle of incidence, n_1 the refractive index of the internal reflectance element, n_2 that of the working electrode and n_3 that of the electrolyte. (B) Multiple internal reflection configuration (MIR-FTIR) to enhance the sensitivity [33].

This dissertation work focuses on the application of an ATR configuration, which relies on the total reflection of an IR beam at the internal surface of an IR-transparent crystal (*internal reflection element*, IRE) of high IR refractive index n_1, such as Ge, Si, ZnSe etc. In many spectroelectrochemical investigations, the IRE is

generally a prism coated with a thin layer of metal (Au or Ag) as a working electrode (*Kretschmann arrangement*). This type of film electrodes, which are usually evaporated on the surface to form a continuous island structure, shows not only polycrystalline or quasi-(111) single crystal features, but also a pronounced surface enhancement of the IR cross-section, which will be discussed separately in Section 2.3.2.

At a proper incident angle larger than the *critical angle* (defined by $\theta_c = \sin^{-1}[n_3/n_1]$), total reflection occurs in the IRE. The thin metal film is almost transparent to the IR radiation with a sufficiently large wavelength. The incident and reflected waves superimpose resulting in a standing evanescent wave that decays exponentially in the vicinity of the crystal surface (See Fig. 2-10A). The *penetration depth* d_p of such an evanescent wave is given by

$$d_p = \frac{\lambda}{2\pi\left(\sin^2\theta - (n_3/n_1)^2\right)} \tag{2.14}$$

with λ representing the wave length, θ the incidence angle, and n_1, n_3 the refractive indices of the prism and of the electrolyte, respectively. It is estimated between 150 ~ 600 nm in the mid-infrared range (1000 ~ 4000 cm^{-1}) [41]. Such a reduced path length reduces the strong solvent absorption considerably, thus the contribution from the interfacial range can be easily "picked out" by adopting a "difference" protocol: First, the reference spectrum, S_r, is collected at the reference potential, E_r, usually chosen in an electro-inactive region. The electrode potential is then swept to a different value of interest, E_s, and spectra, S_s, are collected as a function of the potential; or the potential is stepped to E_s, and the spectra S_s are collected as a function of time. The spectra are usually presented as *reflectance*:

$$\Delta R/R = (S_s - S_r)/S_r \tag{2.15}$$

or *absorbance A* [34]:

$$A = -\lg(S_s/S_r) \tag{2.16}$$

The resulting difference spectra contain only those absorptions which change with potential and/or time. Positive-going IR bands refer to an increase of the related species at E_s relative to E_r, negative-going bands indicate a loss of species.

2.3.2 Surface enhancement

The IR absorption intensity can be significantly increased by 10~1000 times on islands of coinage metals, in comparison to conventional IR measurements. This phenomenon is called *surface enhanced infrared absorption* (SEIRA), which is based on a similar mechanism as the widely-studied surface enhancement in Raman spectroscopy [12]. It was firstly reported by Hartstein et al. in 1980 [35,36] in the Kretschmann-ATR configuration, and developed experimentally and theoretically by Hatta, Suetaka and Osawa [37,38,39]. The application of the SEIRAS technique to electrochemical interfaces was pioneered by Osawa et al. [35,40].

Similar to the well established mechanism of surface enhanced Raman spectroscopy (SERS), the SEIRA phenomenon is attributed to both “electromagnetic” and “chemical” origins [40].

2.3.2.1 The electromagnetic mechanism

Evaporated metal thin films on non-metallic substrates are not continuous, but consist of small islands with an average diameter of about 30 nm and a height similar to the film thickness, as observed by AFM (Fig. 2-11A) and schematically illustrated in Fig. 2-11B. The mechanism results from the polarization of these metal islands by the electromagnetic field of the incident radiation. First the oscillating field of the incident light induces an oscillating dipole in the island via the excitation of localized plasmon, and then the induced dipole produces an electric field around the island and finally excites the absorbed molecules. The induced electric field is normal to the local island surface. This leads to the *surface selection rule*: only the molecular vibrations having dipole changes normal to the local surface can be excited and enhanced. Such a surface selection rule is important to explore the orientation of adsorbed molecules. On the other hand, the local electric field decays within a short distance away from the surface, which implies that this local enhancement occurs only in the near vicinity of the islands, gives a dominant contribution from the first layer of adsorbed species.

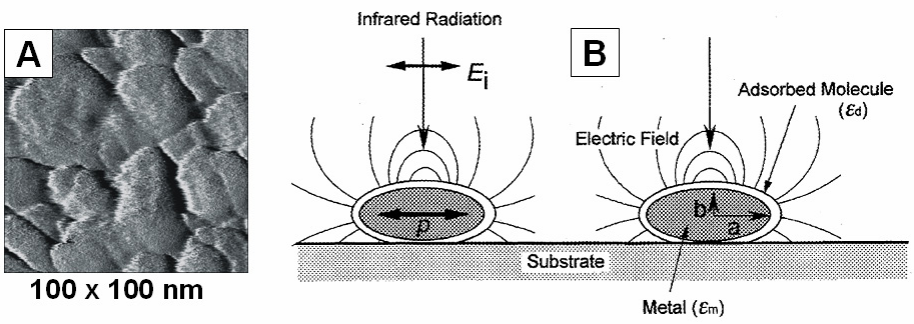

Fig. 2-11: (A) AFM image of the island morphology of an electron-beam evaporated Au-film on silica surface; (B) Electromagnetic mechanism of surface enhancement [40].

Suetaka et al. investigated the influence of the metal film thickness and the role of s- / p-polarization of the incident light on the enhancement [41,42]. Their results show that the p-polarized light can induce polarization changes of the metal film in the direction normal to the macroscopic film more efficiently than s-polarized light.

2.3.2.2 The chemical mechanism

In addition to the dominant contribution of the electromagnetic enhancement, a chemical mechanism also contributes. Experimental observations suggest that chemisorbed molecules exhibit a larger enhancement than physisorbed molecules. Such a chemical mechanism can be interpreted as follows.

i) Chemisorption usually aligns the absorbed molecules, thus giving a larger intensity when the molecular dipoles are also aligned parallel to the surface normal [43];

ii) The absorption coefficient (dipole moment) of molecules is increased upon chemisorption. It can be related with the strong donor-acceptor interactions between molecules and the metal substrate, or the lateral interaction between neighboring molecules (e.g., $\pi - \pi$ stacking between adsorbed CO molecules) [40];

iii) In some special cases, certain IR bands, which are IR-inactive (totally symmetric modes), can be also enhanced via the *vibronic coupling* of

vibrational modes with the charge transfer between the adsorbate and the metal surface [40].

2.3.3 Time-resolved techniques for kinetic studies

The kinetics of fast electrochemical processes can be explored by electrochemical transient methods (fast scan CV, chronoamperometry, chronocoulometry, etc.). However, important structure and chemical information involved in a kinetic process cannot be unambiguously extracted from the obtained electrical response. Due to the high intensity of the SEIRA signals and the ATR configuration giving a fast response to a potential modulation, the dynamic monitoring of reversible molecular events at the electrochemical interface is facilitated by time-resolved ATR-SEIRAS experiments. The time resolution ranges from seconds to a few microseconds [40]. In a general electrochemical setup with a standard size electrode (~ mm), the SEIRAS time-resolution of a few microseconds is already sufficient, because the electrode/electrolyte interface cannot response faster due to the time required for double layer charging (several tens of microseconds).

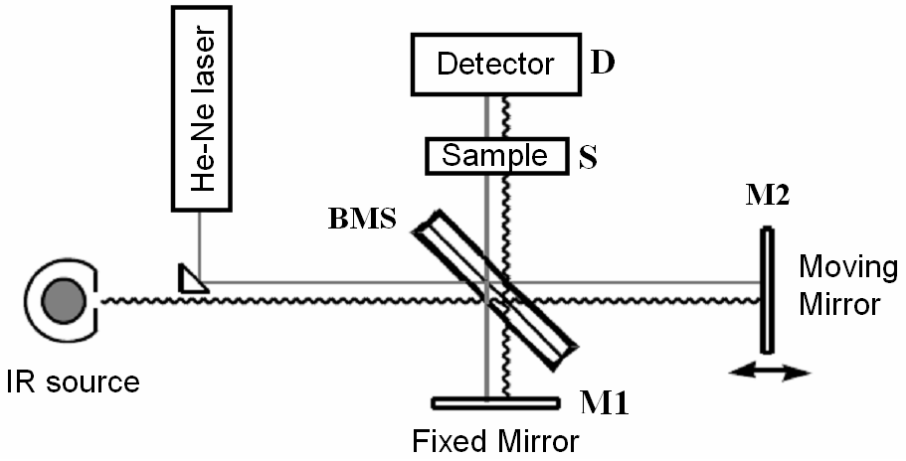

Fig. 2-12: Michelson interferometer in one of the general configurations of an FTIR spectrometer (revised from Ref. [44]).

Time resolved FT-IR measurements rely on the application of the FT technique in combination with a Michelson interferometer. The working principle of the interferometer is shown in Fig. 2-12, with one *fixed mirror* (M1) and another *moving mirror* (M2). The mid-IR light is first split by the *half-beamsplitter* (BMS), reflected by both mirrors, and recombined on the other side of the beamsplitter, then passes the sample (S), and finally is focused onto the detector (D). An optical retardation

(δ) between the two combined IR beams originates from the relative movement of the moving mirror, thus generates an interference pattern in the composite IR beam, i.e. the *interferogram* I(δ) which represents an intensity function of the moving mirror position. When a digital Fourier transform is applied, such a function I(δ) can be converted to a *single beam spectrum* I(ν), i.e. the intensity function of the wavenumber or the frequency. A set of single spectra can be further co-added, averaged to increase the S/N ratio, and used for mathematical treatments to obtain absorbance or reflectance spectra.

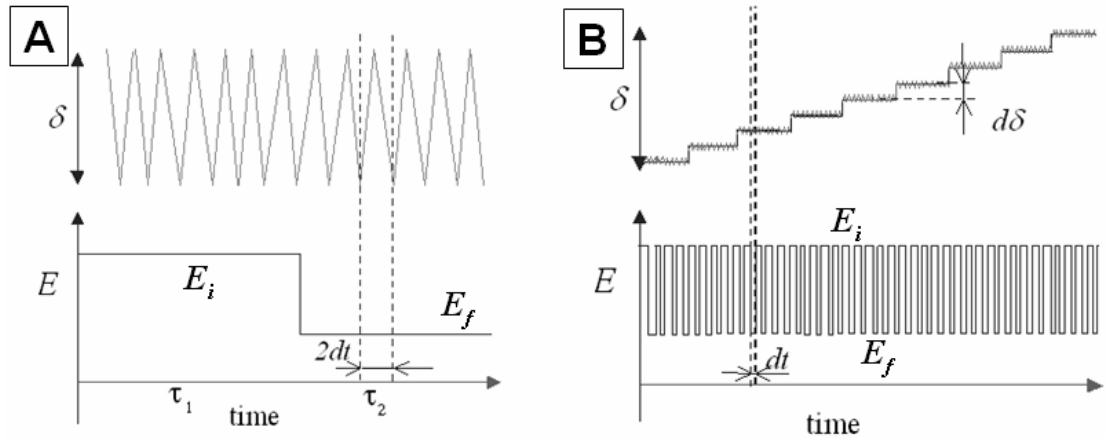

Fig. 2-13: Rapid scan (A) and step scan (B) spectra acquisition regimes. *δ*: optical retardation generated by the movement of a mirror; *E*: potential modulation.

The moving mirror's velocity can be chosen to ensure that each scan is fast enough to record the spectra of one dynamic event during the time scale of interest. This type of spectra acquisition mode based on a fast movement of a mirror is defined as *Rapid Scan*. Fig. 2-13A shows the relation between the mirror movement and the potential step regime in an electrochemical modulation, in which the time-resolved FT-IR spectra are recorded one by one right after a potential step from E_i to E_f.

A higher time-resolution can be achieved by the so-called *Step Scan* acquisition mode. As defined by the name, the mirror retardation is achieved in discrete steps. At each retardation point, the moving mirror is held and stabilized at fixed position. The resulting retardation δ is changing step by step as shown in Fig. 2-13B. In each step, the desired reaction is initiated via a potential step and the signal can be continuously collected in a much shorter time scale *d*t than the rapid scan mode. Then the moving mirror is stepped forward to the next retardation position and the signal is

accumulated in the same way. The step processes are repeated until the retardation reaches a certain maximum value required for a specific spectra resolution.

Except the kinetic study, the measurement for a steady-state system can be carried out by the so-called *Slow Scan* mode, which is usually combined with a voltammetry measurement, i.e. a slow potential sweep. The potential sweep rate is usually chosen ≤ 50 mV s^{-1} to keep a "dynamically" steady state of an electrochemical system. The spectra acquisition mode on the spectrometer part is the same as that in rapid scan mode. A certain number of spectra acquired continuously over a small potential sweeping range can be averaged and result in a set of *quasi-steady-state* spectra in the corresponding potential scale. Compared with the spectra measurements at fixed potentials, the slow scan spectra acquisition mode combined with the potential sweep modulation provides access to the processes directly related to the voltammetric experiments.

2.3.4 Advantages of the ATR-SEIRAS in spectroelectrochemistry

In summary, the application of in situ ATR-SEIRAS at electrochemical interfaces takes several advantages, in comparison to the classical thin layer configuration of IRAS [35]:

i) High and specific surface sensitivity with an enhancement of the IR response of both physisorbed and chemisorbed species up to ca. 100 times as in conventional IRAS;

ii) Dominant first layer effect (Helmholtz region) with a short decay length of the enhanced field of 3 ~ 4 nm (Gouy region) towards the bulk electrolyte;

iii) Signals from the interface and the solution background are of comparable magnitude and can be separated by applying the potential difference tactics. The absorption of bulk solvent can be easily subtracted in the potential different spectra;

iv) No severe limitations due to the mass transport and the advanced potential perturbations, which allows the kinetic measurements with high time-resolution.

In situ ATR-SEIRAS technique represents a powerful method to qualitatively and quantitatively explore interfacial structures, reactions and pathways under steady-state as well as dynamic (time-resolved) conditions.

2.4 Electrochemical STM

As a complementary technique to SEIRAS, EC-STM was also employed in this dissertation work to obtain complementary spatially resolved structure information of the 2D supramolecular assemblies on substrates.

The combination of electrochemical measurements with *scanning tunneling microscopy* (STM) or *scanning probe microscopy* (SPM) provides opportunities to explore an interfacial system from the macroscopic scale down to microscopic level. The application of STM allows monitoring structures and processes at solid/liquid interfaces in situ with molecular/atomic resolution in real space.

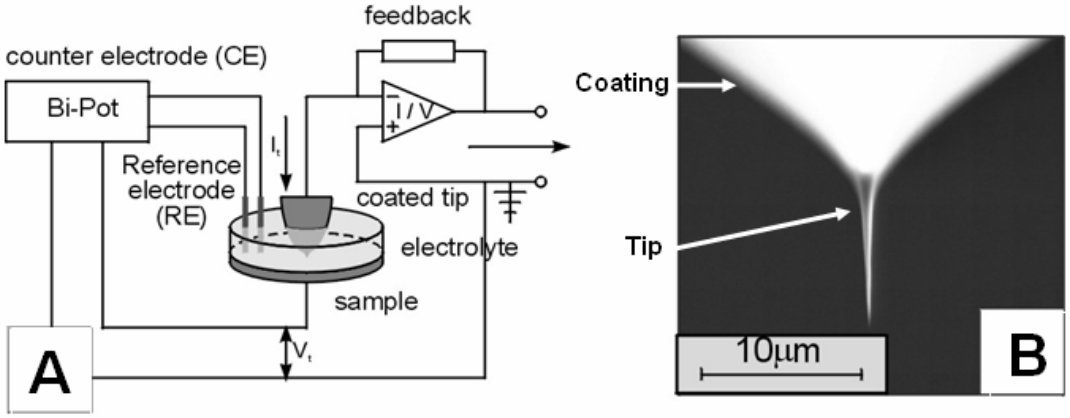

Fig. 2-14: (A) Schematic diagram of an electrochemical STM step-up; (B) polyethylene coated tungsten tip [7].

In an STM experiment a sharp metal tip is positioned close to the electrical conducting surface. Upon applying a voltage, a tunneling current will flow between the tip and the sample surface, which depends exponentially on the gap distance.

Scanning the tip in x-y directions allows imaging the contours of the electronic density of states at the Fermi level of the substrate with high spatial resolution.

Tunneling in electrochemical experiments takes place in an electrically conducting environment, the electrolyte. Electrochemical reactions may take place at the tip as well as at the sample, and superimpose on the tunneling current. Their potentials need to be strictly controlled, which is accomplished by a so-called bi-potentiostatic set-up (see Fig. 2-14A), with which the potentials of sample and tip, measured with respect to a suitable RE, can be chosen independently. Furthermore, the tip is coated with an inert and isolating layer (see Fig. 2-14B), made for example of polyethylene or electrophoretic paint, to minimize the contact with the electrolyte.

In summary, EC-STM provides general structure information of the 2D organization of supramolecular assemblies at electrochemical interfaces. In this dissertation work, EC-STM is applied to illustrate the overall ordered structure of the molecular adlayers and SAMs. The microscopic imaging results provide complementary support for most of the conclusions from in situ SEIRAS study.

2.5 Experimental Design

In the present dissertation work, the main objective is to comprehensively explore the general electrochemical properties and the molecular structures of two self-assembled systems, TMA adlayer and viologen SAMs. In situ SEIRAS characterization is applied simultaneously with two different electrochemical techniques, cyclic voltammetry and chronoamperometry, to explore quasi-steady-state structures and kinetic properties on single crystal and thin film gold electrodes. The idea is to use the carefully evaporated Au-films as a simulation to the Au(111) single crystal electrode. Each experiment covers the following procedures.

i) The self-assembled adlayers are prepared by either electrochemical adsorption from the bulk electrolyte (TMA and other carboxylic acids), or pre-assembly in another organic solvent before transfer into the supporting electrolyte (viologen samples);

ii) As a calibration, each system (both adlayers/SAMs and the electrolyte solution) is first characterized by CV and chronoamperometry on gold single crystal electrodes and subsequently on Au-film electrodes;

iii) The steady-state and dynamic in situ SEIRA spectra are recorded under electrochemical control (potential sweep or step) on Au-film electrodes. The electrochemical responses (CV, chronoamperometry) are recorded simultaneously with the SEIRAS measurements.

The details of materials and experimental setups will be presented in Chapter 3.

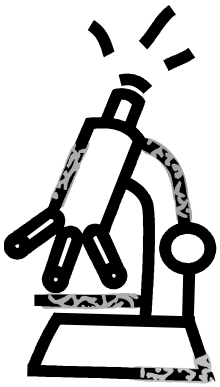

Chapter 3. Materials and Methods

3.1 Chemicals and Electrolyte Solutions

The solutions were prepared with Milli-Q water (18 MΩ cm, 2~ 3 ppb TOC). The glassware was cleaned either in caroic acid (peroxodisulfate, prepared from a 1:3 (volume ratio) mixture of 35% H_2O_2 solution and concentrated H_2SO_4) or from a 1:1 (volume ratio) mixture of hot H_2SO_4 and HNO_3, followed by copious rinsing with Milli-Q water. All electrolytes (EC, SEIRAS) were deaerated with argon before and during the experiments. The measurements were carried out at room temperature at 20 ± 0.5 ºC.

For the EC and spectroelectrochemical measurements of TMA and other carboxylic acids, 0.1 M $HClO_4$ was used as supporting electrolyte. For the viologen experiments, 0.05 M $KClO_4$ is employed as supporting electrolyte. The details of all chemicals used in the present experiments are listed below:

$HClO_4$: 70% solution, suprapure, Merck;

H_2SO_4 (for EC measurement): 96%, suprapure, Merck;

H_2SO_4 (for acidic cleaning mixture): 95 ~ 97 %, pro-analysis, KMF;

HNO_3 (for acidic cleaning mixture): 65 %, puriss., Riedel-de-Haen;

H_2O_2 (for the preparation of caroic acid): 35% (weight) solution, puriss. stabilized, KMF;

HCl: 30% solution, suprapure, Merck;

NaOH: 30 % solution, suprapure, Merck;

$KClO_4$: puriss. p.a., Fluka, twice recrystallized from water;

NH_4F (for Si substrate pre-treatment): 99.5+%, A.C.S. reagent, Aldrich;

Ethanol: for spectroscopy, Merck;

TMA: for synthesis, Lancaster, twice recrystallized in water;

Benzoic acid: standard for element analysis, Merck;

Isophthalic acid: for synthesis, Merck;

Viologen: as synthesized, see Section 3.7 for details of synthesis;

Argon: Argon-5.0, AIRLIQUID (Messer);

3.2 Au Working Electrodes

Gold (Au) is one of the most commonly used metal materials for electrodes in EC studies [6]. It is stable in a broad potential range and inert to many chemicals. Au electrodes are easy to prepare with different shapes and sizes. Furthermore, it is an ideal substrate material for the assembly of 2D supramolecular architectures due to the high affinity of Au to molecules via physical interactions or chemical bonds [6,11,24]. In addition, thin films of gold are commonly used as the substrates for spectroscopic and analytic experiments [6].

Several different types of Au electrodes were employed in the present dissertation work:

3.2.1 Au single crystal electrodes

The smooth Au(111) or stepped Au(n n n-2) = Au[n(111)-110] electrodes were single crystal cylinders of 4 mm height and 4 mm diameter. A gold wire was attached to the rear for mounting purposes. The massive gold single crystals were flame-annealed in a butane flame at red heat (~ 600 ºC) and then cooled in high purity argon before further treatment. In order to preserve the substrate Au(111)-(23×√3) reconstruction, the contact with the electrolyte was established under potential control [35].

The Au(111) disk-shape electrode for STM experiments is 10 mm in diameter and 2 mm height. It was annealed with a H_2 flame at red heat, and cooled in a high purity argon flow before further treatments and mounting into the EC cell of the STM [45].

3.2.2 Au-film electrodes

The film electrodes for SEIRAS measurements were prepared by electron beam evaporation (depositing rate 0.005 to 0.007 nm s^{-1}, base pressure < 2×10^{-7} mbar) of a thin gold film (25 nm mass thickness, monitored with a quartz crystal microbalance) onto the (111)-plane of a highly refractive Si hemisphere (> 6000 Ω cm). The Si substrate (Fig. 3-1A) was pre-treated by a short-time soaking in 40% (wt.) NH_4F solution to form a H-terminated Si surface [46], then the resulting Si-H surface was re-oxidized in hot HNO_3 solution to form a high quality Si oxide substrate for gold evaporation (Fig. 3-1B). The corresponding optical thickness d_o was estimated by ellipsometry to (23.5 ± 0.5) nm, which corresponds to a filling factor of 0.85 [35]. As shown in Fig. 3-1C, an AFM image of the as-evaporated film is composed of Au islands with preferentially (111)-oriented terraces.

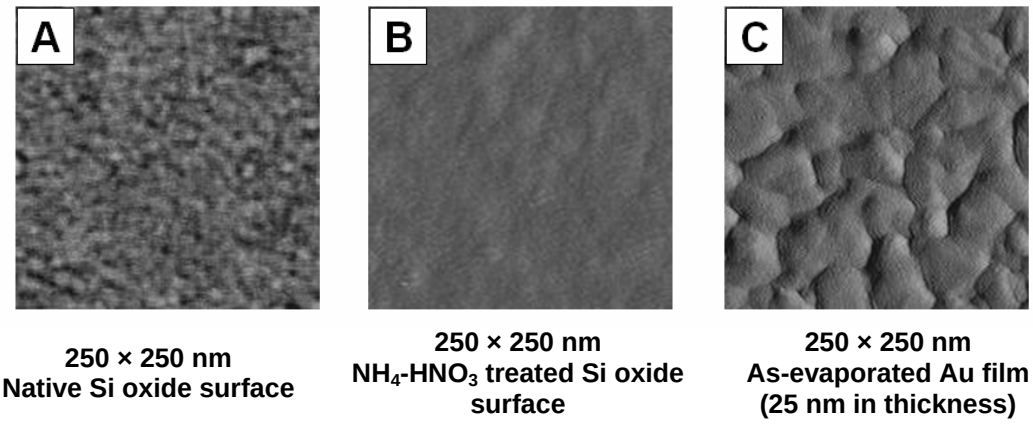

Fig. 3-1: AFM images of Si-substrates with a native oxide surface (A), pretreated by NH_4F-HNO_3 (B), and with evaporated Au film of 25 nm in thickness (C).

For the studies of anions/TMA adsorption, the as-evaporated film electrodes were first mounted onto the cell, and then brought into contact with the supporting electrolyte. Subsequently, the film was annealed by cycling the electrode potential with 50 mV s^{-1} in the double layer region (30 min for H_2SO_4, or 1 h for $HClO_4$). The increasing mobility of the gold surface atoms causes the healing out of surface defects and the preferential formation of larger (111) terraces.

The Au film electrodes for the viologen studies were directly brought into the assembly solution without annealing. After the self-assembly, the viologen modified

Au film electrodes were mounted onto the spectroelectrochemical cell under the protection of argon.

As one of the main ideas in our SEIRAS experiments, a Au-film is used as an approach for modeling the properties of a Au(111) single crystal surface in spectroelectrochemical studies. An electrochemical calibration will be given in Chapter 4.2.

3.2.3 Microelectrodes

Polycrystalline Au microelectrodes sealed in a glass capillary (Bioanalytical Systems, Inc, Ø = 10 μm) were first polished with Alumina slurry (Ø = 1 μm, 0.05 μm), then rinsed with Milli-Q water followed by treatments in an ultrasonic bath to remove the Alumina particles. Finally they were cleaned in concentrated H_2SO_4, and rinsed with Milli-Q water before further experiments.

3.3 Viologen SAM Preparation

The viologen monolayers were self-assembled on island-free unreconstructed Au(111)-(1×1) substrates, which were prepared by immersing a freshly flame-annealed electrode under potential control at 0.50 V (vs. SCE) into deaerated 0.1 M HCl. After a waiting time of 60 s to lift the surface reconstruction, the electrode was thoroughly rinsed with Milli-Q water to remove Cl^- [47]. The as-evaporated Au-film electrode was directly employed without further treatments.

The viologen monolayers were prepared by immersion of the gold electrodes in ethanolic solution of the respective viologen, followed by thermal annealing at 60 ^oC for 6 hours in the assembly solution to create an ordered high-coverage monolayer. The concentrations of viologens in EtOH solution were 1.0 mM for Au(111) single crystals and microelectrodes, and 0.5 mM for the Au(111-25 nm) film electrodes. The formation and characterization of the adlayers were strictly carried out in the absence of oxygen. A thermal incubation was carried out in a stainless steel autoclave to prevent the solvent from evaporation.

After the self-assembly, the modified Au-electrodes were rinsed with pure, warm ethanol to remove physisorbed viologens, subsequently dried in a stream of argon, and finally mounted onto the electrochemical or spectroelectrochemical cells.

3.4 Electrochemical Setup

3.4.1 Electrochemical cell

The electrochemical measurements of both single crystal and film electrodes were carried out in home-built 3-electrode EC cells (see Fig. 3-2). The working electrodes were fixed with Teflon or glass holders by employing the so-called "hanging meniscus technique" to avoid edge effects. The reference electrode (MSE, THE or SCE), located in the side compartment of a cell body, was connected to the WE through a Luggin-capillary to keep a high input impedance and to minimize the uncompensated solution resistance [48]. To avoid the interference from processes at the CE, the CE-compartment was usually separated from the main cell by a glass frit or a Teflon tap. Deaeration was adjusted through the solution under stirring before each measurement, and above the solution during the measurements to avoid the disturbance of electrode processes by argon bubbles.

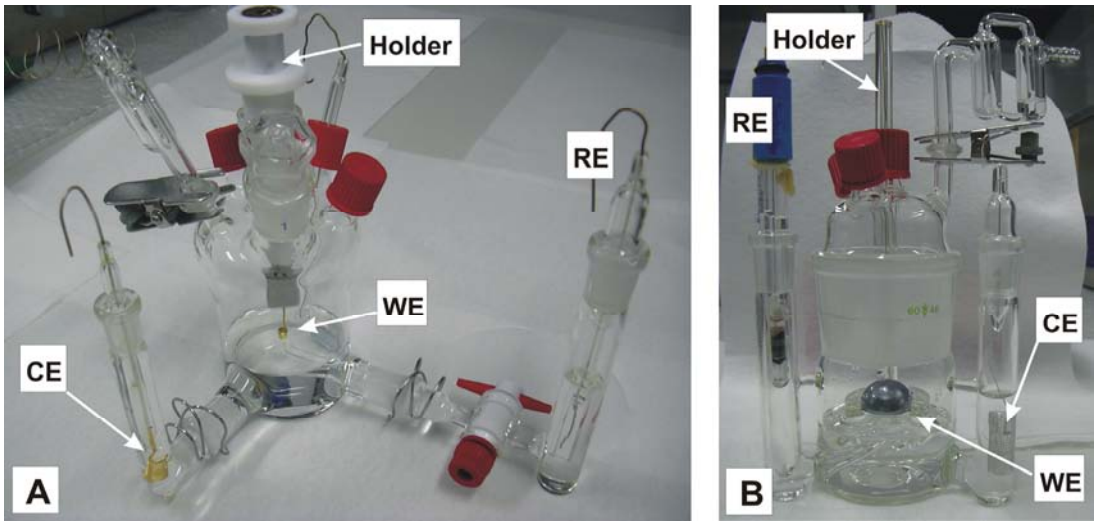

Fig. 3-2: Electrochemical cells for single crystal (A) and Au film (B) electrodes. Both types of electrodes were contacted to the electrolyte solution employing a "hanging meniscus" configuration.

3.4.2 Spectroelectrochemical cell

The SEIRAS experiments were carried out in a vertical spectroelectrochemical cell (Fig. 3-3) employing the Kretschmann ATR-configuration. The working electrode, a thin gold film on a Si-hemisphere "prism", was attached to the cell via a custom-made Teflon holder interspaced by a Kalrez O-ring to prevent electrolyte leakage. The geometric area of the electrode amounts to 1.53 cm^2. The current densities were calculated by referring to this value. The electrical contact of the gold film electrode to the potentiostat was established with a copper ring. The primary reference electrode (RE) was positioned close to the film surface via a luggin-capillary. The counter electrode was a large-area platinum spiral arranged in a centro-symmetric configuration with respect to the working electrode. Such a symmetric location of the CE is needed for fast measurements (i.e. in the high-frequency impedance mode). In addition, a second platinum wire served as an auxiliary electrode to decrease the time constant of the cell down to 5 μs [35].

Several inlets positioned on the upper cell compartment allowed the continuous purging of the electrolyte with argon and an easy access to titrate or to change the solution before and/or during a spectroelectrochemical experiment.

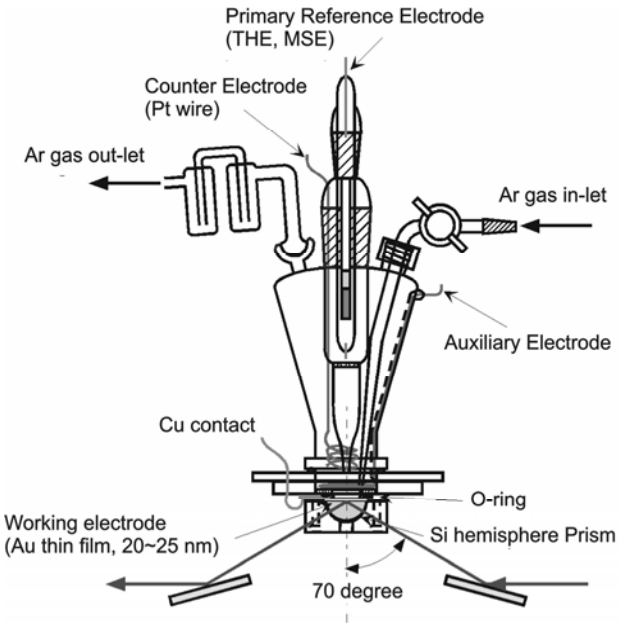

Fig. 3-3: Spectroelectrochemical cell with Kretschmann ATR-configuration [35].

During operation, the spectroelectrochemical cell was fixed onto a custom-designed holder to keep the Si prism inside the sample chamber of the spectrometer

under purging of dry air. The whole solution changing system was driven by an argon pressure control, in order to work in a completely O_2-free environment.

3.4.3 Potentiostats

Depending on different purposes, several commercial and custom-designed potentiostats were employed in the dissertation work.

i) An AutoLab (PGSTAT-30) potentiostat and a FHI (ELAB-200997) potentiostat were used for general single crystal experiments in electrochemical cell;

ii) A HEKA (PG-310) potentiostat was employed to control and synchronize the potentials of the film electrodes in the spectroelectrochemical cell during the in situ SEIRAS measurements;

iii) A home-built low current potentiostat (resolution < 10 fA) has been developed for the low-current measurement with microelectrodes and nanoelectrodes [49].

3.4.4 Reference electrodes

Reference electrodes used in electrochemical and spectroelectrochemical measurements were inserted in a special RE-compartment, or sometimes, directly located within the main cell body. Their relative potential scales are listed in Table 3-1 with reference to the RHE.

Table 3-1: Reference electrodes employed in the dissertation work [50,51].

Name and Abbreviation	Electrode reaction	Potential of reference vs. NHE /V
Normal hydrogen electrode, NHE	H_2/H^+ ($[H^+]$=1 M):	0
Mercury sulphate electrode, MSE	$Hg/Hg_2SO_4/Na_2SO_4$ sat.	0.64
Saturated calomel electrode, SCE	Hg/Hg_2Cl_2 sat. KCl	0.2412
Trapped (real) hydrogen electrode, (THE)	$Pt(H_2)/H^+$ consists of Pt in contact with hydrogen at 1 atm in the same solution as employed in electrochemical cells	c.a. 55 mV vs. NHE in 0.1 M H_2SO_4, 310 mV vs. SCE

All potentials in Chapter 4 and Chapter 5 were quoted with respect to the RHE. The potentials in Chapter 6 were quoted with respect to the MSE.

3.5 In situ SEIRAS

The infrared spectra were measured with a Bruker IF66 V/s Fourier Transform spectrometer. The spectral resolution was 4 cm^{-1} in slow-scan or rapid-scan, and 8 cm^{-1} in step-scan experiments. Nonpolarized infrared radiation from a globar source was focused onto the electrode/electrolyte interface by passing through the back of a Si prism. The incident angle was typically 70º referred to the surface normal. The IR radiation totally reflected at the interface was measured with a liquid-nitrogen cooled MCT detector (Model Colmar Technologies MCT 317).

During a steady-state or a kinetics study, the potential sweep or step modulations from the potentiostat were synchronized by triggering signals from the spectrometer. In the potential sweep experiments (10 mV s^{-1}), the spectrometer was operated in the slow scan mode. Typically, 160 sequentially acquired interferograms were co-added into each single beam spectrum. The potential step experiments were carried out either in the rapid-scan mode (28 ms time resolution, average of 256 traces) or in the step-scan mode (200, or 500 μs time resolution, 10 traces averaged, 1000 time slices). The spectra were plotted in absorbance units defined as $A = -\log(I/I_o)$ where I and I_o represent the intensities of the reflected radiation at the sample and the reference potentials, respectively.

3.6 Electrochemical STM

The in situ STM experiments were carried out with a Molecular Imaging Pico-SPM on disc-shaped Au(111) massive single crystal electrodes (10 mm diameter, 2 mm height). The STM tips were electrochemically etched tungsten or gold wires (0.25 mm diameter), coated with polyethylene. Pt wires served as reference and counter electrodes. All STM images were recorded at room temperature in constant current mode with tunneling currents ranging between 3 and 200 pA [45].

3.7 Synthesis of Viologen Samples

The synthetic strategy of the viologen derivatives HS-6V6-H (**1**) and HS-6V6-SH (**2**) was based on the nucleophilic substitution reaction between pyridines and terminal alkyl bromides (Scheme 3-1) [52].

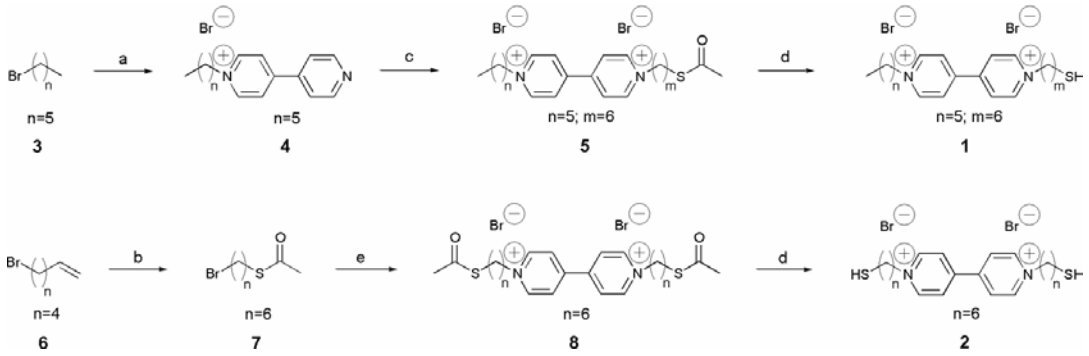

Scheme 3-1: Synthesis of the viologen monothiol (**1**) and dithiol (**2**). (a) 4,4´-bipyridine, $CHCl_3$, 90 °C, 16 h; (b) CH_3COSH, 1,1´-azobis(cyclohexanecarbonitrile), toluene, reflux, 1 h; (c) $Br(CH_2)_6SCOCH_3$, DMF, 110 °C, 24 h; (d) AcBr, MeOH, -78 °C to room temperature, argon atmosphere, 3 h; (e) 4,4´-bipyridine, DMF, 110 °C, 24 h. Other viologens with different alkane chain lengths were synthesized by ranging n and m values: n = 7, m = 8 for HS-8V8-H, and n = 9, m = 10 for HS-10V10-H.

HS-6V6-H (**1**): The viologen core was first mono-functionalized with a hexyl chain. 4,4'-bipyridine and the corresponding 1-bromo-n-hexane (**3**) were heated to 90 °C in chloroform in a pressure tube. The crude products were dissolved in dichloromethane and separated from the insoluble doubly substituted viologen derivatives by filtration to afford the desired mono-substituted viologen (**4**) in reasonable yields of 60 ~ 80 %. The nucleophilic terminal sulphur groups were masked as thioacetates [53]. The required bifunctional hexyl chain with a bromine atom at one end and an acetyl-protected sulphur at the opposite end (**7**) was synthesized from the bromohexene (**6**) and thioacetic acid in the presence of a radical source (yield 81 %) [54]. Bromohexene (**6**) was converted to (**7**) in good yields (81 %) by refluxing in toluene with thioacetic acid and 1,1'-azobis(cyclohexanecarbonitrile). The acetyl protected hexyl bromide (**7)** and the mono-hexylviologen derivative (**4)** were heated to 110°C in dimethylformamide (DMF) to form the acetyl-protected target structure (**5**) in very good yields (97 %). In variation of the literature procedure [53] we replaced acetylchloride by acetylbromide to form in situ HBr in methanol

under argon atmosphere to deprotect the acetyl groups of (**5**). HS-6V6-H (**1**) was isolated as pure bromide salt (yield 92 %) as confirmed by elemental analysis.

HS-6V6-SH (**2**): 2.3 equivalents of the terminally acetyl protected thiol-functionalized hexylbromide (**7**) were used to substitute both nitrogens of 4,4'-bipyridine. The acetyl protected target structure (**8**) was isolated in good yields (81 %) after crystallization from ethanol. The acetyl-protected viologen dithiol (**8**) was dissolved in methanol and an excess of acetylbromide was added at -78 °C to afford the desired viologen dithiol (**2**) after stirring at room temperature (yield 95 %).

Characterization:

N-Hexyl-N´-(6-thiohexyl)-4,4´-bipyridinium bromide, HS-6V6-H (1): Yellow solid. Mp. 274-275 ^{o}C; δ_H (300 MHz; MeOD; Me_4Si) 0.93 (t, 3H, CH_3, J=6.9 Hz), 1.30-1.70 (m, 12H), 2.04-2.20 (m, 4H), 2.52 (t, 2H, SCH_2, J=6.4 Hz), 4.77 (td, 4H, J=2.1, J=6.8 Hz), 8.70 (d, 4H, J=6.7 Hz), 9.30 (d, 4H, J=6.1 Hz); δ_C (75 MHz; MeOD; Me_4Si) 14.28, 23.49, 24.76, 26.65, 26.91, 28.67, 32.32, 32.44, 32.54, 34.78, 63.20, 63.30, 128.33, 147.10, 151.31; Elemental analysis calcd (%) for $C_{22}H_{34}Br_2N_2S$: C 50.97, H 6.61, N 5.40, found: C 50.69, H 6.52, N 5.68; m\z (MALDI TOF) 357.5839 [M^+-2Br].

N,N´-Bis(6-thiohexyl)-4,4´-bipyridinium bromide, HS-6V6-SH (2): Yellow solid (95 %). Mp. 263-265 ^{o}C; δ_H (300 MHz; MeOD; Me_4Si) 1.38-1.58 (m, 8H), 1.64 (q, 4H, J=7.0 Hz), 2.11 (q, 4H, J=7.6 Hz), 2.51 (t, 4H, J=6.8 Hz, SCH_2), 4.75 (t, 4H, J=7.5 Hz, NCH_2), 8.69 (d, 4H, J=6.6 Hz), 9.29 (d, 4H, J=6.6 Hz); δ_C(75 MHz; MeOD; Me_4Si) 25.65, 27.45, 29.60, 33.21, 35.60, 64.10, 129.31, 148.10, 152.32; Elemental analysis calcd (%) for $C_{22}H_{34}Br_2N_2S_2$: C 48.00, H 6.23, N 5.09, found: C 48.27, H 6.49, N 5.05; m\z (MALDI TOF) 390.0631 [M^+-2Br].

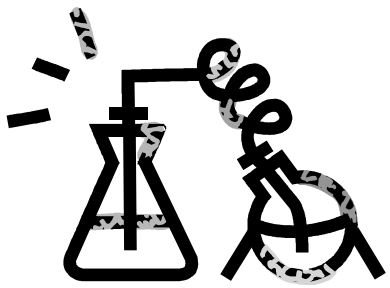

Chapter 4. Electrochemical Double Layer Structure

4.1 Introduction

The structures and compositions of the electrochemical double layer have been widely investigated with focus on the adsorption of anion/cation and water species. For example, the adsorptions of sulphate (SO_4^{2-}), perchlorate (ClO_4^-) and halide anions (F^-, Cl^-, Br^-, I^-) on Au(111) have been systematically investigated by cyclic voltammetry [55,56,57], chronocoulometry [58,59,60], radiochemistry [61], LEED, AES [62, 63, 64], microgravimetry [65], SHG [59], in situ STM and AFM [57,66,67,68,69,70,71], as well as by several different IR-spectroscopy methods [67,72,73,74]. SO_4^{2-} and ClO_4^- can be directly detected by IR spectroscopy because the S-O or Cl-O stretching modes are IR-active, which facilitates the simultaneous monitoring of anions and co-adsorbed water species in the interfacial range. ATR-SEIRAS characterizations of the electrochemical double layer in the presence of SO_4^{2-} and ClO_4^- have been reported recently [72,75,35,76]. We refer to these SEIRAS measurements in order to confirm the performance of our spectroelectrochemical setup.

This chapter is organized as follows: at first we calibrate the morphological and electrochemical properties of the quasi-Au(111-25 nm) film electrodes. The second part focuses on a SEIRAS study of the adsorption behavior of sulphate anions. Finally we will discuss the structure of co-adsorbed H_2O species. In addition, the investigation on SO_4^{2-} adsorption is compared with that of ClO_4^-.

4.2 Characterization of the Au Electrodes

As shown in the AFM image in Fig. 3-1, the Au (111-25 nm) film electrode prepared by electron-beam evaporation consists of preferentially (111) oriented

islands with an average diameter ranging between 30 ~ 50 nm. The Au film was employed in the spectroelectrochemical experiments to approach the properties of a Au(111) single crystal substrate. Because the structure of SO_4^{2-} adlayer is strongly dependent on orientation, average size of terraces, and defect density of the substrates, the CV responses upon SO_4^{2-} adsorption provide a good calibration to characterize the properties of the fabricated Au films.

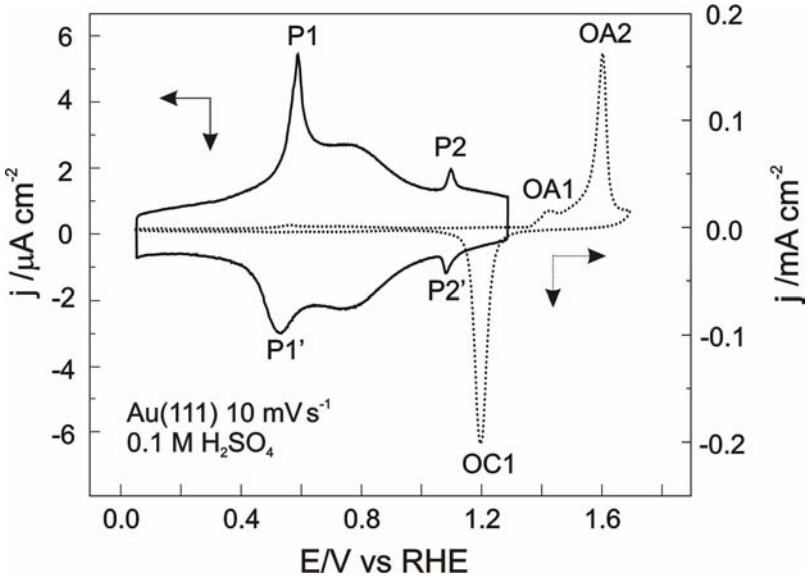

Fig. 4-1: CVs of a Au (111-20 nm) film electrode in contact with 0.1 M H_2SO_4, scan rate 10 mV s^{-1}. Solid line: CV in the double layer region; Dotted line: CV with excursion into the oxidation region.

Before each measurement, the Au film was electrochemically annealed by cycling the potential in the double layer region at 50 mV s^{-1}. Fig. 4-1 shows the typical CVs of a Au film, obtained after 30-min electrochemical annealing in 0.1 M H_2SO_4 solution. The CV exhibits well-defined features for the lifting of the ($p \times \sqrt{3}$) reconstruction (P1) and the disorder/order phase transition of an ($\sqrt{3} \times \sqrt{7}$) (hydrogen) sulphate overlayer (P2/P2´) [55,56,69]. Further potential excursion into the so-called oxidation region, at E > 1.30 V (RHE), shows a shoulder OA1 corresponding to the oxidation of step sites, and the characteristic peak OA2, which represents the oxidation of (111) terraces [56]. These properties are typical for the CV of a Au(111) single crystal electrode.

We compared the voltammetric profiles of the electrochemically annealed Au film electrodes with the responses of a series of stepped single crystals Au[n(111)-(110)] in 0.1 M H_2SO_4 (Fig. 4-2).

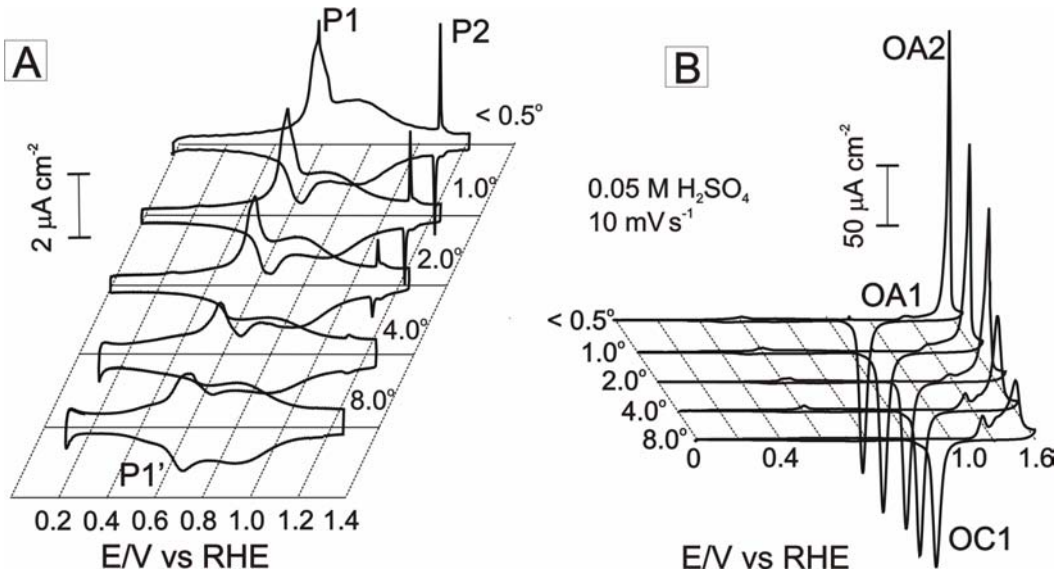

Fig. 4-2: CVs of a series of stepped single crystals Au(n n n-2) = Au [n(111)-(110)] in 0.1 M H_2SO_4, scan rate 10 mVs^{-1}. (A) CV series in the double layer potential range; (B) CV series with excursion to oxidation-reduction potentials. The miscut angles are indicated in the figures.

A miscut of a Au(111) electrode in its (110) direction generates steps along the (100) direction. Such stepped Au[n(111)-(110)] single crystals have different step densities along the (110) direction, which leads to various miscut angles. They can be used as internal standards. The evolution of the reconstruction peak P1, the pair of voltammetric peaks P2/P2´, and the sharp terrace oxidation peak OA2, demonstrates that the Au film electrodes exhibit responses comparable to a stepped Au(111) electrode with an equivalent miscut angle ranging between 2° ~ 4° , which relates to an average size of ideally smooth terraces of 19 ~ 27 atoms [35].

The CVs of the Au(111-20 nm) film electrode recorded in 0.1 M $HClO_4$ solution are shown in Fig. 4-3. A pair of weak current peaks P1/P1´ is observed at around 0.68 V and 0.62 V, corresponding to the adsorption/desorption of ClO_4^- respectively. The difference between the two anions will be further addressed by SEIRAS in Section 4.3.2. The oxidation peak OA1 at 1.30 V corresponds to the oxidation process on steps, whereas OA2 and OA3 at 1.36 and 1.52 V represent the first and second ET during the oxidation on terrace sites, respectively [56].

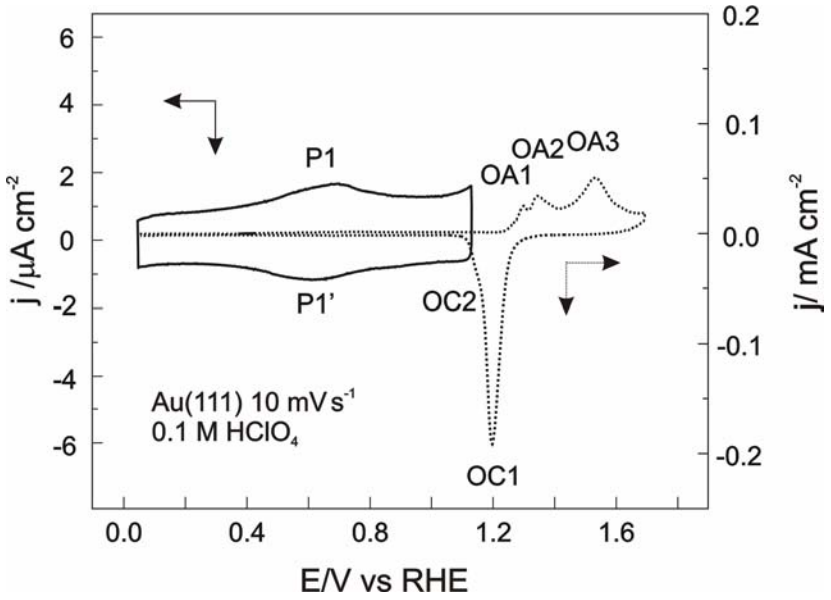

Fig. 4-3: CVs of a Au (111-20 nm) film electrode in contact with 0.1 M $HClO_4$, scan rate 10 mV s^{-1}. Solid line: CV in the double layer region; Dotted line: CV with excursion into the oxidation region.

The above CV results suggest that the Au film electrodes employed in the present ATR-SEIRAS study represent a good approximation to an ideal Au(111) single crystal electrode.

4.3 SEIRAS Study of Anion Adsorption

Based on the understanding from the electrochemical characterization, the structure properties of the electrode/electrolyte interface can be further explored by in situ SEIRAS.

4.3.1 Sulphate/perchlorate adsorption overview

Fig. 4-4A shows a typical series of SEIRA spectra for Au(111-20 nm)/0.1 M H_2SO_4 measured in the double layer region during a positive potential sweep. A single beam spectrum acquired at 0.1 V was chosen as reference, which is outside the potential region of specific adsorption of sulphate species [35]. As the potential advances to more positive values, negative-going bands start to appear at 3500 cm^{-1} and at 1615 cm^{-1}, corresponding to OH-stretching (ν_{OH}) and HOH-bending (δ_{HOH}) modes of interfacial water, respectively [35,72,77,78]. The negative sign of these bands indicates that the exclusion of the initially adsorbed water species from the

interface. Their intensities are continuously increasing in negative direction until a maximum is reached around 0.55 V, which is close to the chronocoulometrically estimated potential of zero charge (E_{pzc}) [59]. At E > 0.55 V a new positive-going band appears around 1100 cm^{-1}, which is attributed to the $\nu_{S\text{-}O}$ mode of adsorbed sulphate species [72]. Its intensity increases with positively potential sweeping, and reaches a maximum at about 1.10 V. Simultaneously, positive-going bands start to appear at 3460 cm^{-1} and 1650 cm^{-1}, corresponding to the ν_{OH} and δ_{HOH} vibrations of interfacial water. Their characteristic band shapes and positions at E > 0.55 V suggest significant differences from the initial water structure in the potential range below 0.55 V.

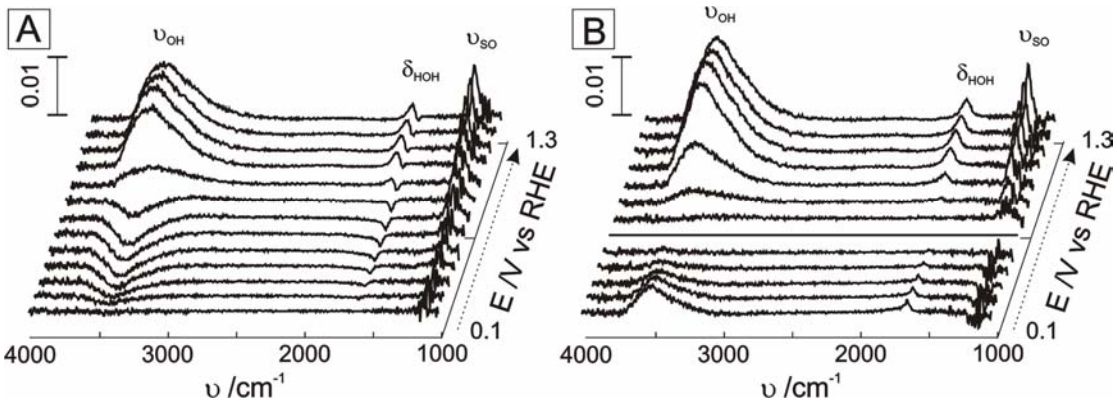

Fig. 4-4: (A) Series of SEIRA spectra of Au(111-20 nm)/0.1 M H_2SO_4 as a function of potential. The spectra were acquired during a potential sweep (5 mV s^{-1}) between 0.1 V and 1.3 V vs. RHE. The reference potential was 0.1 V. (B) Recalculated SEIRA spectra with the single beam spectrum recorded at 0.55 V as the new reference [35].

Fig. 4-5A shows SEIRA spectra for the a Au(111-20 nm) film electrode in 0.1 M $HClO_4$ solution. The reference spectrum was measured at 0.1 V. The positive-going band at around 1130 cm^{-1}, which is assigned to the Cl-O stretching mode ($\nu_{(Cl\text{-}O)}$) of perchlorate ions, increases in intensity with increasing potential. The $\nu_{(O\text{-}H)}$ and $\delta_{(HOH)}$ modes of water appear in 3700~2800 and 1650~1620 cm^{-1}, respectively. The intensities of water bands increase in the negative direction at E < 0.60 V and in the positive at E > 0.60 V. In the latter potential range two different water species can be distinguished as indicated by the $\nu_{(O\text{-}H)}$ bands at 3600 and 3250 cm^{-1}.

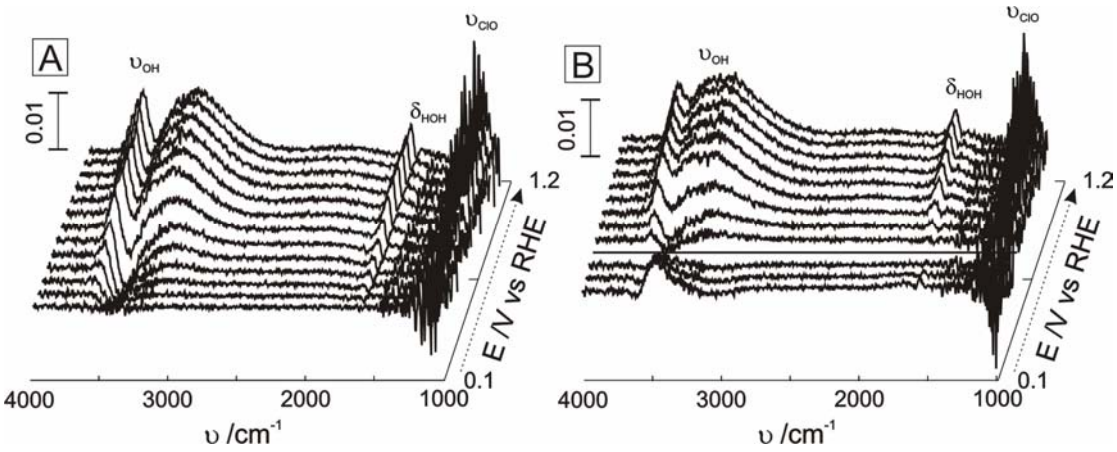

Fig. 4-5: (A) Series of SEIRA spectra of Au(111-20 nm)/0.1 M $HClO_4$ as a function of potential. The spectra were acquired during a potential sweep (10 mVs^{-1}) between 0.1 V and 1.3 V vs. RHE. The reference potential was 0.1 V. (B) Recalculated SEIRA spectra with the single beam spectrum recorded at 0.60 V as the new reference.

Further discussion on the co-adsorbed water structures will be given in Section 4.3.3. In this section we first focus on the specific adsorption of anions.

4.3.2 Specific adsorption

As described in the overview, the adsorption of sulphate is indicated by the $\nu_{(S\text{-}O)}$ vibrational band around 1100 cm^{-1}, which grows in intensity with increasing electrode potential (Fig. 4-4). This band can be either assigned to the triply degenerate ν_3-mode of sulphate with dominating contributions from S-O (of uncoordinated oxygen [79]) to the totally symmetric ν'_3-mode of SO_3, or the doubly degenerate ν_4 mode of the coordinated SO_3-unity in hydrogen sulphate [35,80,81,82]. Such a 3-fold coordination is supported by the results of H_2SO_4 concentration and pH dependence experiments [35], as well as by ab initio calculations [83,84]. A similar intensity evolution of the $\nu_{(Cl\text{-}O)}$ mode is observed in Fig. 4-5. This can be attributed to the same three-fold coordination of ClO_4^- as for SO_4^{2-}.

The nature of adsorption can be more convincingly addressed by the dependence of the vibrational frequencies on the applied substrate potential, which reflects the strength of both inter-adsorbate coupling and adsorbate/substrate interaction [85]. The vibrational frequencies (band positions) of the $\nu_{(S\text{-}O)}$ and $\nu_{(Cl\text{-}O)}$ modes from Fig. 4-4 and Fig. 4-5 are plotted against the electrode potential in Fig. 4-6.

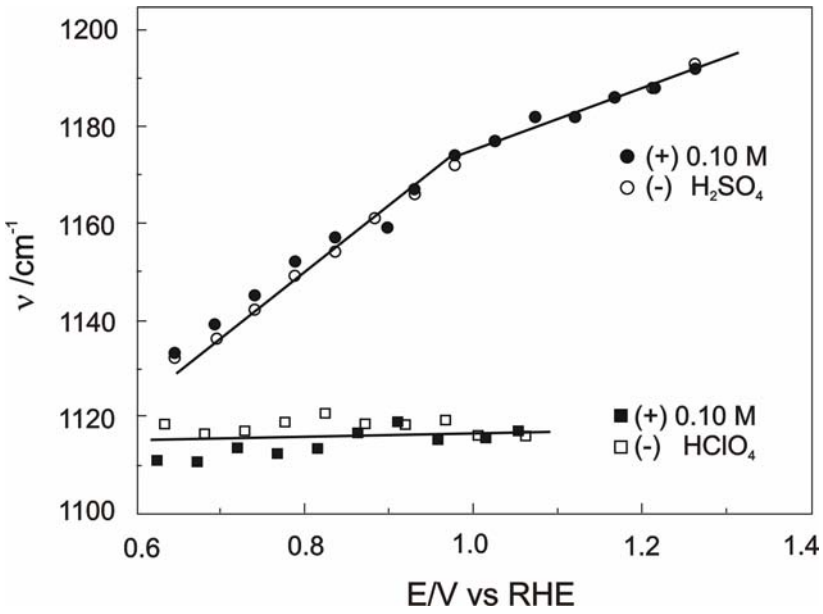

Fig. 4-6: Plots of the peak positions of the $\nu_{S\text{-}O}$ and $\nu_{Cl\text{-}O}$ bands as the function of the electrode potential.

The $\nu_{(S\text{-}O)}$ band shifts to higher wavenumbers with increasing potential. The $\nu_{(S\text{-}O)} \sim E$ dependence is characterized by two linear segments with $\Delta\nu_{(S\text{-}O)}/\Delta E = (132 \pm 5)$ cm^{-1} /V at $E < E_{P2/P2'}$ (~ 1.0 V) and $\Delta\nu_{(S\text{-}O)}/\Delta E = (62 \pm 3)$ cm^{-1} /V at $E > E_{P2/P2'}$, corresponding to the disordered and the ordered ($\sqrt{3} \times \sqrt{7}$) sulphate adlayer, respectively. The smaller slope of the latter indicates a strong and uniform lateral interaction between the neighboring SO_4^{2-} anions, which are bridged via $H_5O_2^+$ ions [35,72]. The change in the slope appears close to the potential of the disorder/order transition (see CV in Fig. 4-1).

The potential-induced shift of the $\nu_{(Cl\text{-}O)}$ band ($\Delta\nu_{(Cl\text{-}O)}/\Delta E < 10$ cm^{-1}/V) is much smaller than for the $\nu_{(S\text{-}O)}$ band. The weak potential dependence of the $\nu_{(Cl\text{-}O)}$ frequency indicates a weak interaction between the ClO_4^- and the substrate. Although a larger $\Delta\nu_{(Cl\text{-}O)}/\Delta E$ value (55 cm^{-1} /V) has been reported at a higher $HClO_4$ concentration (0.5 M) [75], the SEIRAS results clearly support that ClO_4^- is much less specifically adsorbed on the Au film substrate.

4.3.3 Structure of co-adsorbed water

The structure of water species is strongly related to the nature of co-adsorbed anions and metal electrodes [76]. Although both interfacial and bulk water give strong IR absorbance, the signal from interfacial water can be easily distinguished in

potential-different SEIRAS spectra due to the dominating contribution from the first and second adlayers.

In the SEIRA spectra choosing reference potential at 0.10 V (Fig. 4-4A), the superposition of positive and negative-going $\nu_{(O-H)}$ modes complicates the analysis. In order to deconvolute the contributions of different interfacial water species, we follow the strategy proposed by Osawa et al. [75], and choose the one recorded at 0.55 V as a new reference spectrum, which is approximately at the E_{pzc} of the Au film electrode [35]. The selection of the new reference is based on the experimental observations, that the intensity of the negative-going interfacial water bands ($\nu_{(O-H)}$ ~ 3500 cm^{-1} and $\delta_{(HOH)}$ ~ 1615 cm^{-1}) remains constant at 0.55 V, and that the different vibrational modes ($\nu_{(O-H)}$ ~ 3460 cm^{-1} and $\delta_{(HOH)}$ ~ 1650 cm^{-1}) appear at E > 0.55 V. Water molecules are proposed to lie nearly flat, i.e. with their dipole axis parallel to the electrode surface at the E_{pzc} [35,86]. Based on the surface selection rule of SEIRAS, the reference spectrum contains no contribution from any $\nu_{(O-H)}$ and $\delta_{(HOH)}$ modes of adsorbed water, thus represents the exact intermediate state between the initial water species and the new ones co-adsorbed with anions.

Fig. 4-4B shows the recalculated SEIRA spectra of Au(111-20 nm)/0.1 M H_2SO_4 with the reference potential at 0.55 V (~ E_{pzc}). The $\nu_{(O-H)}$ and $\delta_{(HOH)}$ modes of the initially adsorbed water appear at 3500 and 1615 cm^{-1} at E = 0.1 V, and decrease in intensity with increasing potential. They disappear completely at E ~ E_{pzc}. These water bands at E < E_{pzc} represent weakly hydrogen-bonded water, with the hydrogen atoms pointing toward the electrode [72,35]. In addition, a broad feature around 1700 cm^{-1} indicates the co-adsorption of H_3O^+ in the second layer. In a small potential range, E_{pzc} < E < 0.9 V, new $\nu_{(O-H)}$ and $\delta_{(HOH)}$ modes appear at 3150 and 1612 cm^{-1}, corresponding to strongly hydrogen-bonded water. The intensities of the $\nu_{(O-H)}$ and δ_{HOH} bands increase rapidly with increasing potential until the disorder/order transition of the SO_4^{2-} adlayer at E ~ 1.0 V. Water species co-adsorbed with the ordered SO_4^{2-} adlayer show the $\nu_{(O-H)}$ and $\delta_{(HOH)}$ bands at 3460 and 1650 cm^{-1}, indicating contribution from the $H_5O_2^+$ ions hydrogen-bonded to SO_4^{2-} in a few layers next to the electrode. These conclusions are illustrated by the models in Fig. 4-7.

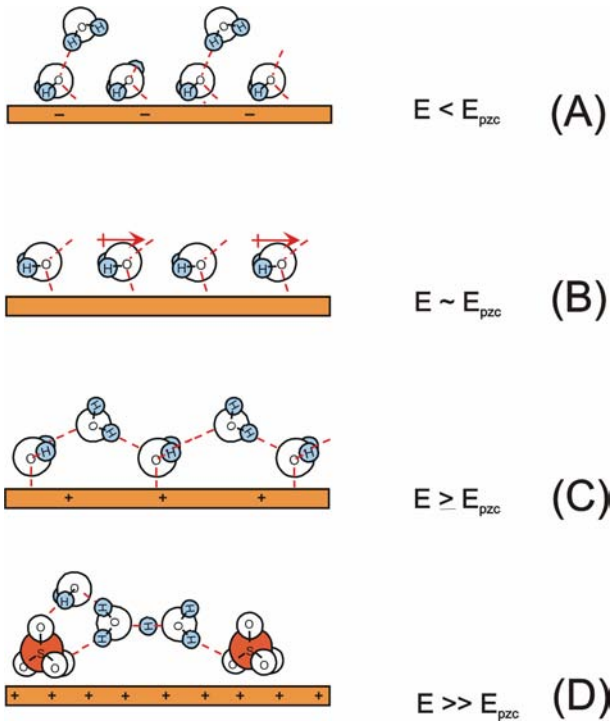

Fig. 4-7: Proposed models of the interfacial structures at various characteristic potential regions [40].

Employing the same deconvolution strategy, the SEIRA spectra of Au(111-20 nm)/0.1 M $HClO_4$ were recalculated. The chosen reference potential was 0.60 V (~ E_{pzc}). The data are presented in Fig. 4-5B. The $\nu_{(O-H)}$ and $\delta_{(HOH)}$ modes at 3460 and 1610 cm^{-1} at $E < E_{pzc}$ are attributed to weakly hydrogen-bonded water species, similar to that for H_2SO_4. However, two $\nu_{(OH)}$ modes appear as a broad band around 3250 cm^{-1} and a narrow one at 3600 cm^{-1} at $E > E_{pzc}$ upon the adsorption of ClO_4^-. The former represents strongly hydrogen-bonded water species. The latter gives a high $\nu_{(OH)}$ frequency close to that of non-hydrogen-bonded isolated water in the gas phase (~ 3660 cm^{-1}) [75]. Such assignments are in agreement with the non-specific adsorbing nature of ClO_4^-, as already discussed in Section 4.3.2. The interaction between "isolated" water molecules and ClO_4^- is much weaker than that for SO_4^{2-}. The further analysis on the detailed potential dependencies of the $\nu_{(O-H)}$ frequencies and the FWHM allow distinguishing different interfacial water species in a more convincing way.

Although the deconvolution of water bands employed in the above discussion is somewhat arbitrating, it provides a useful strategy to explore the diverse nature of interfacial water. Similar methods will be applied in Chapter 5.

4.4 Summary

As a preparative part, this chapter focuses on the characterization of quasi-Au(111) film electrodes, together with some fundamental SEIRAS investigations on the double layer structure upon the adsorption of SO_4^{2-} and ClO_4^- anions.

The CVs of Au(111-20 nm) film/ 0.1 M H_2SO_4 show similar responses to that of typical Au(111) single crystal electrodes. Calibration with a series of stepped Au(111) single crystals indicates that the Au film electrodes in a SEIRAS experiment can be used as a good approach to the Au(111) single crystal electrodes.

In further SEIRAS studies, specific/non-specific adsorption and different types of co-adsorbed water species can be distinguished by analyzing the intensities and frequencies of their vibrational bands during a potential modulation.

Based on the above fundamental results, ATR-SEIRAS represents a powerful molecule/ion-specific probe for electrochemical interfaces to explore interfacial structures, reaction pathways under steady-state and dynamic (time-resolved) conditions. The applications of ATR-SEIRAS in the 2D phase transition of organic adlayers and the redox ET properties of functional SAMs will be respectively presented in Chapter 5 and in Chapter 6.

Chapter 5. TMA and Carboxylic Acids

5.1 Introduction

5.1.1 Building blocks for self-assembly

Carboxylic acids, especially those with symmetric centers like phenyl rings, play important roles as functional pattern-controlling units in crystal engineering and supramolecular assembly. As shown in Scheme 5-1, *benzoic acid* (1 - benzenecarboxylic acid, BA), *terephthalic acid* (1,4 - benzenedicarboxylic acid, TA), *isophthalic acid* (1,3 - benzenedicarboxylic acid, IA), and a wide variety of their derivatives are well known to form one-dimensional tapes and ribbons, 2D networks, or 3D bulk crystals based on the formation of hydrogen-bonds between two or more neighboring molecules [87,88,89,90]. As a typical example, *trimesic acid* (1,3,5 - benzenetricarboxylic acid, TMA), which is composed of a phenyl ring and three trigonally arranged exodentate carboxyl groups, provides an organic template [91,92]. Together with its metal complexes, TMA represents a prototype material for supramolecular assemblies involving directional hydrogen-bonding and metal ion/ligand coordination [92, 93, 94, 95, 96, 97, 98, 99, 100, 101, 102, 103].

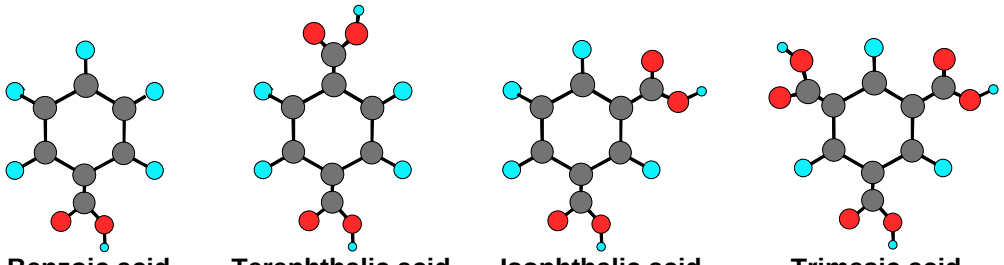

Scheme 5-1: Molecular structures of the different phenyl ring-based carboxylic acids.

5.1.2 STM studies in UHV and in electrolyte solutions

The assembly of TMA on surfaces was recently studied under UHV conditions [104, 105] and at electrified solid/liquid interfaces [106, 107]. Many different structures have been observed by using scanning tunneling microscopy (STM).

Griessl et al. [104] reported the coexistence of two hexagonal ring structures composed of TMA with hydrogen-bonds formed either between two (“chicken wire” or “honeycomb” motif) or three (“flower” motif) adjacent molecules on highly oriented pyrolytic graphite (HOPG). The structure of the SAM can be controlled by adjusting experimental parameters like temperature or concentration. Dmitriev et al. [105] reported in a temperature-dependent study on Cu(100) two different 2D structures: a honeycomb structure at low temperature (200 K), and a more densely packed stripe arrangement at room temperature. The latter was assigned to upright standing TMA molecules which are adsorbed on Cu(100) via one or two carboxylate groups.

Compared with temperature and concentration, electrochemistry allows employing the electrode potential as “steering” parameter. Under electrochemical conditions, Ishikawa et al. found for Au(111)/0.1 M $HClO_4$ a honeycomb-type (8 × 8) 2D network of flat oriented TMA molecules, which transforms at higher potentials into a close-packed structure of dimers [106]. Under similar experimental conditions Su et al. [107] found three ordered adlayers: a quasi-hexagonal (4 × 4) phase of planar oriented molecules at low coverage, a mixed (5 × 2√3) adlayer and a striped phase represented by (2√3 × 4√3) or (7 × 2 √3). The latter was tentatively ascribed to perpendicularly adsorbed molecules. Furthermore, the potential-induced adsorption and self-assembly of TMA were investigated at the electrified Au(111)/0.05 M H_2SO_4 interface by in situ STM in our recent study [45]. Several new structures and phase transition features based on STM result will be briefly discussed in this chapter.

Despite the general structure information, the above STM results do not provide a direct insight into chemical composition, interactions within TMA adlayers, and the formation/dissolution kinetics between the different adlayer phases. These details can be obtained from surface spectroscopic experiments, especially IR spectroscopy. The adsorption of BA [43,108,109], as well as its derivatives like p-nitrobenzoic acid [43], fluorobenzoic acid [110] and terephthalic acid [111] on Au, Pt, and Ag electrodes were studied by in situ IR methods. On these electrode surfaces, the above mentioned acids are physisorbed with planar oriented phenyl rings at negative potentials, and chemisorbed in tilted or perpendicular ring-orientations at positive potentials accompanied by the deprotonation of carboxylate groups. A blue shift of the

symmetric stretching vibrational band of deprotonated -COO^- around 1370~1400 cm^{-1} was observed with increasing potential, which was explained as a result of the intermolecular dipole-dipole coupling. However, the information accessible from traditional electrochemical in situ IR methods (employing a thin layer configuration) is very limited [40,112]. For example, very little knowledge from co-adsorbed anions and H_2O species can be obtained.

Since the pioneering application of surface enhanced infrared absorption spectroscopy (SEIRAS) in electrochemical studies by Osawa et al., several examples of benzenecarboxylic acids were studied by steady-state (equilibrium) SEIRAS. In the light of the surface selection rule, potential-induced orientation changes were confirmed for the adsorption of fumaric acid [113] and p-nitrobenzoic acid [114] on Au film electrodes. Furthermore, the comprehensive analysis of SEIRAS band intensity, peak position, and FWHM reveals changes of the substrate/adsorbate interactions, surface coverage and surface order. Similar potential dependencies of molecular orientation and adlayer structure were also found in several other systems, such as 4,4'-bipyridine [13], p-nitrobenzoic acid (on silver) [43], cytosine [115], uracil [116].

5.1.3 Kinetic studies by SEIRAS

The kinetics of carboxylic acid adlayer phase transition was also investigated by time-resolved SEIRAS in combination with electrochemical chronoamperometry. The adsorption of fumaric acid on a Au(111) electrode shows a Langmuir type kinetics, indicating a random adsorption without any lateral interactions, while an instantaneous nucleation-growth mechanism was suggested for its desorption process, which starts from holes in the adlayer [113]. In case of p-nitrobenzoic acid, the analysis of the SEIRAS intensity suggests first a random adsorption, and then a reorientation accompanied by a nucleation-and-growth mechanism [114]. Similar multi-step phenomena were also reported in our recent work on uracil [116], in which the dissolution of chemisorbed uracil comprises at least three contributions: (i) Perpendicularly oriented uracil molecules change their orientation toward a tilted or planar arrangement depending on the final potential; (ii) Desorption of strongly hydrogen-bonded second-layer water and sulphate species; (iii) Second-layer adsorption of weakly hydrogen-bonded water.

5.1.4 Our strategy

In this chapter we present a comprehensive in situ ATR-SEIRAS study on TMA adsorption on quasi-single crystalline Au(111 - 25 nm) film electrodes in contact with aqueous 3 mM TMA/0.1 M $HClO_4$. First, we describe the steady-state properties of the potential dependent adlayer structures with special emphasis on substrate/adsorbate interaction, intermolecular hydrogen-bonding, and the role of interfacial water. The second part of this chapter is to explore the kinetics of phase formation employing time-resolved SEIRAS in rapid-scan and step-scan regimes. A comparison with BA and IA adlayer structures will be discussed separately. All spectroscopic results will be compared with in situ STM and electrochemical experiments employing well-defined single crystal electrodes.

5.2 TMA

5.2.1 Steady-state experiments

If a potential sweep is slow enough to keep the equilibrium of charge transfer and mass transport between the interface and the bulk electrolyte solution, potential-induced structure or chemical changes are quasi-stationary and thermodynamically equilibrated during the CV experiment. Slow scan CV measurements were employed to explore the potential-dependent quasi-steady-state properties of TMA on gold electrodes.

5.2.1.1 CV and STM

Fig. 5-1A shows typical CVs of Au(111) in 0.1 M $HClO_4$ solution in the absence (dotted line) and in the presence (full and dashed line) of 3 mM TMA. The experiment started with a thermally reconstructed Au(111)-electrode immersed in the electrolyte at 0.30 V. The trace represented by the solid line was recorded after three subsequent cycles in the double layer region. The CV in dashed line was obtained after 10 min of cycling the potential in the range between 0.85 and 1.20 V. Four characteristic potential regions (labeled I, II, III_a and III_b), which are separated by the current peaks $P_1/P_{1'}$, $P_2/P_{2'}$ and P_3, can be readily distinguished. Based on previous in situ STM experiments, the following tentative assignment is suggested [45,107]. During the positive potential scan, a physisorbed adlayer develops in region I,

followed by a transition phase II ($E > P_1 = 0.59$ V), which transforms into a chemisorbed adlayer at $E > 0.76$ V (P_2). The chemisorbed region III is further separated into III_a and III_b by a broad current peak P_3 at $E \sim 0.88$ V indicating a slow disorder/order transformation [45]. Extended potential cycling in region III_b facilitates the formation of a long-range ordered chemisorbed adlayer. The subsequent dissolution during a negative potential sweep gives rise to a characteristic cathodic current peak P_2´.

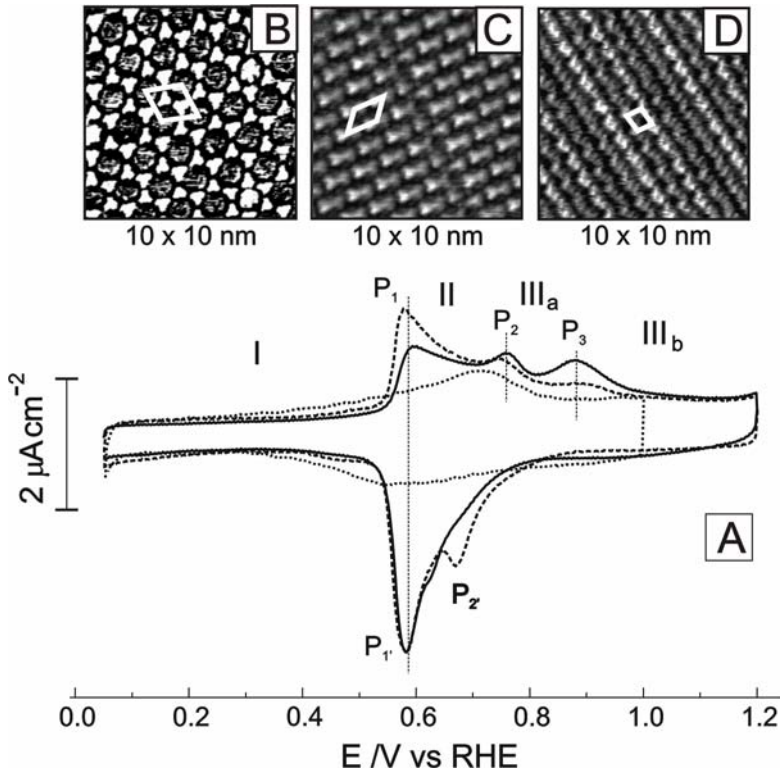

Fig. 5-1: (A) CVs of an ideal Au(111) electrode (miscut angle < 0.2°) in 3 mM TMA/0.1 M $HClO_4$, scan rate of 10 mV s^{-1}. The solid line represents the steady-state CV recorded after three complete potential cycles, the dashed line was obtained after 10 min cycling in 0.85 V to 1.20 V. The CV in TMA-free base-electrolyte is plotted as dotted line. The different adlayer regions labeled I, II, III_a and III_b. High-resolution in situ STM images (B), (C) and (D) represent the ordered phases recorded at 0.10 V, 0.70 V and 1.0 V, respectively [45].

The in situ STM images in Fig. 5-1 B, C and D demonstrate the molecular arrangements of TMA in the three ordered phases I, II and III_b, respectively. Fig. 5-1 B shows the open honeycomb pattern of planar oriented, physisorbed TMA molecules, which are connected by symmetric hydrogen-bonds between neighboring carboxyl groups (dimer motif). The rhombohedral unit cell with a = (1.65 ± 0.08) nm and α =

$(60 \pm 6)^o$ contains two molecules, which gives rise to a coverage of $\Gamma_{mI} = (1.4 \pm 0.2)$ 10^{-10} mol cm^{-2} or an area per molecule of $A_I = (1.18 \pm 0.06)$ nm^2. Similar structures were reported previously under UHV conditions as well as in solution on HOPG, Cu(100) and Au(111) [45,104,105,106,107]. At higher electrode potentials, in region II (Fig. 5-1C), an assembly of physisorbed quasi-linear rows is observed. Within the rows adjacent molecules appear to be connected by hydrogen-bonds in an alternating arrangement of centrosymmetric and macrocyclic dimers. The unit cell, composed of two TMA molecules, is represented by a parallelogram with a = (1.47 ± 0.05) nm, b = (1.22 ± 0.20) nm and $\alpha = (57 \pm 5)^o$. The corresponding coverage and area per molecule are estimated to be $\Gamma_{mII} = (2.2 \pm 0.2)$ 10^{-10} mol cm^{-2} and $A_{II} = (0.75 \pm 0.05)$ nm^2. At more positive electrode potentials, in region III_b, STM experiments revealed a close-packed, striped structure with a suggested unit cell of a = (1.15 ± 0.05) nm, b = (0.95 ± 0.06) nm, $\alpha = (80 \pm 5)^o$, $\Gamma_{mIIIb} = (3.1 \pm 0.2)$ 10^{-10} mol cm^{-2} and $A_{IIIb} = (0.54 \pm 0.05)$ nm^2. This tentative assignment is based only on the assumption that TMA molecules are perpendicularly adsorbed on the positively charged electrodes, similar to the behaviors reported for other aromatic carboxylic acids [43,108,109, 110,113,114]. A comprehensive structure analysis of the interfacial adlayer will be given in the following section.

For internal calibration, the voltammetric profiles of TMA on the Au(111-25 nm) film electrodes are compared with the corresponding responses obtained from a series of stepped gold single crystals Au[n(111)-110]. Fig. 5-2 shows that, with higher step density, the characteristic phase transition peaks decrease in magnitude, broaden, and finally merge into each other. These trends indicate the increasing disorder within the TMA adlayer. The CV of an electrochemically annealed Au(111-25 nm) film electrode (shaded panel in Fig. 5-2) exhibits all the characteristic potential-dependent features of a Au(111)-oriented surface, except that the current peaks are broader than those on an ideally smooth single crystalline electrode. The comparison demonstrates that the response of a carefully prepared Au(111-25 nm) film electrode is comparable to that of a stepped Au(111) electrode with an equivalent miscut angle between 2º and 4º. Therefore, the film electrodes employed in the present ATR-SEIRAS study represent a rather good approximation to an ideal Au(111) single crystal electrode. Similar conclusions were also reported in our previous studies for sulfate [35] (see Chapter 4) and uracil on Au(111-20 nm) in aqueous electrolytes [116].

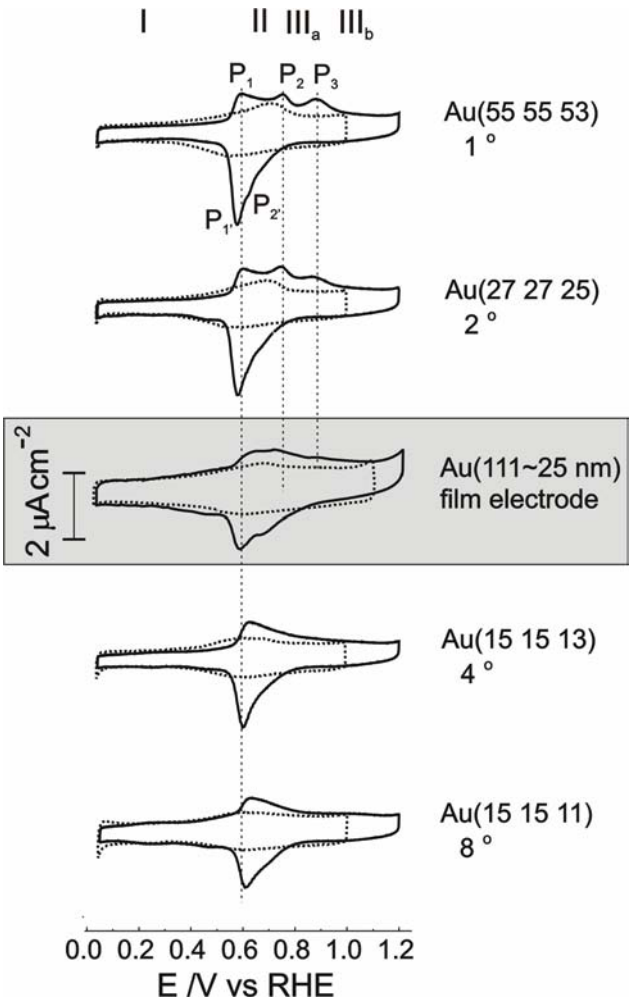

Fig. 5-2: Steady-state CVs of a series of stepped single crystals Au(n n n-1) = Au[n(111)-(110)] in 0.1 M $HClO_4$ without (dashed lines) and with (solid lines) 3 mM TMA, scan rate 10 mV s^{-1}. The miscut angles are indicated in the figure. The shaded frame shows the corresponding CVs of a Au(111-25 nm) film electrode for comparison.

5.2.1.2 SEIRAS

5.2.1.2.1 Overview and assignments

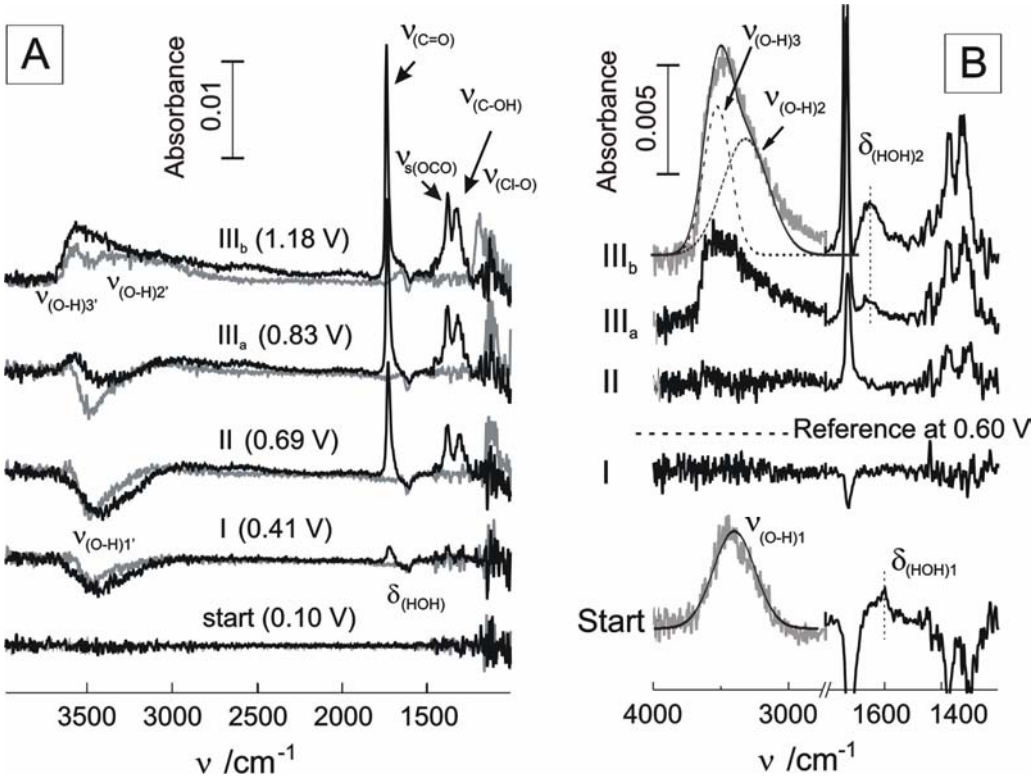

Fig. 5-3: (A) Selected SEIRA spectra of Au(111-25 nm)/0.1 M $HClO_4$ in the absence (gray traces) and in the presence of 3 mM TMA (black traces) recorded simultaneously during a positive-going potential sweep from 0.10 to 1.20 V, scan rate 10 mV s^{-1}. The background spectra were measured at 0.10 V. The data represent different potential regions of the various phases of TMA adlayer: Start (0.10 V), I (0.41 V), II (0.69 V), III_a (0.83 V) and III_b (1.18 V). (B) selected SEIRA spectra of the characteristic potential regions, I, II, III_a and III_b in 4000 to 2750 cm^{-1} and 1800 to 1200 cm^{-1} with the reference voltage chosen at E = 0.60 V. A typical result of the deconvolution of the OH-stretching region is illustrated in the top of panel B.

Fig. 5-3 shows selected slow-scan SEIRA spectra of 3 mM TMA in 0.1 M $HClO_4$ acquired simultaneously with the potentiodynamic CV (scan rate 10 mV s^{-1}). The corresponding data of the TMA-free supporting electrolyte are also plotted as gray traces. Each set of spectra represents one of the characteristic adlayer phases (I, II, III_a and III_b) acquired during a positive potential scan. A set of single beam spectra recorded at E = 0.10 V was chosen as reference. For reasons of clarity, the continuous evolution of the 3D spectral features during a complete potential cycle is separately shown in Fig. 5-4 for the two intervals $1200 < \nu < 1800$ cm^{-1} and $2750 < \nu < 4000$ cm^{-}

[1]. The spectra in the OH-stretching region are plotted choosing either E = 0.10 V (Fig. 5-4B) or E = 0.60 V (Fig. 5-4C) as reference.

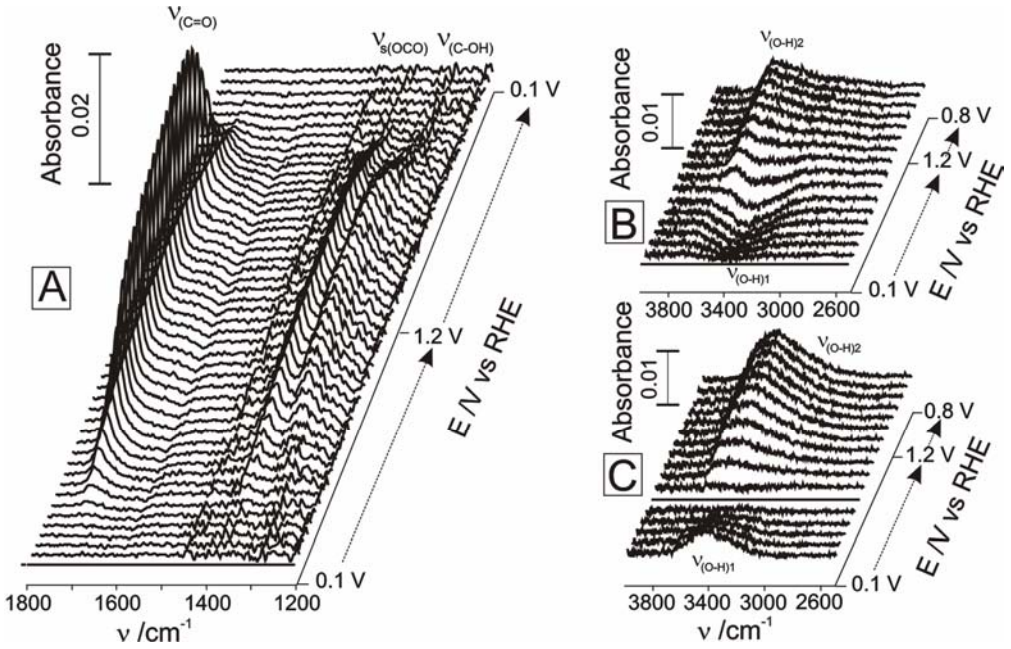

Fig. 5-4: Typical set of 3D SEIRA spectra measured simultaneously with a slow-scan voltammogram (10 mV s^{-1}) during a potential cycle from 0.10 V to 1.20 V and back to 0.10 V. Each spectrum represents the average of 160 single traces within a potential interval of 50 mV. (A) shows the wavenumber region 1800 ~ 1200 cm^{-1} with a single beam spectrum taken at 0.10 V as the reference. (B) and (C) represent the $\nu_{(O-H)}$ region 4000 ~ 2750 cm^{-1} choosing the reference spectrum at E = 0.10 V (B) and E = 0.60 V (C), respectively. For reasons of clarity, the spectra in panels B and C do not show the complete sets of data for the negative-going potential sweeps.

As the potential increases from 0.10 V to more positive values, three sharp positive-going infrared bands appear in the presence of 3 mM TMA at 1720 ~ 1735 cm^{-1}, around 1375 cm^{-1}, and at 1300 ~ 1320 cm^{-1} (black traces in Fig. 5-3A). Comparison with the spectra of BA, IA and TMA in solid state and solution, as well as with their potassium salts supports the assignment of these spectral features to the following TMA vibrations: the stretching mode of C=O in COOH ($\nu_{(C=O)}$), the symmetric stretching mode of O-C-O in COO^- ($\nu_{s(OCO)}$), e.g. a carboxylate group, and the stretching mode of C-OH in COOH ($\nu_{(C-OH)}$), respectively [117 , 118]. A correlation analysis suggests that all sets of vibration modes originate from the same molecule. The intensities of these TMA bands increase with positive potential sweep, reach their maximum in the chemisorbed region III, and decrease during the subsequent negative potential scan.

Simultaneously, broad IR bands appear between 3000 cm^{-1} and 3600 cm^{-1} corresponding to O-H stretching vibrations ($\nu_{(O-H)}$) of interfacial water molecules [13,119,120]. The potential dependent evolutions of the O-H stretching modes, $\nu_{(O-H)}$, and of the HOH bending mode, $\delta_{(HOH)}$, are plotted in Fig. 5-3 and Fig. 5-4. The reference spectrum was either recorded at E = 0.10 V (the most negative potential) or at E = 0.60 V (close to the potential of zero charge for the present system). Qualitatively, the spectra in Fig. 5-3A and Fig. 5-4B illustrate that the intensity of a broad negative-going band centered around 3410 cm^{-1}, which starts to grow in phase I, reaches its maximum at 0.65 V. This band is labeled as $\nu_{(O-H)1}$, and corresponds to the replacement of weakly hydrogen-bonded interfacial water by physisorbed TMA molecules [116,119]. At more positive potentials, a new positive-going water stretching mode $\nu_{(O-H)2}$ starts to evolve at around 3500 cm^{-1}. This vibration is attributed to the water species co-adsorbed with the chemisorbed TMA adlayer. Detailed assignments of $\nu_{(O-H)}$ bands will be given in Section 5.2.1.2.3.3.

The SEIRA spectra of the supporting electrolyte (0.1 M $HClO_4$, gray traces in Fig. 5-3A) show the existence of weakly hydrogen-bonded water at E < 0.60 V, strongly hydrogen-bonded interfacial water at E > 0.60 V, and isolated water at E > 0.8 V. Detailed assignment has been given in Chapter 4.

5.2.1.2.2 Local structure of chemisorbed TMA

Both calculations and experimental evidence support that a deprotonated $-COO^-$ group has a strong preference to occupy a bridge site via chemical bonds including two oxygen atoms bound to two neighboring metal atoms, with the carbon atom in between [121, 122, 123] as shown in Fig. 5-5. At sufficient positive potentials, perpendicularly oriented TMA molecules could be chemisorbed onto the electrode surface via one or two carboxylate groups [105,107,124].

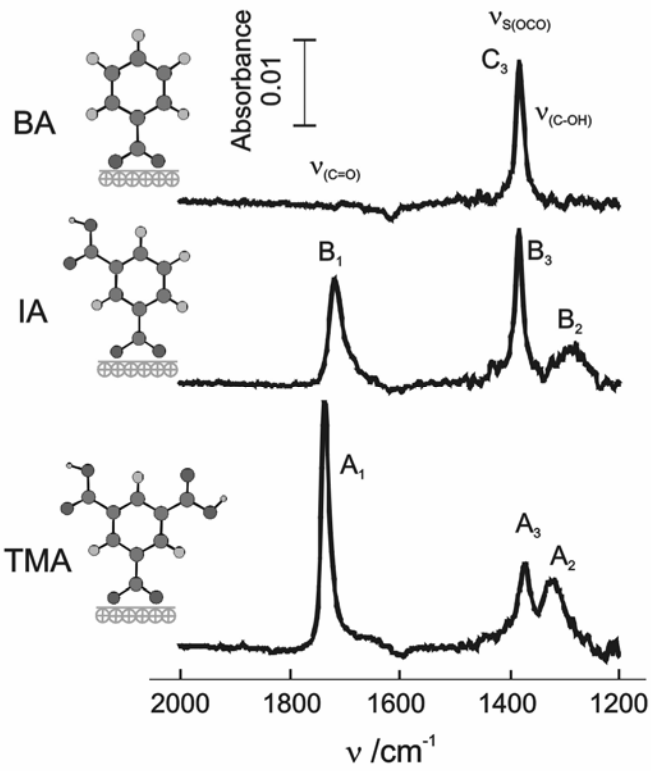

Fig. 5-5: Equilibrium SEIRA spectra of TMA (3 mM), IA (saturated solution ~ 0.5 mM) and BA (3 mM) in 0.1 M $HClO_4$ obtained at 1.10 V in region III_b, reference spectrum taken at E = 0.10 V. The insets illustrate the derived molecular orientations of the three molecules chemisorbed on a positively charged Au(111-25 nm) film electrode.

In order to resolve the issue on surface coordination, we carried out a comparative study of BA, IA and TMA in the high coverage region III. These carboxylic acids have different numbers of identical carboxyl groups but similar conjugated structures (Detailed results will be discussed in Section 5.3). Fig. 5-5 shows SEIRA spectra of the three molecules at E = 1.1 V, as recorded during a slow potential scan experiment. The symmetric mode $\nu_{s(OCO)}$, 1370 ~ 1390 cm^{-1}, (FWHM ~ 2 cm^{-1}) appears in all three spectra (labeled as A_3, B_3 and C_3), indicating that these three acids are coordinated to the positively charged electrode by at least one carboxylate group. The spectrum of IA shows the $\nu_{s(OCO)}$ mode (B_3) and two additional vibrations, $\nu_{(C=O)}$ at 1715 cm^{-1} (B_1) and $\nu_{(C-OH)}$ at 1290 cm^{-1} (B_2), which originate from a protonated -COOH group. This signature indicates that IA is coordinated to the electrode surface with one carboxylate group, while the other (protonated) carboxyl group faces the electrolyte.

One may assume that the position and the surface coordination of carboxylate and carboxyl groups should be constant after the adsorption equilibrium has been established. Therefore, we conclude from the approximately identical ratio of the integrated intensities $I_{B1}/I_{B2} \approx I_{A1}/I_{A2} \approx 1.40$ that the chemisorbed adlayers of IA and TMA exhibit structure similarities. With I_{A3} and I_{B3} as an internal standard one obtains $I_{A1}/I_{A3} \approx 2 \times I_{B1}/I_{B3}$ indicating that the TMA adlayer exhibits two protonated -COOH groups while IA has only one. These quantitative estimations imply that both IA and TMA are coordinated via one carboxylate group to the positively charged electrode in the chemisorbed phase.

5.2.1.2.3 Substrate/adsorbate and hydrogen-bonding interaction

The slow-scan SEIRA spectra plotted in Fig. 5-4 indicate that the adsorption and surface orientation of TMA are potential dependent, and major changes occur upon the transition from physisorption to chemisorption. Based on the surface selection rule of SEIRAS, only those molecular vibrations that induce dipole moments normal to the local surface give enhanced IR absorption [40,112]. No vibration modes related to TMA adsorption were observed at E < 0.35 V. The absence of the characteristic TMA bands $\nu_{(C=O)}$ and $\nu_{(C\text{-}OH)}$, which induce dipole moments parallel to the plane of the phenyl ring, indicates that TMA molecules are oriented with the phenyl ring parallel to the electrode surface. Locally, the organic molecules appear to change their orientation at E > 0.35 V.

To describe the structure transition in detail, we plotted in Fig. 5-6 the potential dependence of intensities, peak positions and full widths at half maximum (FWHM). Because TMA molecules are chemisorbed to the substrate surface by carboxylate groups, and connected to each other laterally via hydrogen-bonded carboxyl groups, the evolution of those vibration parameters of $\nu_{(C=O)}/\nu_{(C\text{-}OH)}$ and $\nu_{s(OCO)}$ contains characteristics of intermolecular hydrogen-bonding and substrate/adsorbate interactions.

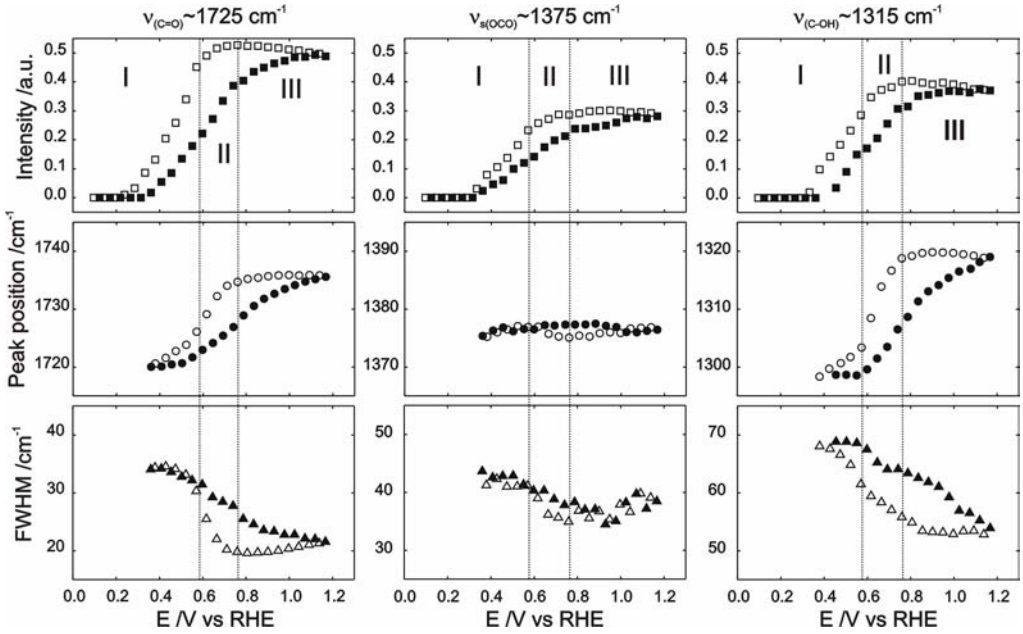

Fig. 5-6: Potential dependencies of the integrated intensities (■, □), the peak positions (●, ○) and the FWHM (▲, Δ) of the $\nu_{(C=O)}$ (~ 1725 cm^{-1}), $\nu_{s(OCO)}$ (~ 1375 cm^{-1}) and $\nu_{(C-OH)}$ (~ 1315 cm^{-1}) bands as obtained from the data plotted in Fig. 5-3 and 5-4. The solid (open) symbols represent the positive (negative) going potential scan.

5.2.1.2.3.1 Intermolecular hydrogen-bonding

The intensities of $\nu_{(C=O)}$ and $\nu_{(C-OH)}$ are directly influenced by the TMA orientation and the number of uncoordinated -COOH side groups. The rapid intensity increase upon changing the potential from region I to region II indicates the onset of an orientation change from planar to tilted or perpendicular. The intensities of $\nu_{(C=O)}$ and $\nu_{(C-OH)}$ increase only moderately in region III_a and reach a plateau in region III_b indicating the formation of a stable chemisorbed adlayer III_b. Reversing the direction of the potential scan exhibits a distinct hysteresis in 1.00 V > E > 0.40 V, which suggests a rather slow structure transition in this potential range. We notice further that in situ STM experiments of TMA on ideally smooth Au(111) single crystal electrodes show long range ordered physisorbed adlayers of hydrogen-bonded and still planar oriented molecules in region II (e.g. up to E ~ 0.80 V). The more negative onset of the structure transition of TMA on the Au(111-25 nm) film electrodes is most probably related to the surface morphology of the gold film. The latter is composed of islands with a preferential (111) surface orientation, which have inherently a higher defect density and larger grain boundaries than an ideal Au(111) single crystal surface [13]. In consequence, the TMA adlayer appears to be more disordered in the

physisorbed regions I and II, and the uneven potential distribution near defect sites might facilitate localized orientation changes at more negative potentials, as observed in the in situ ATR-SEIRA spectra.

Both bands, $\nu_{(C=O)}$ and $\nu_{(C\text{-}OH)}$, shift to higher wavenumbers with increasing electrode potential. A plateau is reached after establishing an equilibrated chemisorbed phase in region III, the most pronounced change occurs in region II. This evolution is reversible, but shows a distinct hysteresis. Potential-dependent peak shifts of vibration modes may be attributed to three different factors: the Stark tuning effect, metal/adsorbate electron (back) donation, and lateral interactions such as dipole-dipole coupling [118,119]. There is no strong experimental evidence for a predominant Stark tuning effect because the potential-dependent peak shifts are not as linear as expected [116,125], and the electric field around the -COOH side groups is rather weak. Peak shifts preferentially attributed to strong dipole-dipole coupling have been suggested for the adsorption of several organic molecules capable of forming close-packed adlayers, such as cytosine [115], 4,4′-bipyridine [13], BA [108,109] and uracil [116]. For the present system the ladder-type network of chemisorbed TMA appears to be still too open to support strong interactions between the oscillating dipoles of adjacent -COOH groups. Although a direct substrate/-COOH side group electron donation can be ruled out, an indirect ET via the π–electron system of TMA appears to be possible. The molecule represents a perfectly conjugated system. In consequence, changes in the electron (charge) density in one -COOH group can be partially “transferred” to the other two -COOH or $-COO^-$ groups, respectively. An electron back donation to the coordinating carboxylate group at positive potential may generate a simultaneous electron donation to both -COOH side groups, which results in a shift of $\nu_{(C=O)}$ and $\nu_{(C\text{-}OH)}$ to higher wavenumbers. A similar blue shift of the $\nu_{(C=O)}$ and $\nu_{(C\text{-}OH)}$ bands is observed in the potential-dependent SEIRA spectra of IA. An additional contribution to the observed blue shift in phase III could be induced due to directional hydrogen-bonds between the -COOH side groups, which should increase the stretching constant of the in-phase $\nu_{(C=O)}$ and $\nu_{(C\text{-}OH)}$ vibrations. Table 5-1 compares the peak shifts $\Delta\nu$ for the characteristic vibrations of BA, IA and TMA. The smaller values of $\Delta\nu$ of the $\nu_{(C=O)}$ and $\nu_{(C\text{-}OH)}$ vibrations of IA could be attributed to the weaker hydrogen-bonding interactions compared to TMA.

Simultaneously, the FWHM of $\nu_{(C=O)}$ and $\nu_{(C\text{-}OH)}$ decreases from phase I to III_b, and reaches a minimum in the potential region III. This trend suggests an increasing long-range lateral order with the establishment of the chemisorbed phase III_b. In combination with an in situ STM, the present SEIRAS result demonstrates that TMA molecules form a highly ordered 2D ladder network. The molecules are coordinated via one -COO^- group to the electrode surface, while the two remaining -COOH side groups give rise to rows of hydrogen-bonded dimers.

5.2.1.2.3.2 Substrate/adsorbate interaction

The three carboxyl groups of TMA are protonated in 0.1 M $HClO_4$ (pH = 1 and for TMA pK_a = 2.12, 4.10 and 5.18 [126]). The $\nu_{s(OCO)}$ vibration appears only when TMA molecules are chemisorbed onto the surface via carboxylate groups. Similar $\nu_{s(OCO)}$ vibrational bands were observed for chemisorbed BA [108,109,110,111], fumaric acid [113], fluorobenzoic acid [43] and *p*-nitrobenzoic acid [114] on various gold electrodes.

Table 5-1: Potential induced peak shifts of the characteristic COO(H)-vibrational modes of different carboxylic acids. ($\Delta\nu$ values were calculated from the subtraction of spectra at 0.64 V and 1.18 V.)

	$\Delta\nu_{s(OCO)}$ /cm^{-1}	$\Delta\nu_{(C=O)}$ /cm^{-1}	$\Delta\nu_{(C\text{-}OH)}$ /cm^{-1}	Γ_m /10^{-10} mol cm^{-2}
BA [108,109,121]	15~20	-	-	7.3
IA	8	11	14	6.1
TMA	~ 0	15	20	3.3
Fumaric acid [113]	16	~ 0	~ 0	4.0

As illustrated in Fig. 5-6, the plot of the intensity of $\nu_{s(OCO)}$ shows a similar potential dependence as $\nu_{(C=O)}$ and $\nu_{(C\text{-}OH)}$: it grows slowly with increasing potential in phase I, and reaches a constant value in phase III_b. The increase of intensity in region II suggests deprotonation and a change in molecular orientation. Similar trends were observed for BA on Au(111) [108,109].

The frequency of the $\nu_{s(OCO)}$ band is almost potential independent. We notice that $\nu_{s(OCO)}$ shows a strong potential dependence and a characteristic blue shift with

$\Delta\nu$ up to 16 cm^{-1} for densely packed adlayers of carboxylic acids such as BA [108,109] and fumaric acid [113]. This observation is attributed to strong dipole-dipole coupling at high surface coverage. STM experiments (Fig. 5-1D) [45] reveal that the packing of TMA in the chemisorbed phase III appears to be less compact, leading to rather large distances between the neighboring carboxylate groups. Table 5-1 illustrates the values of $\Delta\nu$. The following sequence is obtained: fumaric acid > BA > IA > TMA. One also needs to consider a strong adsorbate/substrate interaction between the surface coordinated carboxylate groups and the positively charged gold electrode, which should result in a red shift of $\nu_{s(OCO)}$. However, this trend seems to be compensated by a Stark shift.

5.2.1.2.3.3 Co-adsorbed H_2O

The high sensitivity of ATR-SEIRAS enables us to monitor structure properties of electrolyte species in the electrochemical double layer associated with the adsorption of TMA [13,116,119,120]. Fig. 5-3 and 5-4 B, C show the potential-dependencies of the vibrational characteristic of interfacial water species.

As discussed before, the overlapped positive-going and negative-going $\nu_{(O-H)}$ modes complicate the analysis. In order to deconvolute the contributions of different interfacial water species, we adapt a strategy proposed in ref. [119] and have chosen the spectrum at E = 0.60 V, which is close to the potential of zero charge for the present system, as the new reference spectrum. The recalculated spectra are plotted in Fig. 5-3B and Fig. 5-4C. At E < 0.60 V a broad band, $\nu_{(O-H)1}$, centered at 3410 cm^{-1} and a weak band $\delta_{(HOH)1}$ at 1600 cm^{-1} are observed. The shape of the $\nu_{(O-H)1}$ band is rather symmetric, suggesting the preference of only one type of water species. At more positive potentials, in regions II and III, an asymmetric band with a distinct shoulder at higher wavenumber evolves. The deconvolution allows the identification of two contributions: one broad band, $\nu_{(O-H)2}$ centered at 3320 cm^{-1}, and a sharper band, $\nu_{(O-H)3}$ around 3520 cm^{-1} (Fig. 5-3B). The $\nu_{(O-H)2}$ mode and a weak $\delta_{(HOH)2}$ mode (~ 1650 cm^{-1}) indicate the existence of strongly hydrogen-bonded water species in phase III_b.

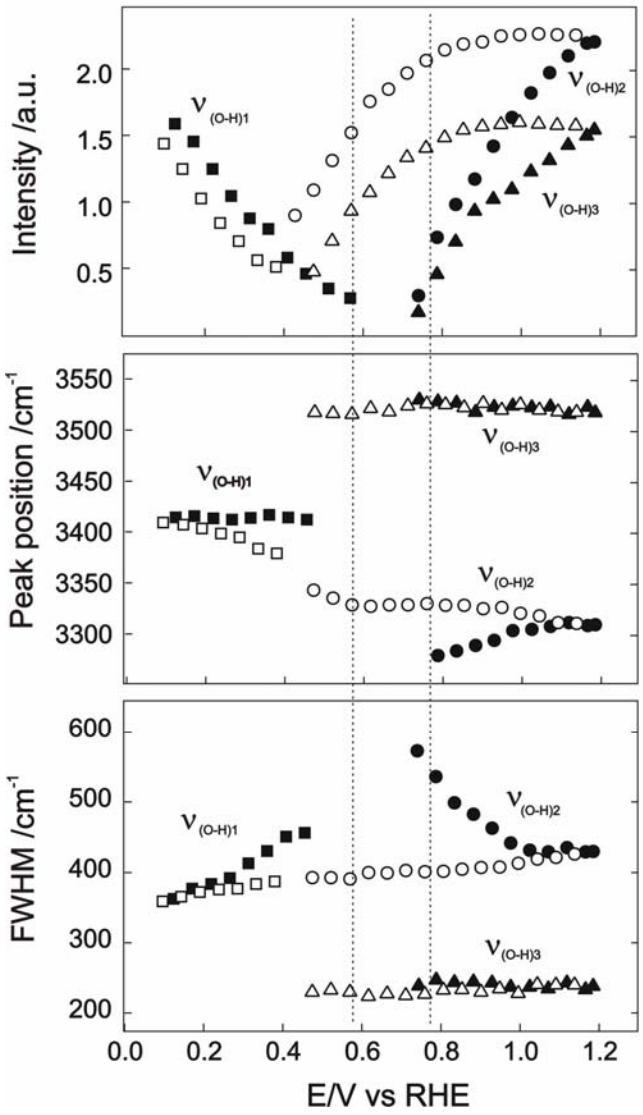

Fig. 5-7: Potential dependencies of the integrated intensities, the peak positions and the FWHM of the $\nu_{(O-H)}$ modes for 3 mM TMA/0.1 M $HClO_4$ on Au(111-25 nm) film electrodes: $\nu_{(O-H)1}$ (■,□), $\nu_{(O-H)2}$ (●,○) and $\nu_{(O-H)3}$ (▲, Δ) as obtained from the data plotted in Fig. 5-3 and 5-4. The solid (open) symbols represent the positive (negative) going potential scan.

Based on the above analysis, at least three different co-adsorbed water species appear during a slow scan from negative to positive potentials accompanied with the formation of the various TMA adlayers. Fig. 5-7 shows the potential-dependence of peak intensity, peak position and FWHM of the $\nu_{(O-H)1}$, $\nu_{(O-H)2}$, and $\nu_{(O-H)3}$ modes. $\nu_{(O-H)1}$ corresponds to weakly hydrogen-bonded water species which are adsorbed on the negatively charged surface in the absence of TMA. They are subsequently replaced by physisorbed TMA molecules in phase I giving rise to a negative-going spectroscopic feature. $\nu_{(O-H)2}$ and $\nu_{(O-H)3}$ start to grow in phase III_a simultaneously the formation of a chemisorbed TMA adlayer, indicating that interfacial water is co-adsorbed within or next to the TMA adlayer. Their intensities increase until a maximum is reached in the potential regions of an equilibrium phase III_b, and subsequently decrease upon the onset of TMA desorption. Weakly hydrogen-bonded water appears again as indicated by an increase of the intensity of $\nu_{(O-H)1}$ in phase I at negative charge densities.

Additional knowledge can be obtained from the potential-dependence of the respective peak positions. The vibration mode of strongly hydrogen-bonded water, $\nu_{(O\text{-}H)2}$, appears in region III_a and shifts to higher wavenumber ($\Delta\nu \approx 50$ cm^{-1}) with increasing potential. Such water molecules could be hydrogen-bonded to the oxygen atoms of the -COOH side groups of TMA, which are directed toward the electrolyte. The small blue shift shows that the hydrogen-bonding interaction between interfacial water and the -COOH groups is weakened upon the formation of the long-range ordered ladder network between adjacent TMA molecules in III_b. Simultaneously, the FWHM of $\nu_{(O\text{-}H)2}$ decreases in phase III_a, and reaches a minimum in phase III_b.

Compared to $\nu_{(O\text{-}H)2}$, $\nu_{(O\text{-}H)3}$ is less synchronized with the formation - dissolution of the chemisorbed TMA adlayer. Its peak position and FWHM are almost potential-independent. The integrated intensity of $\nu_{(O\text{-}H)3}$ increases towards phase III_b. The high wavenumbers and narrow bands suggest to attribute $\nu_{(O\text{-}H)3}$ to weakly hydrogen-bonded or isolated water species next to the chemisorbed TMA adlayer and/or at defect sites not being in direct contact with the electrode surface. The location of these water species appears to be different from those discussed for blank supporting electrolytes such as $HClO_4$ [119], where a direct contact to the electrode surface is proposed.

5.2.1.3 Steady-state models

Fig. 5-8 summarizes schematically the potential-dependent evolution of the TMA adlayer structures on Au(111-25 nm) film electrodes in contact with 0.1 M $HClO_4$ aqueous electrolyte.

At 0.10 V (starting potential), TMA molecules are randomly adsorbed in a planar orientation together with weakly hydrogen-bonded interfacial water molecules. In phase I ($0.10 < E < 0.50$ V) planar oriented TMA molecules form a 2D ordered physisorbed adlayer. Weakly hydrogen-bonded water species are replaced by the organic molecules. At higher potentials, in phase II ($0.58 < E < 0.75$ V), a close-packed physisorbed adlayer composed of linear dimers forms slowly. Further increase of the electrode potential to phase III_a ($0.75 < E < 0.88$ V) causes a orientation change from planar to perpendicular. Each TMA molecule is chemisorbed via one carboxylate group leaving the two -COOH side-groups available for further hydrogen-

bonding between neighboring TMA molecules. In parallel, two types of water species start to be co-adsorbed: weakly hydrogen-bonded water at intermolecular defect sites and strongly hydrogen-bonded water interacting with -COOH side-groups. In phase III_a, the initially chemisorbed TMA molecules are still mobile and disordered. At E > 0.90 V, in region III_b, almost all surface coordinated TMA molecules are interconnected via intermolecular hydrogen-bonds between adjacent -COOH side-groups, resulting in a stable and highly ordered ladder network.

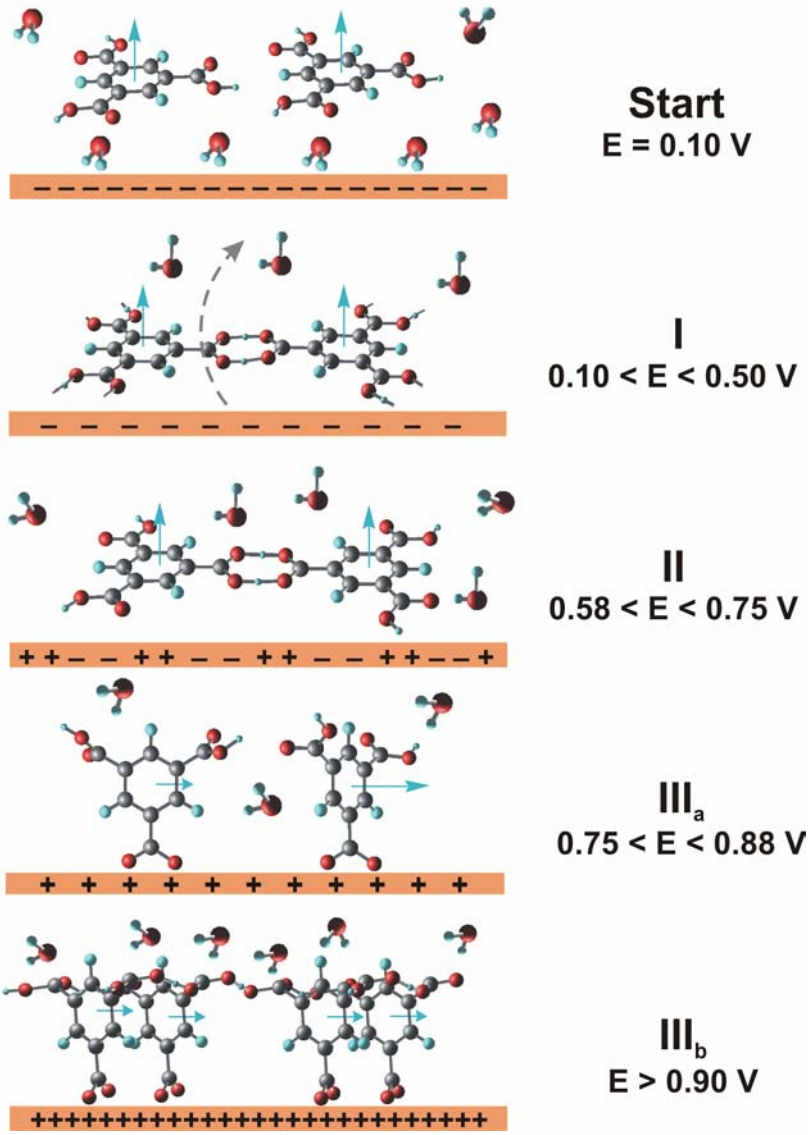

Fig. 5-8: Models of steady-state TMA adlayer structures in the potential regions I, II, III_a and III_b.

5.2.2 2D phase formation kinetics

After the discussion of the potential-dependent steady-state TMA adlayer structures, further discussion will focus on the kinetics of structure transitions between the different adlayer phases. Advanced spectroscopic acquisition modes, such as rapid-scan and step-scan, enable us to study potential-induced structure changes with high time resolution. Potential steps from the physisorbed phase I into the chemisorbed phase III_b were applied to monitor the formation kinetics of the chemisorbed TMA adlayer. The corresponding current transients are recorded simultaneously. We have chosen the following regime: E_i = 0.45 V (10 s) → E_f = 0.90 V for rapid-scan experiments and E_i = 0.45 (250 ms) → E_f = 0.90 V for the step-scan studies. The reference spectrum was measured at each starting potential before stepping the potential.

5.2.2.1 Long time scale: rapid scan

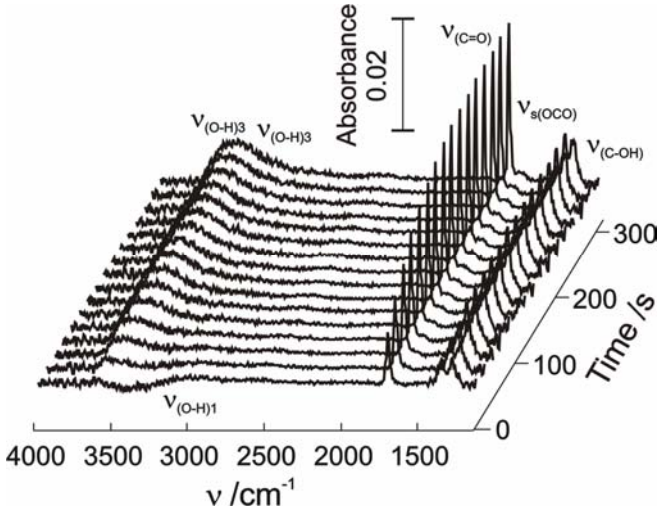

Fig. 5-9: Time-resolved SEIRA spectra for the formation of a chemisorbed TMA adlayer III_b on Au(111-25 nm)/0.1 M $HClO_4$ + 3 mM TMA, recorded in the rapid-scan regime after a single potential step from E_i = 0.45 V to E_f = 0.90 V. The waiting time at E_i was 10 s. Each spectrum plotted was averaged in an interval of 9.7 s and represents the average of 256 individual traces.

Fig. 5-9 shows selected SEIRAS spectra recorded in rapid-scan mode for a single potential step from E_i = 0.45 V (10 s) to E_f = 0.90 V. The three characteristic bands of chemisorbed TMA start to grow immediately after the potential step, indicating an orientation change from planar to perpendicular within t << 10 s. Subsequently, these bands become gradually stronger and sharper until a maximum is

reached, suggesting a rather slow increase of surface coverage and 2D long-range order in region III_b. The time-dependencies of intensity, peak position and FWHM are plotted in Fig. 5-10. The evolution of the simultaneously co-adsorbed water species is shown in Fig. 5-11.

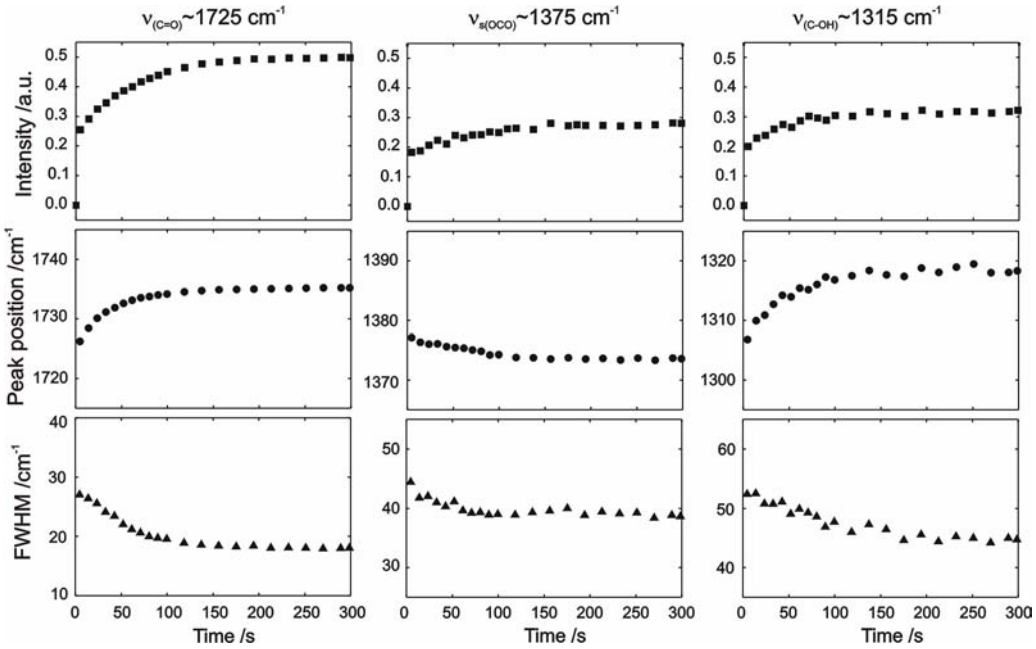

Fig. 5-10: Time dependencies of the integrated intensities (■), the peak positions (●) and the FWHM (▲) of the $\nu_{(C=O)}$ (~ 1725 cm^{-1}), $\nu_{s(OCO)}$ (~ 1375 cm^{-1}) and $\nu_{(C-OH)}$ (~ 1315 cm^{-1}) bands of TMA as obtained from the data plotted in Fig. 5-9.

The intensities of $\nu_{(C=O)}$, $\nu_{s(OCO)}$ and $\nu_{(C-OH)}$ indicate that a final steady state is reached approximately 150 s after triggering the potential step. The lateral alignment of TMA to establish the long-range ordered, hydrogen-bonded network is rather slow, which is consistent with the result of our recent in situ STM measurements [45]. Further insight into the kinetics of ordering can be provided by the analysis of the time dependencies of the FWHM and the peak positions of the TMA modes, as well as of the vibration features of co-adsorbed water.

The FWHM values of $\nu_{(C=O)}$, $\nu_{s(OCO)}$ and $\nu_{(C-OH)}$ decrease with time and reach a steady state after 150 s, indicating the formation of a long-range ordered adlayer (Fig. 5-10). The simultaneously recorded time dependencies of the peak positions of $\nu_{(C=O)}$ and $\nu_{(C-OH)}$ exhibit a slow shift to higher wavenumbers ($\Delta\nu \sim 10$ cm^{-1}). This is partially due to the increased lateral interactions as a result of directional hydrogen-bonds formed between neighboring TMA molecules. The electron donation may also

contribute to the blue shift, which represents an increase of substrate/adsorbate interactions upon the formation of a long-range ordered adlayer at the positively charged electrode surface.

Compared with the blue shift of $\nu_{(C=O)}$ and $\nu_{(C\text{-}OH)}$, the $\nu_{s(OCO)}$ band shifts to lower wavenumbers ($\Delta\nu \approx 5$ cm^{-1}), reaching a constant position at 1380 cm^{-1}. As described in Section 5.2.1, $\nu_{s(OCO)}$ is related to -COO$^-$ groups coordinated in a perpendicular position to the positively charged electrode surface. The red shift of the $\nu_{s(OCO)}$ band can be attributed to the increase of electron back-donation when the substrate/adsorbate interaction increases with surface order.

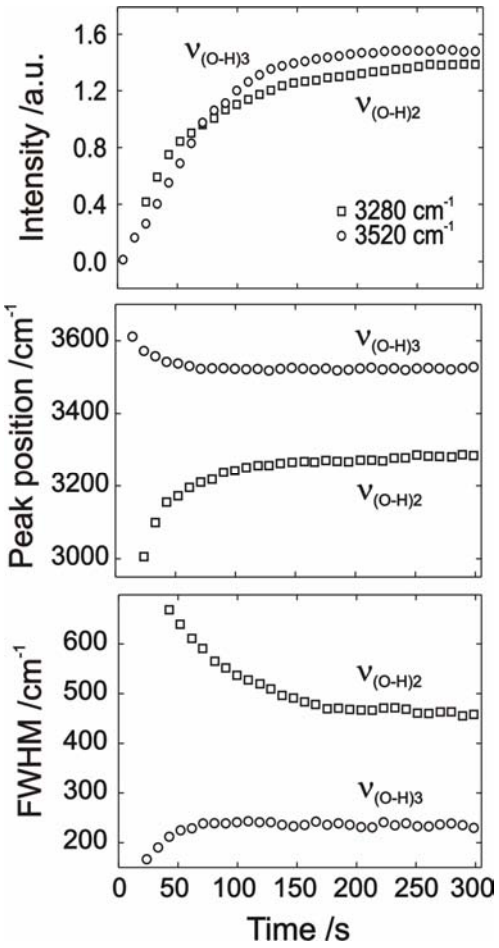

Fig. 5-11: Time dependencies of the integrated intensities, the peak positions and the FWHM of the OH-stretching modes $\nu_{(O\text{-}H)2}$ (□) and $\nu_{(O\text{-}H)3}$ (○) of co-adsorbed water species as obtained from the rapid-scan spectra plotted in Fig. 5-9 after deconvolution.

The appearance of the negative-going band $\nu_{(O\text{-}H)1}$, immediately after application of the potential step (<< 5 s, Fig. 5-9), represents the displacement of weakly hydrogen-bonded water molecules from the electrode surface by additional adsorbed TMA. Its intensity is small because the experiment starts at a rather positive potential with a significant amount of TMA physisorbed in a planar orientation. The intensities of $\nu_{(O\text{-}H)2}$ and $\nu_{(O\text{-}H)3}$ increase simultaneously with the evolution of the

characteristic bands for perpendicularly adsorbed TMA (Fig. 5-10) indicating co-adsorption with the organic molecules in phase III_b. Interestingly, the peak position and FWHM of the $\nu_{(O\text{-}H)3}$ band reach steady-state values somewhat faster (~ 100 s) than the $\nu_{(O\text{-}H)2}$ band (~ 150 s). Such a delay between $\nu_{(O\text{-}H)2}$ and $\nu_{(O\text{-}H)3}$ shows that the isolated water species are co-adsorbed with the TMA molecules before the ordered equilibrated TMA adlayer is formed, while the strongly hydrogen-bonded water phase forms simultaneously with the ordered TMA adlayer.

5.2.2.2 Short time scale: step scan

To explore the kinetics of the structure transition within the TMA adlayer at a very short time after stepping the potential, we carried out simultaneous electrochemical and spectroscopic step-scan experiments. This regime enables us to increase the time resolution with our current setup up to 10^{-5} s. Fig. 5-12A shows a 3D plot for the evolution of the TMA marker band $\nu_{(C=O)}$ after application of a single potential step from E_i = 0.45 V to E_f = 0.90 V. The time dependence of the integrated intensity of the $\nu_{(C=O)}$ TMA band, as calculated from time slices of 0.2 ms, is plotted in Fig. 5-12B. A similar time-dependence was observed for $\nu_{s(OCO)}$ and $\nu_{(C\text{-}OH)}$. For reasons of clarity, one typical spectrum recorded after 8 ms in $1200 < \nu < 1800$ cm^{-1} is plotted as inset of Fig. 5-12A.

The electrochemical current transient, as monitored after the potential step, is characterized by a single exponential decay (c.f. solid line in Fig. 5-12B). This macroscopic response may contain several different contributions such as double layer charging, deprotonation of -COOH groups, reorientation of the organic molecules and/or co-adsorbed water species. However, the chronoamperometric experiments do not provide direct information on structure changes within the adlayer. To address this issue, step-scan SEIRAS experiments were carried out with synchronized electrochemical measurements.

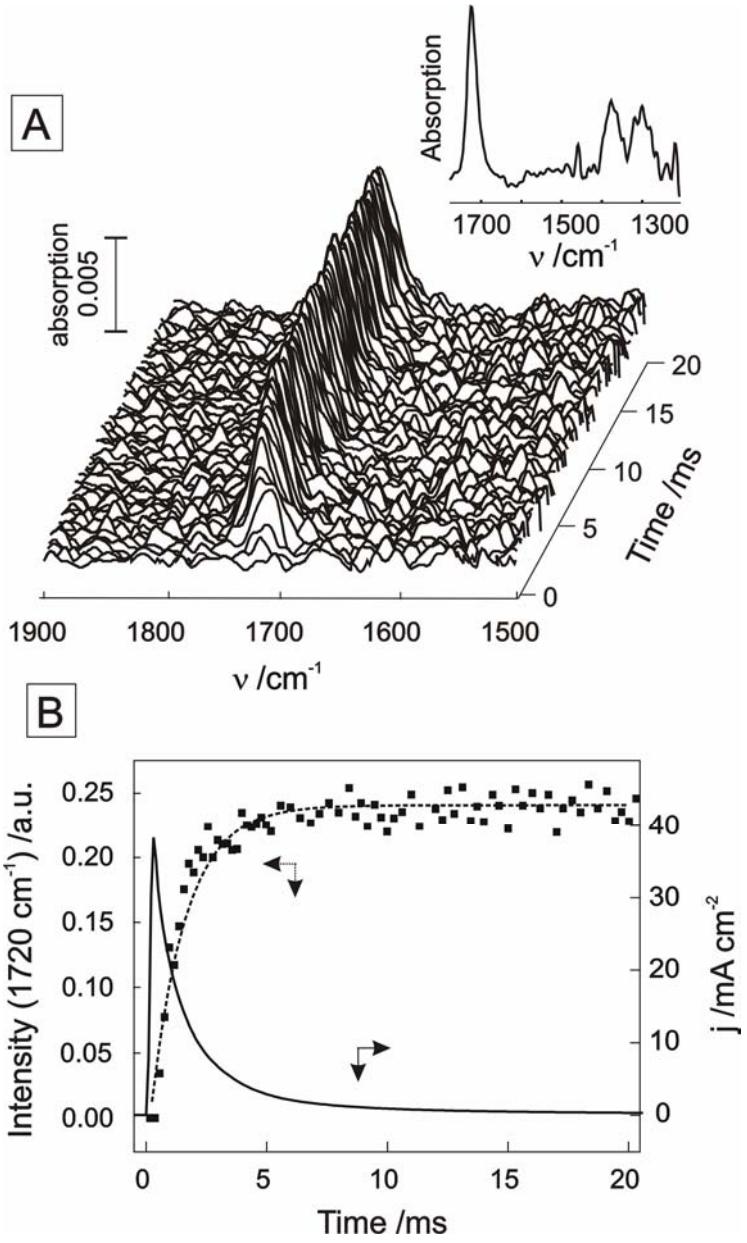

Fig. 5-12: (A) Series of time-dependent SEIRAS spectra for the formation of a chemisorbed TMA adlayer on Au(111-25 nm) in 0.1 M $HClO_4$ + 3 mM TMA after a single potential step from E_i = 0.50 V (t_w = 0.22 s) to E_f = 0.90 V as measured in the step-scan regime. The inset shows a typical extended spectrum recorded after 8 ms in 1200 < ν < 1800 cm^{-1}. (B) Time dependence of the integrated intensity of the TMA marker band $\nu_{(C=O)}$ (■) as calculated from the spectra shown in panel (A). The dashed line represents the fit of Eqs. 5.1 to the spectroelectrochemical transients with the following parameters: I_∞ = 0.237, K = 0.686 ms^{-1}, t_0 = 0 ms. The experimental time resolution is 200 μs. The simultaneously measured current transient is shown as solid line.

Fig. 5-12B demonstrates that the intensity of the $\nu_{(C=O)}$ mode increases rapidly and reaches a maximum after 8 ms, which is much longer than the time constant of

our IR cell (ca. 50 μs [13]). This result suggests a fast orientation change of TMA from planar to randomly oriented perpendicular molecules. The simultaneous evolution of $\nu_{s(OCO)}$ also indicates the deprotonation of the carboxyl group. The observed transition is significantly faster than the establishment of a 2D order within the organic adlayer observed in the rapid scan experiments. The intensity vs. time curve in Fig. 5-12B is represented by a first order Langmuir-type rate equation:

$$I = I_\infty \{1 - \exp[-K(t - t_0)]\} \tag{5.1}$$

with I_∞ as the integrated intensity at $t \rightarrow \infty$, K is the rate coefficient and t_0 an induction time (dashed line in Fig. 5-12B). The model suggests that the re-orientation of TMA molecules is initialized at randomly distributed defect sites, the initially chemisorbed TMA molecules are rather far from each other without efficient lateral hydrogen-bonding interaction. No ordered chemisorbed TMA phase is established within a short time scale of 20 ms. This "disorder" transition starts mainly from the defect sites on the electrode surface, as observed in the STM study [45]. Similar transitions were reported previously in SEIRAS kinetic studies of fumaric acid [113], which give rises to a completely disordered adlayer, and for *p*-nitrobenzoic acid on Au film electrodes [114].

5.2.2.3 Two-step kinetic models

The kinetic model of the formation of the chemisorbed phase is illustrated in Fig. 5-13. Immediately after a potential step to region III, TMA molecules change their orientation from planar to tilted or perpendicular accompanied by the deprotonation of -COOH groups. This process involves the breakdown of the hydrogen-bonded network of the physisorbed phase I and the incorporation of additional TMA molecules from the bulk electrolyte into the interfacial region. In a subsequent and much slower process the chemisorbed TMA molecules start to gradually align into a highly ordered 2D network III_b. At the same time, TMA molecules appear to be co-adsorbed with strongly hydrogen-bonded and isolated water species. Such a two-step scenario and the disorder → order evolution of chemisorbed TMA are consistent with our STM investigation [45].

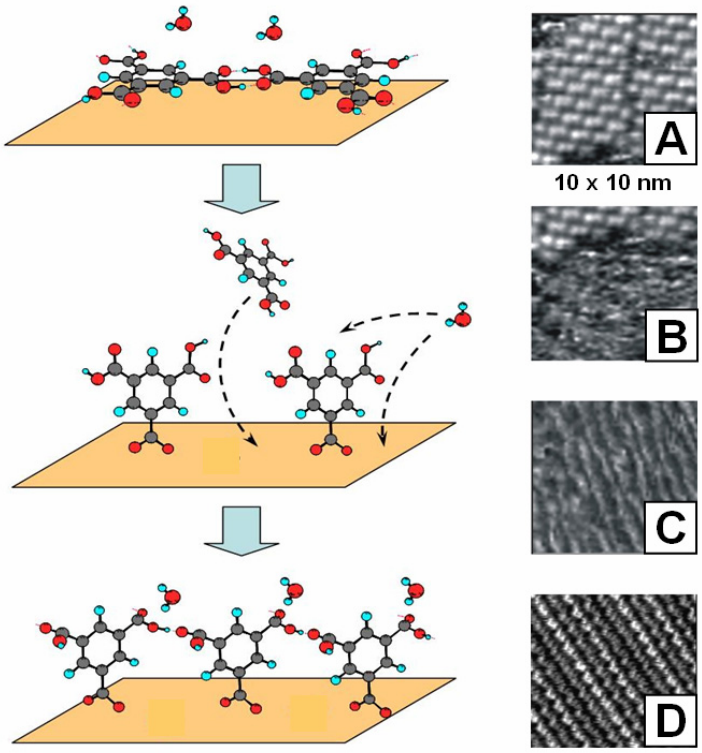

Fig. 5-13: 2-step kinetic scenario of the formation of the chemisorbed TMA adlayer. Fast process: TMA molecules change their orientation from planar to tilted or perpendicular accompanied by the deprotonation of one carboxyl group immediately after a potential step in region III; Subsequent slow process: the chemisorbed TMA molecules start to gradually align into a highly ordered 2D network III_b. STM images: (A) initially physisorbed adlayer at 0.47 V; (B) disordered structure after the fast reorientation at 0.90 V; (C) initially aligned stripe-like structure at 0.90 V (< 15 min); (D) final long-range ordered structure (> 15 min).

5.3 Benzoic Acid and Isophthalic Acid

In order to address the local structure of chemisorption, the SEIRAS of chemisorbed TMA has been compared with BA and IA in Section 5.2.1.2.2. There are still several important aspects to discuss, for example, the influence of the molecular structure, especially the number and position of functional -COOH groups on the molecular orientation, the lateral hydrogen-bonding and the substrate/adsorbate interaction.

To avoid the complicated lateral interaction upon the interfacial over-saturation or the formation of multilayer [127], both EC and SEIRAS measurements on BA, IA were carried out at moderate coverages, which are controlled by limiting their concentrations in the bulk electrolytes (BA: 3 mM, IA: 0.5 mM).

5.3.1 CV and STM

The CVs and STM images of BA and IA are presented in Fig. 5-14. Each CV is separated into two potential ranges, physisorption and chemisorption, by a pair of broad current peaks (~ 0.80 V) which correspond to the adsorption/desorption of the BA or IA molecules, respectively. The values of the double layer capacitance are almost the same as for TMA, indicating a similar chemical composition of the adlayers (carboxylic acid, ClO_4^- and H_2O).

In addition, several small current peaks are observed overlapping with the broad adsorption/desorption current peaks of IA and TMA (dotted line in Fig. 5-14 IA, and P_1/P_1'~P_3/P_3' in Fig. 5-1), indicating phase transitions upon chemisorption. They become sharper after a potential pre-conditioning in the positive potential range $1.0 < E < 1.2$ V (~ 15 min potential cycling, 50 mV s^{-1}), where long-range ordered chemisorbed adlayers are formed [45]. This conclusion is supported by STM results [45,127].

The surface coverages can be estimated from the STM images. The coverages of the chemisorbed adlayer decrease in the sequence BA (6.6×10^{-10} mol cm^{-2}) > IA (5.0×10^{-10} mol cm^{-2}) > TMA (3.1×10^{-10} mol cm^{-2}), which is consistent with the size of the individual molecules. These observations are in agreement with the maximum surface coverage of BA (7.3×10^{-10} mol cm^{-2}) reported by Li et al. [128].

The CVs obtained for the Au(111-25 nm) film electrode show similar physisorption/chemisorption transition properties. Detailed structure characteristics of BA and IA were also investigated by in situ SEIRAS on the Au(111-25 nm) film electrodes.

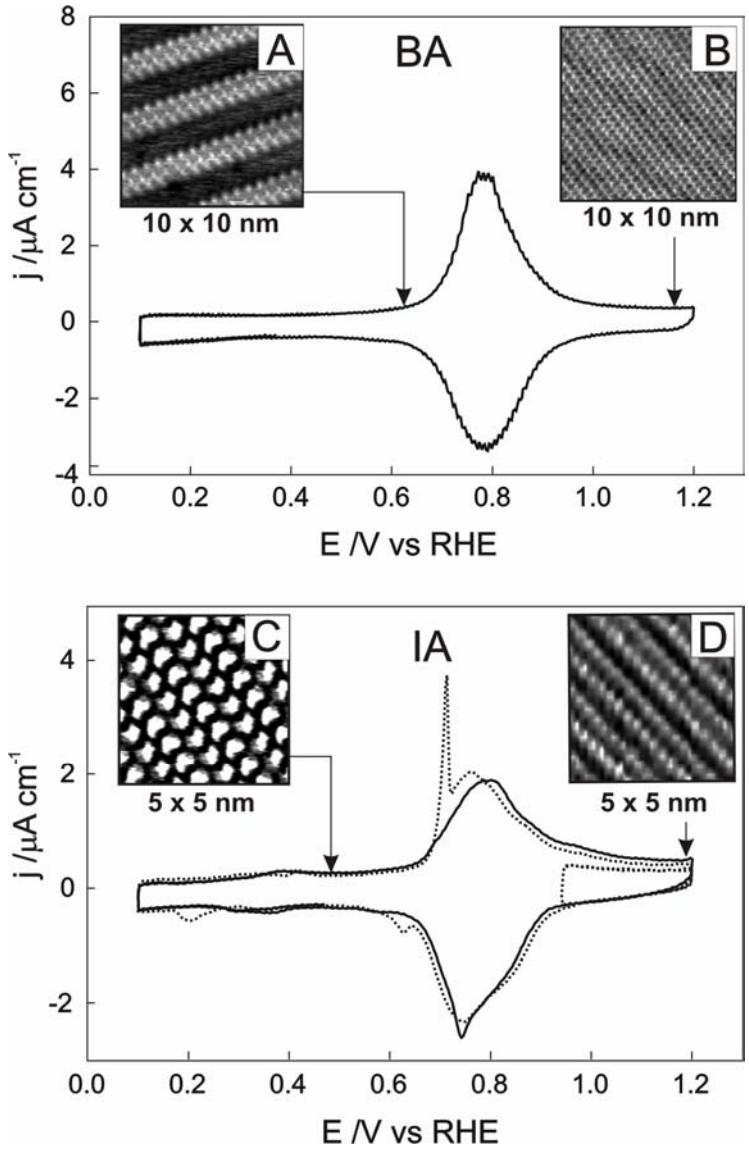

Fig. 5-14: CVs of a Au(111) electrode (miscut angle < 0.2°) in 3 mM BA (upper) and 0.5 mM IA (below) in 0.1 M $HClO_4$, scan rate of 10 mV s^{-1}. The solid lines represent the steady-state CV recorded after three complete potential cycles, the dotted line of IA was obtained after 10 min cycling in 0.85 V to 1.20 V. The insets (A), (B), (C) and (D) represent high-resolution in situ STM images of the ordered phases recorded at 0.65 V, 1.20 V (BA), and 0.45 V, 1.20 V (IA), respectively.

5.3.2 SEIRAS

The overall SEIRA spectra of the chemisorbed BA and IA adlayers were already shown in Fig. 5-5. The vibrational bands around 1380 cm^{-1} can be unambiguously assigned to the $\nu_{s(OCO)}$ modes of the COO^- for all chemisorbed states of BA, IA and TMA. The potential dependencies of the band intensities during the slow scan measurements exhibit similar trends as for TMA. With the breaking of the

physisorbed hydrogen-bonded network, orientations of both BA and IA change from planar to tilted or perpendicular in a positively potential sweep. At positive potentials, the IA molecules are also coordinated onto the substrate surface via one deprotonated COO^- group, leaving another -COOH side-group available for intermolecular hydrogen-bonding. Such hydrogen-bonded models are supported by the STM image of the chemisorbed IA adlayer in Fig. 5-14.

Without going into every detail, the discussion in this section is focused on the potential dependence of vibrational frequencies, which is related to the lateral hydrogen-bonding and substrate/adsorbate interaction. The plots of the vibrational frequency versus the potential, recorded during a slow scan (0.1 ~ 1.2 V, 10 mV s^{-1}), are presented in Fig. 5-15. As shown in Table 4-1, the potential-induced band shift decreases in the sequence of BA > IA > TMA.

Among the three factors usually leading to the potential dependencies of band frequencies, dipole-dipole coupling can be considered for the close-packed stacking of the chemisorbed BA structure at a high coverage, shifting the $\nu_{s(OCO)}$ mode to a higher wavenumber [121]. However, it can be ruled out in the cases of IA and TMA due to a rather large intermolecular distance. Therefore, the frequencies of the $\nu_{s(OCO)}$ mode of IA and TMA are mainly determined by the Stark tuning effect (blue shift at positive potential) and the electron back donation (red shift at positive potential). The former analysis on TMA suggests a compensation of Stark tuning by a strong electron back donation from a highly conjugated TMA molecule to the positively charged substrate, which provides a very small band shift. However, such a conjugation effect becomes less pronounced with the decreasing number of -COOH substitutes in case of IA and BA. The less delocalized π-systems block the donation of electrons back to the substrate, and give a larger blue shift following the sequence: TMA < IA < BA.

In addition, the $\nu_{s(OCO)}$ frequency at a stable chemisorbed state shows the following sequence: TMA (1376 cm^{-1}) < IA (1383 cm^{-1}) < BA (1390 cm^{-1}), indicating a decreasing substrate/adsorbate interaction with a small number of COOH substitutes, and an increasing dipole-dipole coupling. The correlation between the decreased $\nu_{s(OCO)}$ frequency and the increased substrate/adsorbate interaction is further supported

by the red shift of the $\nu_{s(OCO)}$ band during the slow alignment of the chemisorbed TMA adlayer (see Fig. 5-9).

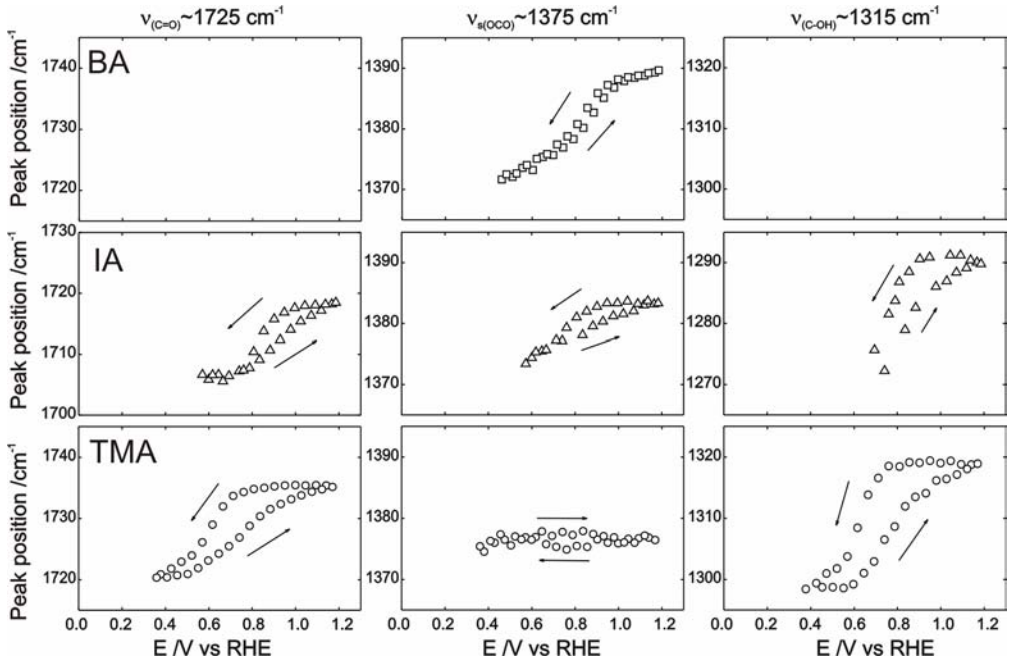

Fig. 5-15: Potential dependencies of the peak positions of the $\nu_{(C=O)}$ (~ 1725 cm^{-1}), $\nu_{s(OCO)}$ (~ 1375 cm^{-1}) and $\nu_{(C-OH)}$ (~ 1315 cm^{-1}) bands of BA (□), IA (Δ) and TMA (○) as obtained from a slow potential scan at 10 mV s^{-1}.

The intensity ratios between the $\nu_{(C=O)}$ and the $\nu_{(C-OH)}$ modes of IA and TMA are similar, indicating that the -COOH groups in both systems belong to the same type of -COOH side-groups with similar orientations in the hydrogen-bonded network.

A strong blue shift is observed for the $\nu_{(C=O)}$ and $\nu_{(C-OH)}$ modes of IA and TMA. Both $\nu_{(C=O)}$ and $\nu_{(C-OH)}$ bands of TMA appear at higher wavenumbers (15~30 cm^{-1} higher) than those for IA. Due to the large distance from the substrate, their frequencies are weakly influenced by the Stark effect from the strong electric field, which dominates only in the vicinity of electrode surface. Alternatively, an indirect electron donation to the -COOH side-groups should be considered together with an additional contribution from the directional hydrogen-bonds. The latter should increase the in-plane $\nu_{(C=O)}$ and $\nu_{(C-OH)}$ frequencies, as supported again by the observation of the blue shift during the adlayer alignment via hydrogen-bonds (see Fig. 5-9).

5.4 Summary

We have investigated the adsorption and phase formation of TMA on Au(111) single crystal and Au(111-25 nm) film electrodes in 0.1 M $HClO_4$ by combining in situ ATR-SEIRAS with simultaneous electrochemical experiments.

At 0.10 V (starting potential), TMA molecules are randomly adsorbed on the negatively charged gold surface in a planar orientation together with weakly hydrogen-bonded interfacial water molecules. In phase I, 0.10 < E < 0.50 V, planar oriented TMA molecules form a 2D-ordered physisorbed adlayer. STM experiments show that the TMA molecules are interconnected by centrosymmetric hydrogen-bonds giving rise to a honeycomb network of open rings. Weakly hydrogen-bonded water species are displaced by the organic molecules. At more positive potentials, but still in phase I (E > 0.30 V), TMA molecules at grain boundaries and defect sites start to tilt and break apart the long-range hydrogen-bonded network. At higher potentials, in 0.58 V < E < 0.75 V (phase II), a close-packed physisorbed adlayer composed of linear dimers forms slowly, but only on ideally smooth domains of the electrode surface, accompanied by the replacement of additional interfacial water species. Further increase of the electrode potential, 0.75 V < E < 0.88 V (phase III_a), causes an orientation change from planar to perpendicular, accompanied by the deprotonation of one -COOH group which is chemically bonded to the positively charged electrode surface. Each TMA molecule is chemisorbed via one carboxylate group in the “atop” model leaving the two -COOH side-groups available for further hydrogen-bonding between neighboring TMA molecules. Simultaneously, two types of water species start to co-adsorb, weakly hydrogen-bonded water at intermolecular defect sites and strongly hydrogen-bonded water interacting with the non-coordinated -COOH side-groups. The chemisorbed TMA molecules are still mobile and not yet incorporated into an ordered 2D network. Phase III_a represents a “disordered chemisorption” phase. At E > 0.90 V, in region III_b, almost all surface coordinated TMA molecules are interconnected via intermolecular hydrogen-bonds between adjacent -COOH side-groups, resulting in a stable and highly ordered ladder network.

The formation kinetics of the chemisorbed TMA adlayer was explored by electrochemical transient experiments and time-resolved ATR-SEIRAS employing

rapid-scan and step-scan acquisition modes. The analysis of the SEIRAS transients shows that the formation of chemisorbed TMA in phase III_b proceeds in two steps: (i) TMA molecules change their orientation from planar to tilting or perpendicular accompanied by the deprotonation of one carboxyl group immediately after a potential step in region III. This process involves the breakdown of the hydrogen-bonded network of the physisorbed phase I and a fast incorporation of additional TMA molecules from the bulk electrolyte into the interfacial region. The process follows a Langmuir-type kinetics indicating randomly triggered orientation changes with rather weak lateral interactions between the active species; (ii) In a subsequent and much slower process the chemisorbed TMA molecules start to gradually align into a highly ordered 2D network III_b. At the same time, strongly hydrogen-bonded and isolated water species appear to be co-adsorbed with TMA molecules.

The comparison with BA and IA shows that the interfacial orientation of these molecules in the respective adlayers have a similar potential dependence as TMA, changing from planar to tilted and finally perpendicular during an positive-going potential sweep. Both substrate/adsorbate interaction and intermolecular hydrogen-bonding are strongly dependent on the number of -COOH groups.

Based on a detailed analysis of carboxyl and carboxylate vibration modes and OH-stretching modes, the present ATR-SEIRAS study provides a comprehensive understanding of the steady-state structures and dynamic changes as triggered by the electrode potential. The combination of macroscopic electrochemical experiments, in situ STM and SEIRAS reveals details of structure changes and of the chemical composition of TMA, IA, and BA adlayers on well defined gold/electrolyte interfaces.

Chapter 6. Viologen

6.1 Introduction

Viologen are formed by diquaternizing of 4,4´-bipyridine to 1,1´-disubstituent-4,4´-bipyridilium salts with counter anions to balance its positive charge [23]. The redox-active viologens occur in three different oxidation states: the oxidized dication V^{2+}, the one-electron reduced radical monocation $V^{\bullet+}$, and the fully reduced neutral V^0, which may transform into each other in two sequential one-electron processes according to: $V^{2+} \leftrightarrow V^{\bullet+}$ and $V^{\bullet+} \leftrightarrow V^0$ [23,129]. Derivatives of viologen have been used in various applications such as functional polymers [130], biosensors [131], liquid crystals [132], photo energy conversion [133], complex-stabilized metal particles [134] and luminent materials [135]. Reviews on the research and applications of viologens can be found in the book of Monk [23] and the literatures cited therein. Recently, viologens were incorporated as "backbone-components" in self-assembled monolayers [136, 137], nanometer-scale electronic switches, and various functional materials [138,139] employing the precise control of their redox states upon electrochemical polarization.

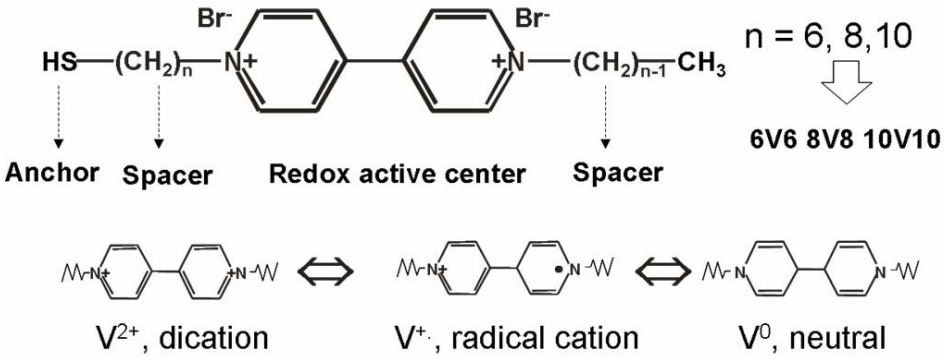

Scheme 6-1: Molecular structure and redox reactions of viologen.

The redox electron transfer (ET) of viologens has been extensively studied both in solution and immobilized on electrode surfaces employing electrochemical techniques [140,141,142,143,144]. The thermodynamic redox potential is strongly dependent on the hydrophobic/hydrophilic environment and hydration capacity of the

co-adsorbed anions [140,143]. An ion-pair mechanism has been proposed in the presence of ClO_4^- as counter anions, leading to rather complex charge transfer kinetics [140].

Vibrational spectroscopy (Raman and IR) characterization shows the co-existence of monomeric and dimeric radical cations. The latter are formed as a face-to-face sandwich structure, with strong spin-pair interaction of radical electrons, which are delocalized over the whole bipyridinium cores [141,142,143,145,146,147]. Monomer/dimer equilibrium of radical cations, and their dependence on the anions and the alkyl chain lengths have been characterized in detail [141,142]. Aging effects originating from structure re-arrangement of redox centers and counter anions are proposed to decrease the reversibility of the ET reactions [146]. The kinetic study of the redox processes for heptyl-viologen on Pt electrodes were studied by EC chronoamperometry, electron reflectance [142], time resolved SEIRAS and resonance Raman spectroscopy [146]. Combined with electrochemical methods, vibrational spectroscopy provides comprehensive and complementary understanding of the intrinsic structure and chemical changes at a molecular level.

In this chapter, we focus on the redox-activity of N-hexyl-N´-(6-thiohexyl)-4,4´-bipyridinium bromide (monothiol 6V6) immobilized on gold electrodes in an electrochemical environment. As illustrated in Scheme 6-1, each tailored molecule is composed of a redox-active bipyridinium center, two flexible alkyl-spacer units and one or two terminal thiol anchor groups. The self-assembly and redox-functionality of thiol-functionalized viologens on gold macro-electrodes has been investigated by cyclic voltammetry [139,140,141,142,143,148], UV-vis-absorption [149], IR [136] and Raman spectroscopy [145], quartz crystal microbalance [140, 150], electro-reflectance [141], ex-situ STM [137], and STS [136]. Most of the conclusions from the electrochemistry of viologen species in electrolyte solution can be applied to a surface-immobilized monolayer.

Motivated by the pioneering work of the Liverpool group on single molecule conductivity [53], we also took efforts to address the ET characteristics of redox-active, thiol-functionalized viologens, to explore the relations between molecular structure and electronic properties from macroscale self-assembled monolayers to the single-molecular junction in STM approach [151]. As a part of this topic, the in situ

SEIRAS characterization of structure and chemical functionality of self-assembled viologen monolayers immobilized on gold electrodes has been carried out in the present dissertation work.

The present chapter is organized in the following way:

(i) Steady-state electrochemical studies (CV) of viologen SAMs on Au (111) single crystal macro-electrodes will provide a general understanding of the redox properties; (ii) The structures of quasi-steady states for V^{2+} and $V^{\bullet+}$ will be explored by in situ SEIRAS; (iii) Based on the knowledge of structures at different redox states, attempts to investigate the kinetics involved in the whole redox ET reaction ($V^{2+} \rightarrow V^{\bullet+}$) will be presented based on the results from chronoamperometry and time resolved SEIRAS measurements.

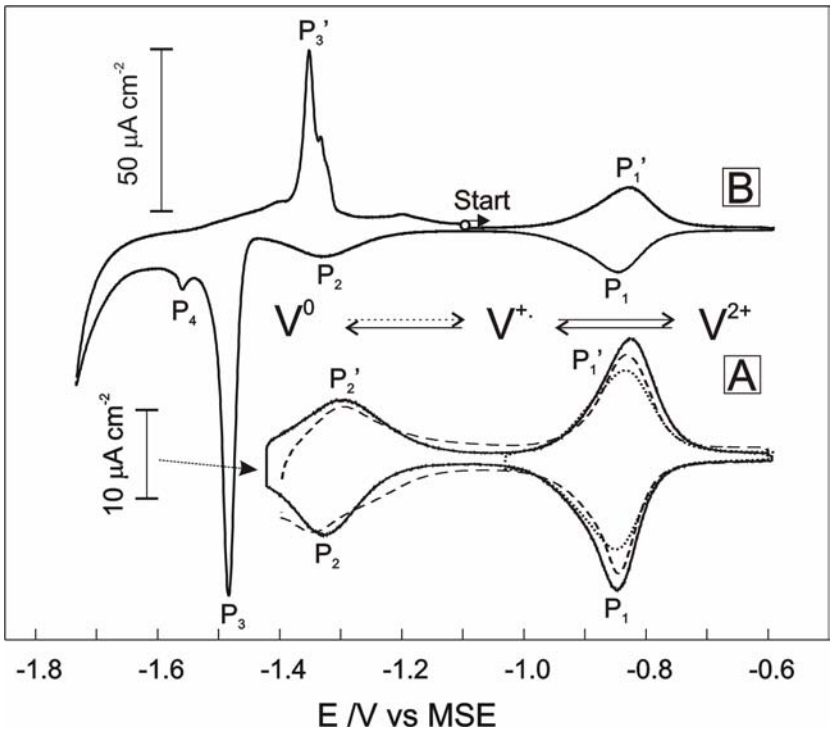

Fig. 6-1: CVs of 6V6 SAMs on Au electrodes. Contact with the electrolyte was established at E = -0.60 V. Sweep rates are 50 mV s^{-1}. The characteristic current peaks are labeled P_1/P_1', $P_2/P_2'$and P_3/P_3'. (A) CVs of 6V6 SAM on a Au(111) single crystal electrode in 0.05 M $KClO_4$, pH adjusted to 10 with NaOH (solid line), on a Au(111-25 nm) film electrode at pH~10 (dashed line), and on a Au(111) single crystal electrode in neutral solution (dotted line); (B) the 1st cycle of the CV of the 6V6 SAM on a Au(111) single crystal electrode with reductive desorption in 0.05 M $KClO_4$, pH ~ 10. The electrode potential was first scanned in the positive direction starting from -0.60 V.

6.2 General Electrochemical Characterization (CV)

The SAM of viologen on a Au(111) electrode was first characterized by cyclic voltammetry. Fig. 6-1 shows typical CVs of a Au(111)-(1×1) electrode modified with a monolayer of HS-6V6-H, in contact with 0.05 M $KClO_4$ (pH ~ 10). The potential scan rate is 50 mV s^{-1}. Restricting the potential range to -1.45 < E < -0.60 V results in two pairs of well-defined current peaks P_1(-0.85 V)/P_1´ (-0.82 V) and P_2(-1.33 V)/P_2´ (-1.30 V) (Fig. 6-1A), which represent the characteristic 1st ($V^{2+} \leftrightarrow V^{\bullet+}$) and 2nd ($V^{\bullet+} \leftrightarrow V^{0}$) one-electron redox processes of the viologen moiety, respectively [23]. Both will be discussed separately in the next two sections.

6.2.1 1st redox process: $V^{2+} \leftrightarrow V^{\bullet+}$

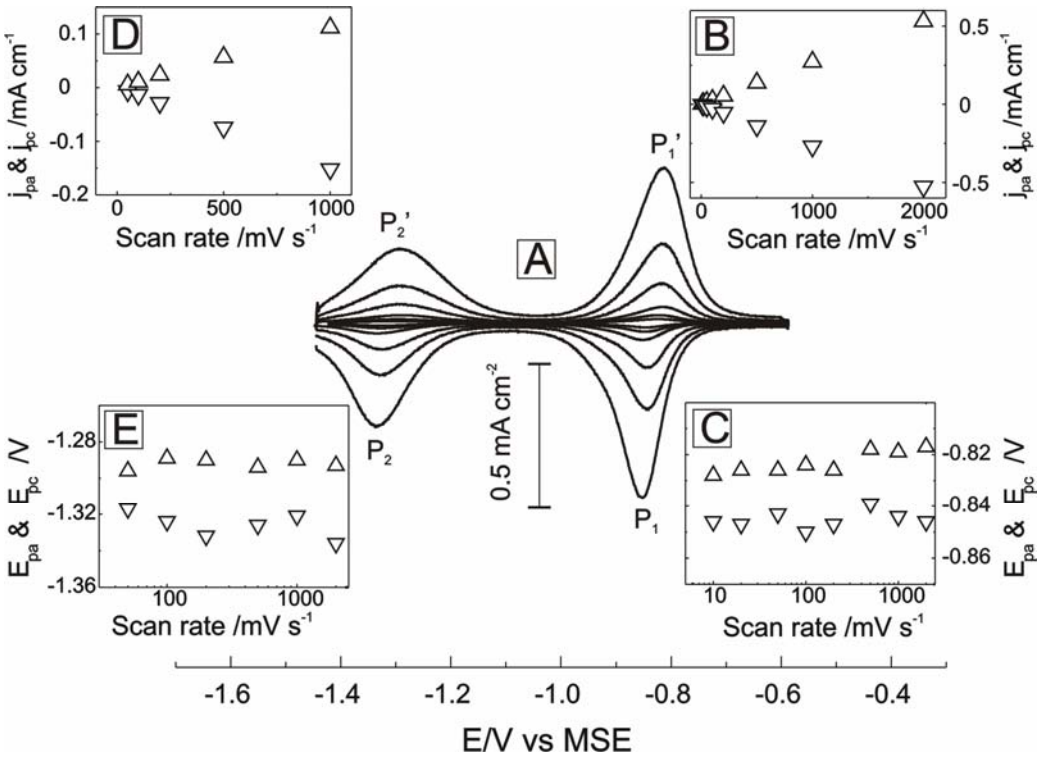

Fig. 6-2: (A) CVs of a 6V6 adlayer on a Au(111) single crystal electrode in 0.05 M $KClO_4$, pH ~ 10. The scan rates range from 10 mV s^{-1} ~ 2 V s^{-1}; (B, C) Scan rate dependencies of the peak currents j_{pa}/j_{pc} and of the peak potentials E_{pa}/E_{pc} for the 1st redox process; (D, E) Scan rate dependencies of the peak currents j_{pa}/j_{pc} and of the peak potentials E_{pa}/E_{pc} for the 2nd redox process. The anodic and cathodic scan directions are labeled as (△) and (▽), respectively. The solution resistance was compensated by applying a positive feedback.

Fig. 6-2A shows the CVs of the 1st and 2nd ET processes recorded at different potential sweep rates (10 ~ 2000 mV s^{-1}) and plots of the peak currents and potentials vs. the sweep rate. The current peaks P_1/P_1' are completely reversible during the potential cycles (Fig. 6-2A). Peak-to-peak separations of P_1/P_1' are rather constant up to 2 V s^{-1} (Fig. 6-2C), and the peak current scales linearly with the scan rate (Fig. 6-2B). The FWHM is 0.091 V for both P_1 and P_1'. These observations indicate a fairly reversible process, in which the redox active species are confined to the electrode surface [12]. The migration of counterions and the reorganization of solvent molecules appear to be rather fast [143].

The formal potential $E^{0'}$ (estimated as the midpoint between the anodic and cathodic peak potentials) is much more negative than that reported for Cl^-, Br^- and SO_4^{2-} containing electrolyte [140,143], indicating a possible exchange of hydrophilic Br^- by the hydrophobic ClO_4^- ions when working in $KClO_4$ as supporting electrolyte solution. This is because the hydrophobic ClO_4^- can easily permeate through the alkyl chains to reach the redox centers due to its small hydrated diameter [140]. This issue will be addressed in detail in Section 6.3.

The peak-to-peak separation (ΔE_p ~ 20 mV) represents some complexity of the ET process, such as changes in solvation (hydrophobicity/hydrophilicity), as well as the interaction between redox active species and counterions [140,11]. One possible explanation is the ion pairing effect [152, 153, 154] with a strong electrostatic interaction between the V^{2+} centers and the hydrophobic ClO_4^- anions. Similar mechanism of ion pair formation has been proposed for ferrocenium/ClO_4^- [155,156].

The adlayer capacitance C_{dl} is estimated to be 8.8 μF cm^{-2} in -0.70 V < E < -0.60 V. Although the value of C_{dl} is larger than that of alkanethiol SAMs [157] due to the incorporation of water molecules or ions, it is much smaller than that of systems in the presence of SO_4^{2-} counterions [141], indicating the formation of a compact 6V6 monolayer on Au(111) surface. It is comparable with the data reported for a highly ordered 18V2 viologen monolayer on an n-hexanethiol coated Au electrode (9 μF cm^{-2}) [143].

Systematic studies on the modification of a Au(111) single crystal electrode with 6V6 reveal that a complete monolayer was obtained upon deposition from 1 mM

ethanolic solution and annealing at 60 ^{o}C at incubation times longer than one hour. No evidence for multilayer formation was obtained when oxygen was carefully excluded. By integrating the area under the current curves and considering a single ET process ($V^{2+} \leftrightarrow V^{\bullet+}$), the charge transfer can be estimated as ~30 μC cm^{-2}, corresponding to a surface coverage ~ (3.5 ± 0.3) × 10^{-10} mol cm^{-2} (~ 47 Å^2 per molecule). This value is in good agreement with literature data reported for related systems (41 ~ 55 Å^2) [139,140,145, 158]. It is significantly smaller than the projected area of a planar oriented 6V6 molecule (c.f. crystal structure data in Ref. [159,160]) but larger than the estimated cross section of an all-trans oriented alkanethiol in a densely packed self-assembled monolayer (18 ~ 20 Å^2) [19]. This qualitative discussion points to a tilted orientation of the viologen moiety with respect to the surface normal as suggested by Sagara et al. [141].

6.2.2 2nd redox process: $V^{\bullet+} \leftrightarrow V^0$

The peak-to-peak separation ΔE_p of P_2/P_2' is constant around 32 mV for a scan rate up to 1 V s^{-1} (Fig. 6-2E). The peak heights scale linearly with the scan rate (Fig. 6-2D). The current peaks are less reversible compared with P_1/P_1'. A decay in the peak current of P_2/P_2' was observed after long-time potential cycling in -1.10 < E < -1.43 V. The $V^{\bullet+} \leftrightarrow V^0$ reaction shows under our experimental conditions as “quasi-reversible”. Compared to P_1/P_1', the quasi-reversibility of P_2/P_2' is also indicated by larger values of both FWHM and ΔE_p, which are estimated to be 0.110/0.132 V and 32 mV, respectively. The large FWHM could be related to the penetration of anions, the uneven distribution of the redox centers, or the aggregation of different $V^{\bullet+}$ species [11]. A direct spectroscopic study is necessary to explore the possible origins. The lower reversibility of the 2nd process $V^{\bullet+} \leftrightarrow V^0$ is attributed to the insolubility and/or aging tendency of the V^0 species [11,146], which generate heterogeneity within the monolayer. This explanation is also supported by a larger value of the integrated charge transfer involved in the cathodic sweep, as compared to the anodic one.

In the structure studies we will focus on the steady-state and kinetic properties of the viologen monolayer during the first redox process: $V^{2+} \leftrightarrow V^{\bullet+}$.

6.2.3 Reductive desorption

Further negative potential excursion generates two sharp current peaks P_3(-1.48 V) and $P_3´$(-1.35 V) (Fig. 6-1B), which are assigned to the irreversible reductive desorption, and a partial oxidative re-adsorption of a redox-active thiolate, respectively [24,161]. Current integration of P_3, after correction of the double layer contribution, yields an overall desorption charge of 160 ± 10 μC cm^{-2}, which is considerably larger than the redox charge transfer (~ 30 μC cm^{-2}) and typical values reported for alkanethiols (~ 70 μC cm^{-2}) [157]. The large overall charge and the sharpness of this current peak indicate parallel contributions from additional faradaic processes [11,142].

Besides the main desorption peaks $P_3/P_3´$, a less intense negative-going peak P_4 appears at more negative potential ~ -1.95 V, which could be assigned to the precipitation of crystallites of insoluble $V^0/V^{\bullet+}$ reactants [144, 162]. Subsequent multiple cycling in -1.70 V < E < -0.60 V results in a rather distorted CV characteristics with continuously decreasing current. This is related to the loss of active $V^{\bullet+}$ thiolate from the monolayer after breaking the S-Au anchors.

6.2.4 Dependence on the alkyl chain lengths

Fig. 6-3 shows the CVs of the 1st redox process of monothiols of 6V6, 8V8, and 10V10. The parameters of all current peaks are summarized in Table 6-1. The CVs of 8V8 and 10V10 show similar symmetric and reversible 1st redox peaks $P_1/ P_1´$, and also rather similar values of adlayer capacitance (C_{dl} ~ 9.0 μF cm^{-2}) as 6V6.

The peak current of the viologen monothiols increases slightly with the length of the alkyl chain, indicating the following sequence of the surface coverage: 6V6 < 8V8 < 10V10, which is in agreement with the observations of alkanethiol SAMs. Longer alkyl chains exhibit stronger van der Waals interactions, which result in an increasing 2D adlayer order [11]. Considering the increase of the spatial size along the alkyl chain axis with increasing number of CH_2 units, the surface coverage should have decreased according to 6V6 > 8V8 > 10V10 if the molecules were aligned parallel to the substrate. A reversed trend in the surface coverage indicates however a tilted orientation of the viologen molecules within the SAM. The spatial increase for

longer alkyl chains is only in the all-trans direction along the chain axis. This conclusion is supported by further SEIRAS results (Section 6.3).

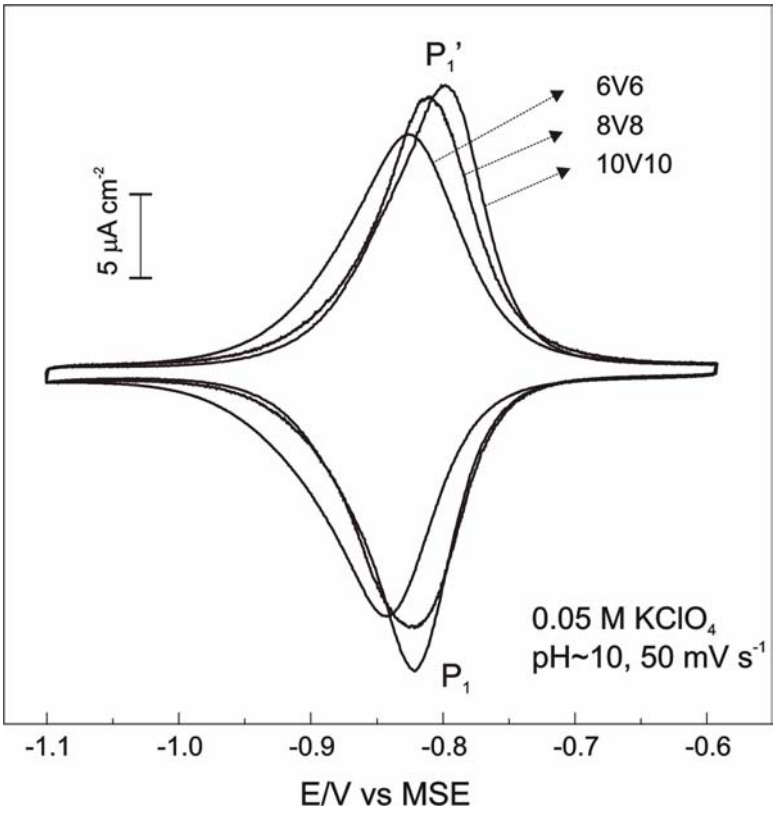

Fig. 6-3: CVs of monothiol 6V6, 8V8 and 10V10 SAMs on a Au(111) single crystal electrode (the 1st redox process).

The anodic and cathodic peak potentials shift towards positive values with increasing alkyl chain length, i.e. the distance between the redox moiety and the monolayer/solution interface. V^{2+} is hydrophilic and usually hydrated, while $V^{\bullet+}$ is rather hydrophobic. Long alkyl chains provide a hydrophobic environment, which favors $V^{\bullet+}$ rather than V^{2+} species. Therefore, the prevailing $V^{\bullet+}$ will push the $V^{2+}/V^{\bullet+}$ equilibrium potential to positive values [140]. A similar positive potential shift induced by increasing of the alkyl chain lengths has been observed in other systems like ferrocenylalkane thiols [155].

The average FWHM values of the current peaks become smaller with increasing alkyl chain lengths, indicating that the attractive interaction between redox active centers is enhanced [156]. Such attractive interactions may also originate from ion-pairing interaction [140], together with the π-stacking between bipyridinium planes. It

is further enhanced by the hydrophobic environment and strong alignment effect provided by the van der Waals interactions between neighboring alkyl chains.

Table 6-1: CV parameters of monothiol viologen with different alkyl chain lengths.

1st Redox	ΔE_p (< 2 V s^{-1})	Peak position (< 1 V s^{-1})	$E^{0'}$ /V Approx.	FWHM	Γ /x 10^{-10} mol cm^{-2}	Desorption potential /V
6V6	0.020	-0.825	-0.835	0.103	3.31	-1.48
		-0.845		0.097		
8V8	0.018	-0.807	-0.816	0.092	3.42	-1.49
		-0.825		0.080		
10V10	0.017	-0.801	-0.809	0.084	3.51	-1.48
		-0.818		0.077		

Within the experimental error, the potential difference between cathodic and the anodic peaks is almost constant (~ 19 mV) for viologen with different alkyl chain lengths. Such an independence of ΔE_p on the alkyl chain length indicates that the kinetics involved in the 1st redox process is mainly determined by the redox centers themselves, or the local solvent/anion vicinity.

Based on the above discussion, CV results provide understandings of the overall redox behaviors and the general stability of the viologen SAMs on Au electrodes. However, the molecular structure and chemical composition of these SAMs as well as the local environment (anions, solvent molecules) cannot be directly probed without other structure-sensitive characterization techniques. To explore the factors involved in the redox process comprehensively, in situ SEIRAS investigations were carried out on viologen modified Au film electrodes.

6.2.5 CV on Au(111-25 nm) film and in neutral electrolyte solution

Au(111-25 nm) film electrodes are used as an approach to Au(111) single crystal electrodes in the SEIRAS characterization of the 1st redox process of viologen SAMs. Fig. 6-1A shows the CVs of a Au(111-25 nm) film electrode modified with 6V6 at pH ~ 10 (dashed line), and of a Au(111) single crystal electrode modified with 6V6 in neutral solution (dotted line).

The scan rate dependence of the 1st redox peak P_1/P_1' reveals the similar EC properties of Au(111-25 nm) film and Au(111) electrodes modified with 6V6. The larger adlayer capacitance (~11.5 μF cm^{-2}) and the lower surface coverage (~

3.09×10^{-10} mol cm^{-2}) on the film electrode are due to the partially polycrystalline features, resulting in a less uniform adlayer, which may lead to an additional incorporation of solvent molecules [35,116]. The 2nd redox current peaks $P_2/P_2´$ are quasi-reversible and slightly distorted during the negative sweep.

The IR investigations were mainly carried out in neutral supporting electrolyte to protect the glass IR cell and the Si prism from being etched. For comparative reasons, we also investigate the redox properties of 6V6 modified gold electrodes in neutral (pH ~ 7) and alkaline (pH ~ 10) electrolyte. The CV measurements in neutral solution were limited to E > -1.20 V to avoid hydrogen evolution. The general CV features and the detailed scan rate dependencies reveal similar characteristics in both supporting electrolytes.

Therefore, the IR investigations of the 1st redox process of the viologen SAMs can be reliably carried out in neutral solution on modified Au(111-25 nm) film electrodes.

6.3 SEIRAS

6.3.1 Steady-state V^{2+} structure

The most stable redox state of viologen is the bipyridinium dication (V^{2+}) [23]. In the light of the electrochemical CV results, the V^{2+} dications are stabilized when the potential is carefully held at -0.60 V (Fig. 6-1). The structure of a steady-state V^{2+} SAM was therefore investigated on a dry surface in argon atmosphere and on the solid/liquid interface at -0.60 V in the spectroelectrochemical cell.

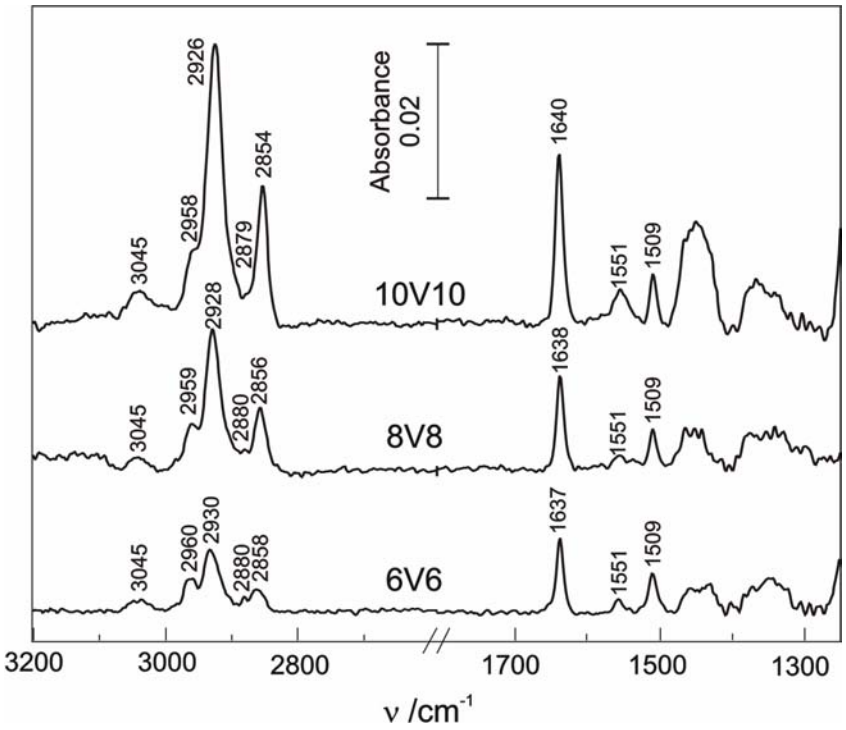

Fig. 6-4: Ex situ SEIRA spectra of as-prepared monothiol 6V6, 8V8, 10V10 adlayers on Au(111-25 nm) electrodes (spectral regions: 3200 ~ 2800 cm^{-1} and 1750 ~ 1100 cm^{-1}). The plotted absorption spectra represent the "dry" viologen monolayers obtained after careful rinsing with bare ethanol and subsequent evaporation of the solvent in a gentle stream of argon. The reference spectrum was obtained on a bare Au(111-25 nm) electrode in the flow of dry argon. Each spectrum is the average of 256 single spectra.

The preparation and characterization of the adlayers were strictly carried out in the absence of oxygen. The film was first immersed into 0.5 mM ethanolic solution of the respective viologen derivatives for 6 h at elevated temperature (~ 60 ^{o}C), subsequently rinsed with pure ethanol to remove physisorbed species, dried in a stream of argon, and finally mounted onto the spectroelectrochemical cell during argon purging. An aqueous solution of 0.05 M $KClO_4$ was pre-deaerated and used as supporting electrolyte. The conditions of viologen monolayer are defined as "dry" and "wet" SAMs, before and after contacting with the supporting electrolyte solution, respectively.

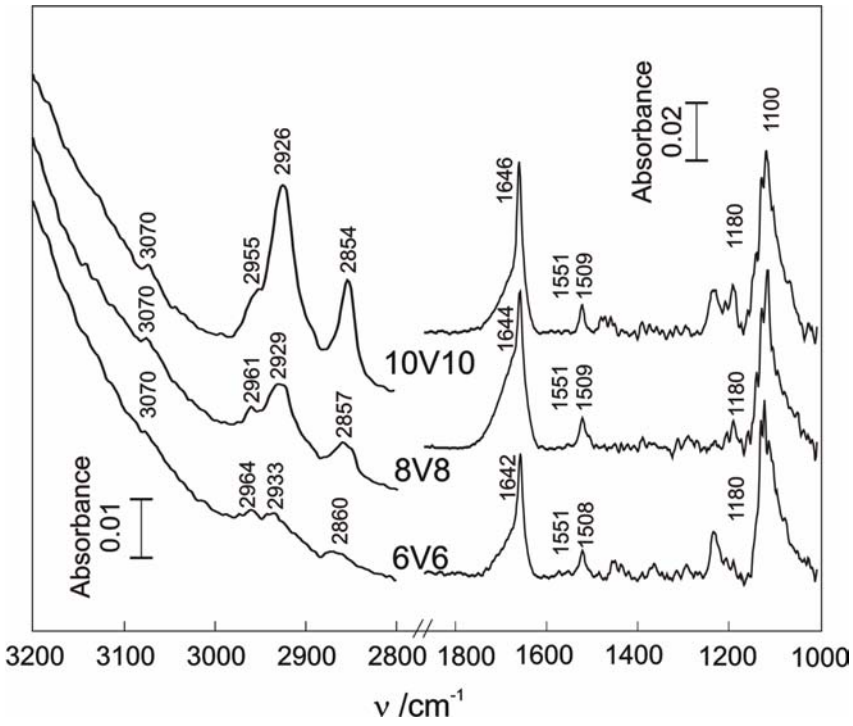

Fig. 6-5: In situ SEIRA spectra of monothiol 6V6, 8V8, 10V10 adlayers on Au(111-25 nm) electrodes, for the dication form (V^{2+}) recorded at E = - 0.600 V in 0.05 M $KClO_4$, pH ~ 7. The reference spectrum was obtained in the absence of viologen in 0.05 M $KClO_4$, pH = 7, at E = -0.600 V. The plotted absorption spectra represent "wet" viologen monolayers. Each spectrum is the average of 256 single beam spectra.

The corresponding SEIRA spectra of 6V6, 8V8 and 10V10 are showed together in Fig. 6-4 and Fig. 6-5. Fig. 6-4 represents the SEIRA spectra of "dry" SAMs with the reference spectrum acquired on the bare gold surface in argon atmosphere. Fig. 6-5 shows the spectra of "wet" SAMs in contact with a supporting electrolyte solution at -0.60 V, with the reference spectrum measured on the bare gold surface in adsorbate-free supporting electrolyte at the same potential. Three main groups of viologen-related vibration modes are observed at 1750 ~ 1000, 3000 ~ 2800 and 3000 ~ 3100 cm^{-1}, corresponding to the ring vibrational modes of bipyridinium planes, the C-H stretching of alkyl chains, and the in-plane aromatic C-H stretching of bipyridinium rings, respectively. In addition, the HOH-bending modes ($\delta_{(HOH)}$ ~ 1650 cm^{-1}) and the broad OH-stretching modes ($\nu_{(O-H)}$ 2800~3600 cm^{-1}) of co-adsorbed water species are observed in the wet spectra. With an enhancing distance ~ 5 nm perpendicular to the substrate surface [40] and a maximum length of the viologen molecules ranging between 2.6 to 3.8 nm (for 6V6, 8V8, 10V10) [151], the $\nu_{(O-H)}$ mode may also contain contributions of bulk H_2O.

6.3.1.1 Ring vibrations

As observed on the "dry" SAM of 6V6 (Fig. 6-4), the vibration bands of the bipyridinium ring below 1750 cm^{-1} are assigned to in-plane dipole moment components parallel either to the long molecular axis, as defined in Scheme 5-2 by the 4,4´-N,N´-direction (B_{3u} in D_{2h} symmetry: 1637, 1509 cm^{-1}), or to the short molecular axis (B_{2u} modes in D_{2h} symmetry: 1551, 1450, 1355 cm^{-1}) [146,163,164,165,166].

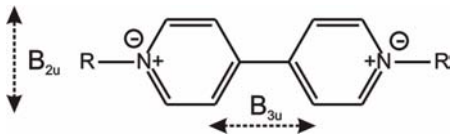

Scheme 6-2: Schematic view of the V^{2+} molecular structure of the viologen. The B_{3u} and B_{2u} axis correspond to the long and short molecular axis, respectively.

The broadening feature at 1450 and 1355 cm^{-1} in the "dry" SAMs is probably due to the interference from the symmetric H-C-H scissor modes of the CH_2/CH_3 units [163]. This assumption is supported by in situ studies of the self-assembly process.

Similar modes of bipyridinium ring vibrations are also observed on the SAM/electrolyte interface in Fig. 6-5 ("wet") at 1642, 1508, 1225, 1180 cm^{-1} (B_{3u}), and 1450, 1355, 1280 cm^{-1} (B_{2u}), superimposed with the $\delta_{(HOH)}$ and the broad $\nu_{(O-H)}$ bands of interfacial water. In addition, a prominent peak appears at 1100 cm^{-1}, which is attributed to the symmetric Cl-O stretching mode ($\nu_{(Cl-O)}$) of ClO_4^- incorporated into the adlayer lattice, which replace the original Br^-. These findings support our previous hypothesis.

Referring to the surface selection rule of SEIRAS, the observation of the B_{2u} and B_{3u} ring vibrations and the aromatic C-H stretching modes indicates a tilted orientation of both the long and of the short axis of the co-planar viologen moiety with respect to the surface normal. The higher intensities of B_{3u} modes compared to B_{2u} modes suggest a dominant alignment of the viologen moiety along the surface normal [145]. Support for this conclusion is provided by recent results with similar systems. By using electro-reflectance spectroscopy, Sagara et al. concluded that the long axis of the viologen group in monothiol 4V4/$(PF_6^-)_2$ on a polycrystalline Au electrode exhibits an orientation angle of 70º with respect to the surface normal [141].

Based on a combined infrared and near edge X-ray absorption fine structure spectroscopy study, Rong et al. reported tilting and leaning angles of 45º respective 70º for the aromatic moiety in monolayers of ω-(4´-methyl-biphenyl-4-yl)-alkanethiol with an even number of methylene spacer groups on Au(111) [167].

After the transfer from dry to wet conditions, the blue shifts of the B_{3u} mode from 1637 (dry) to 1642 cm^{-1} (wet), and the $\nu_{(Ar\text{-}H)}$ from 3045 (dry) to 3070 cm^{-1} (wet) indicate an increase of π–π interactions between the neighboring bipyridinium rings [168], or a more ordered alignment along the long molecular axis. One reason for the increase of the stacking and of the alignment of the bipyridinium ring planes is the replacement of Br^- by ClO_4^-.

The replacement of Br^- or Cl^- ions by ions with a smaller dynamic hydration sphere, such as ClO_4^- and PF_6^-, was already suggested based on cyclic voltammetric experiments by Buttry [140] and Sagara [141] in self-assembled monolayers of thiol-functionalized viologens. The presence of the hydrophobic perchlorate ions increases the 2D order within the organic film as derived from peak intensities of the B_{3u} modes [141,146]. The lower electron donor ability of ClO_4^- reduces the charge transfer between the viologen moiety and the co-adsorbed anion [160]. Consequently higher π-electron density is kept in the bipyridinium unit [23].

6.3.1.2 C-H stretching modes of alkyl chains

In both Fig. 6-4 and Fig. 6-5, the vibrational bands in 3000 ~ 2800 cm^{-1} can be assigned to the C-H stretching vibrations of the CH_3 asymmetric ($\nu_{a(CH3)}$ at 2960 cm^{-1}), the symmetric ($\nu_{s(CH3)}$ at 2880 cm^{-1}), the CH_2 asymmetric ($\nu_{a(CH2)}$ at 2930 cm^{-1}), and the symmetric ($\nu_{s(CH2)}$ at 2858 cm^{-1}) stretching modes [164,165]. This assignment agrees with the absence of $\nu_{a(CH3)}$ and $\nu_{s(CH3)}$ modes in the spectra of dithiol viologen HS-6V6-SH [151]. The analysis of the intensity ratio of $\nu_{a(CH2)}$ to $\nu_{s(CH2)}$ supports a tilted orientation for the alkyl chains with respect to the normal to the Au(111) surface [169,170]. The tilted angle can be estimated to be approximately 20~30º [141].

The positions of the methylene C-H stretching modes provide a measure of the intermolecular environment of the alkyl chains in the molecular assembly. The peak frequencies of $\nu_{s(CH2)}$ (2858 vs. 2850 cm^{-1}) and $\nu_{a(CH2)}$ (2930 vs. 2920 cm^{-1}) in the

liquid state are typically higher than those for highly ordered crystalline polymethylene chains [169]. The application of Porter's results to the present system leads to the conclusion that the methylene chain environment of the high coverage 6V6 adlayer is liquid-like, i.e. there exists a considerable degree of conformational disorder in the 2D arrangement of the alkyl chains [169].

In Fig. 6-5 of the "wet" SAM, a similar series of C-H stretching modes is observed at slightly higher wavenumbers (2 ~ 4 cm^{-1}, for 6V6) than that for the "dry" adlayer. This is related to the co-adsorption of water molecules and anions.

6.3.1.3 Influence of the alkyl chain length on the V^{2+} SAM structure

The dependence of the V^{2+} SAM structure on the alkyl chain length is in general determined by the lateral interaction (van der Waals interaction) between the neighboring alkyl chains in the SAM.

With increasing number of methylene units, the intensities of the CH_2 and CH_3 stretching modes increase simultaneously, indicating that the orientation of the alkyl chains is almost independent on the chain lengths. Considering the large increase in the magnitude of the absorbance intensity, it is not only in agreement with the slow increase of the surface coverage, but also points to a stronger alignment of the alkyl chains in an all-trans conformation. On the other hand, their frequencies shift to lower values (from 6V6 to 10V10, $\Delta\nu$ = 2 ~ 4 cm^{-1} per $(CH_2)_2$ for dry adlayers and 1 ~ 2 cm^{-1} for wet), showing again an improvement of the lateral order within the assembled viologen SAMs. This is consistent with the higher surface coverage reported for alkanethiols [169], biphenyls [167], or viologen SAMs having longer alkyl chains, as anticipated from CV results in Section 6.2.4.

Both the intensity and the frequency of the B_{3u} ring mode at 1642 cm^{-1} increase with alkyl chain lengths. Referring to similar coverages of 6V6, 8V8, and 10V10, the higher intensities of the B_{3u} bands of 10V10 can be explained by a more tilted orientation of the N-N′ axis, which favors a stronger π–π alignment of the bipyridinium planes and thus results in a blue shift. The long alkyl chains not only increase the alignment of the all-trans hydrocarbon chains, but also stabilize the bipyridinium planes by providing a well-defined non-polar environment, which favors the replacement of Br^- by hydrophobic ClO_4^-.

6.3.1.4 Model of the V^{2+} monolayer

Based on the above qualitative discussion on the structure of viologen adlayers, a schematic model of the V^{2+} SAMs is suggested in Fig. 6-6. The alkyl chains are aligned in an all-trans configuration along the surface normal in a tilted orientation. The long axis of the central bipyridinium rings is also tilted with respect to the surface normal.

The van der Waals interactions between the long alkyl chains leads to two well organized hydrophobic layers, with the redox active bipyridinium V^{2+} aligned in between. The positive charges of the bipyridinium dications are balanced by the negatively charged anions (Br^- under the original "dry" condition and ClO_4^- in electrolyte solution) located close to the nitrogen atoms. The ordered compact stacking of the bipyridinium dications is stabilized by inter-planar π–π and electrostatic coulombic interactions.

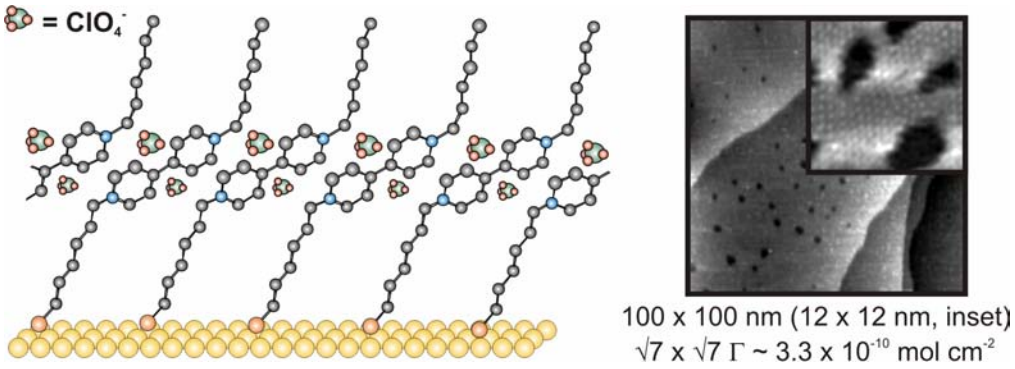

Fig. 6-6: Model of the V^{2+} SAM on a Au surface, and in situ STM image of a 6V6 monothiol adlayer on Au(111) in 0.05 M $KClO_4$, pH = 7, recorded at E_S = -0.60 V (high coverage).

The above model is consistent with results from an EC-STM study of the high coverage 6V6 SAM. The monothiol 6V6 forms an expanded hexagonal monolayer, which covers the entire substrate surface with a (√7 × √7) motif (Fig. 6-6). The resulting coverage amounts to 3.3×10^{-10} mol cm^{-2}, which is in good agreement with the CV data. The open structure is expected due to the bulky size of the tilted viologen moiety, which prevents a (√3 × √3) arrangement, as often observed for high coverage adlayers of alkanethiols on a Au(111) surfaces [171]. In addition, the adlayer is composed of many mono-atomically deep vacancy islands with a typical size of 2 ~ 5 nm in diameter. The defects distort the molecular structure to some extent.

6.3.2 Quasi-steady-state structure of $V^{\bullet+}$

6.3.2.1 Quasi-steady-state SEIRA spectra

As shown in Fig. 6-1, the excursion of the electrode potential from E = -0.60 V to E = -1.10 V triggers the one-electron reduction of $V^{2+} \leftrightarrow V^{\bullet+}$, which is reversible upon cycling the potential with a scan rate $\geq$ 50 mV s^{-1}. Radical monocations ($V^{\bullet+}$) can also be stabilized by holding the substrate potential at -1.10 V. However, a stationary potential control at -1.10 V should be avoided because the reversibility may decrease due to an "aging" effect induced by re-alignment of solvent molecules [129,146] or the formation of insoluble salts [142]. Therefore we focus on the quasi-steady-state SEIRAS spectra of $V^{\bullet+}$ measured in a potential cycle, with a reference spectrum acquired at -0.60 V, where a stable V^{2+} adlayer exists. The potential different SEIRAS shows the difference in the structure of $V^{\bullet+}$ compared to V^{2+}.

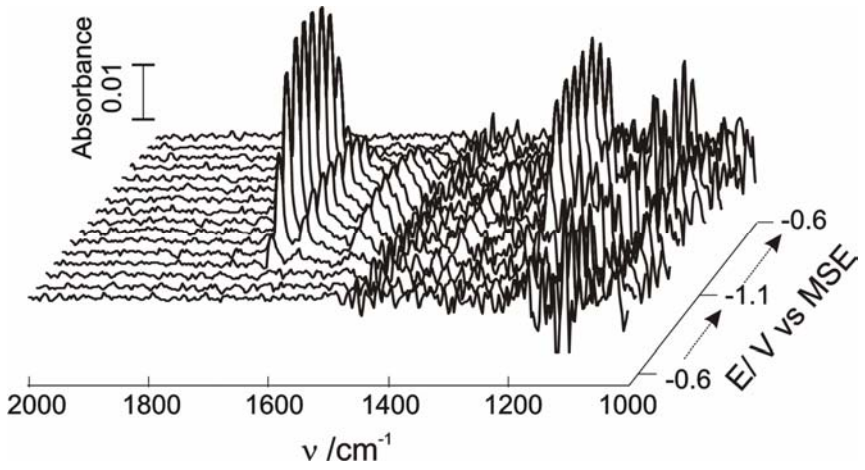

Fig. 6-7: 3D potential-dynamic SEIRA spectra of a 6V6 monothiol SAM on a Au(111-25 nm) film electrode. The spectra were recorded in the "slow scan" mode during a potential cycle at 50 mV s^{-1}. The background spectrum was measured at E = -0.600 V. Each potential-difference spectra is the average of 80 single beam spectrums.

A 3D representation of the slow scan SEIRA spectra of a 6V6 adlayer on a Au(111-25 nm) film electrode is shown in Fig. 6-7. The reversible evolution of the IR bands in the range of the ring vibrations agrees well with the CV results of the $V^{2+} \leftrightarrow V^{\bullet+}$ redox reaction. The spectrum recorded at -0.94 V, which represents a quasi-steady-state response of the reduced $V^{\bullet+}$ form, was selected and presented in Fig. 6-8 together with the potential difference spectra of 8V8 and 10V10 recorded in the same way at -0.94 V.

Only small changes appear in the spectra ranges of the $\nu_{(C-H)}$ and $\nu_{(O-H)}$ stretching modes (not show), illustrating rather similar structures of the alkyl chains in two redox states, and very little reorganization in the structure and amount of interfacial water, respectively. The latter is consistent with the previous expectation of a hydrophobic, compact monolayer characterized by strong van der Waals interactions between alkyl chains.

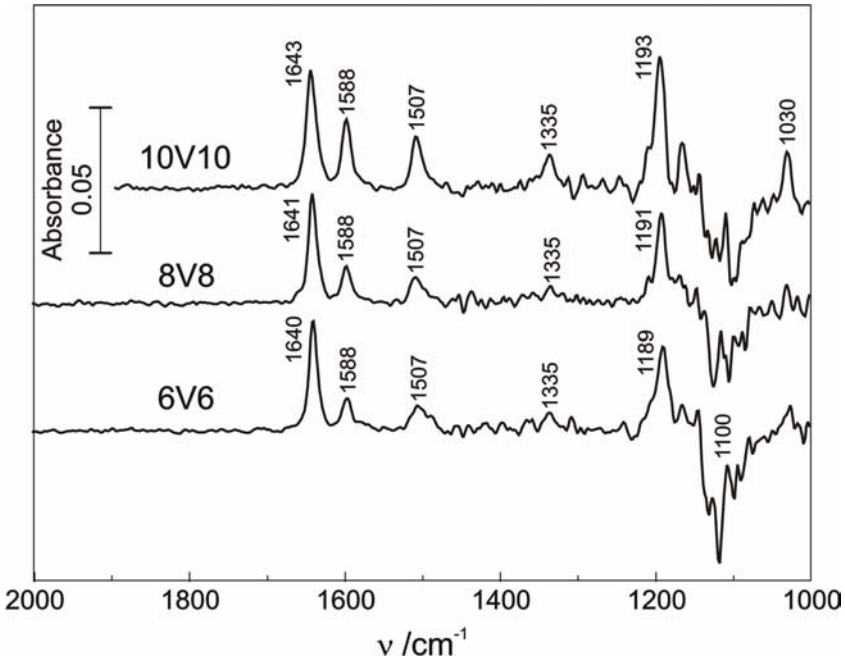

Fig. 6-8: In situ SEIRA spectra of the radical cations ($V^{\bullet+}$) of 6V6, 8V8, and 10V10 monothiol SAMs recorded at -0.940 V during a slow potential scan from -0.600 V to -1.100 V, scan rate 50 mV s^{-1}. The reference spectrum was measured at E = -0.600 V. Each potential difference spectra is the average of 80 single spectrums.

Compared with the high wavenumber range, several positive bands around 1640, 1588, 1507, 1335, 1189, 1030 cm^{-1} and a negative one around 1100 cm^{-1} appear at 1000~1700 cm^{-1}. They are related to the ring vibrational modes of $V^{\bullet+}$ and the symmetric $\nu_{(Cl-O)}$ mode of ClO_4^-, respectively. The presence of such pronounced vibrational bands in the potential different spectra indicates considerable structure changes in the redox center upon the redox reaction.

The prominent bands at 1640 and 1189 cm^{-1} can be assigned to the asymmetric in plane ring-vibrations of the monomer radical cation $V^{\bullet+}$. Specific coordination analysis shows that they have the same origin as V^{2+}: the two B_{3u} modes in a D_{2h} symmetry have main contributions from the push-pull movements of C-C (1640 cm^{-1})

and N-R (1189 cm^{-1}) bonds [146,164]. Their high intensities can be explained by the enhanced dipole changes originating from the oscillation of the delocalized radical electron between the two pyridine rings, which is parallel to the long molecular axis in N-N′ direction. Such oscillation of the delocalized radical electrons suggests an extended aromatic moiety across both rings, which may partially contribute to the enhancement of the ET through the whole redox center. For example, we notice that STM experiments on single-molecular junction (Au_{tip}-S-6V6-S-$Au_{substrate}$) reveal a 50% higher conductance for the $V^{\bullet+}$ state in comparison to V^{2+} [151].

The other modes (1588, 1507, 1335 and 1030 cm^{-1}) are attributed to "charge-transfer activated", totally symmetric (A_g) ring vibrations of the radical cation dimer $(V^{\bullet+})_2$. The activation of these inherent A_g modes involves a "vibronic coupling" mechanism in a one-dimensional charge transfer complex: when two radical $V^{\bullet+}$ planes are linked face-to-face via π-bonding, their individual A_g modes are coupled out-of-phase and activated by a charge polarization, which is induced by the charge-transfer between the two bipyridine units [163]. The dipole transitions involved in these dimer vibrational modes are normal to the $V^{\bullet+}$ planes.

The $(V^{\bullet+})_2$ dimer is usually more stable than the monomer because the π–π stacking interactions between radical planes are stronger than the electrostatic attractions between the radical cation and the attached anions [146]. In spite of the higher stability of the $(V^{\bullet+})_2$ dimer, the radical cation monomer is stabilized by electrostatic attraction to co-adsorbed ClO_4^- anions in a hydrophobic environment [140,141,143], as well as by the commensurability matching of intra-assembly planes [19,172]. Consequently, monomers and dimers of $V^{\bullet+}$ radical cations coexist in the reduced 6V6 monolayer.

The broad negative-going band around 1100 cm^{-1} indicates the release of ClO_4^- upon the reduction $V^{2+} \leftrightarrow V^{\bullet+}$, which is supported by previous EQCM results [150]. Due to the less hydrated shell of ClO_4^- and the hydrophobic alkyl chain environment, the anion migration involves very small amounts of solvent molecules (H_2O). This phenomenon is reflected in the absence of a $\nu_{(O-H)}$ feature related to interfacial water species in the potential different spectra between V^{2+} and $V^{\bullet+}$

6.3.2.2 Alkyl chain length dependence of $V^{\bullet+}$

The lateral interactions can be further addressed by exploring the alkyl chain length dependence of the $V^{\bullet+}$ spectra. Fig. 6-8 shows selected SEIRAS spectra of 6V6, 8V8, and 10V10 measured at -1.0 V. The reference potential was -0.60 V.

The ring-vibrational modes of the monomers shift to higher wavenumbers with the increase of the chain length (from 1640, 1189 to 1643, 1193 cm^{-1}, respectively). It indicates a stronger inter-plane π–π interaction between the $V^{\bullet+}$ units, which is stabilized by the van der Waals interaction within the bulky alignment of the alkyl chains. A similar mechanism has been proposed to explain the blue shift of the B_{2u} vibrational band of V^{2+} at 1642 cm^{-1}. However, the ring vibrational bands of the dimer $(V^{\bullet+})_2$ do not shift, indicating the vibronic coupling intensity is relatively independent on the aliphatic environment. Such different trends of the chain length dependence suggest that the coupling between two sub-units of a dimer is stronger than the electrostatic π–π interaction between neighboring monomeric $V^{\bullet+}$ radicals [143,146].

Taking the intensity of the strongest monomer vibration around 1640 cm^{-1} as an internal standard, a more tilted orientation of the longer alkyl chains is suggested by the increased intensity of the N-R/N′-R dominated vibrational band around 1189 cm^{-1}. The relative intensities of the dimer modes at 1596, 1507 cm^{-1}, with respect to that at 1640 cm^{-1}, increase with the alkyl chain lengths, indicating an increased preference of the dimerization according to 6V6 < 8V8 < 10V10. Similar to the π–π stacking between V^{2+} planes, the dimerization is also favored by more tilted bipyridinium units connected with the longer alkyl chains.

6.3.2.3 Model of the $V^{\bullet+}$ monolayer

Based on the above qualitative discussion, different schematic models of the $V^{\bullet+}$ adlayers were developed in Fig. 6-9. The van der Waals interaction between long alkyl chains results in two well aligned hydrophobic “sub-layers”, with the redox active bipyridinium $V^{\bullet+}$ layer enclosed. Both the monomers and the dimers of $V^{\bullet+}$ co-exist in such a sandwich model. The alignment of radical cations is stabilized by both the π–π stacking between monomers and the strong vibronic coupling within the dimers. The dimerization and the alignment are favored by a more tilted bipyridinium units. Both increase with the lengths of the alkyl chains.

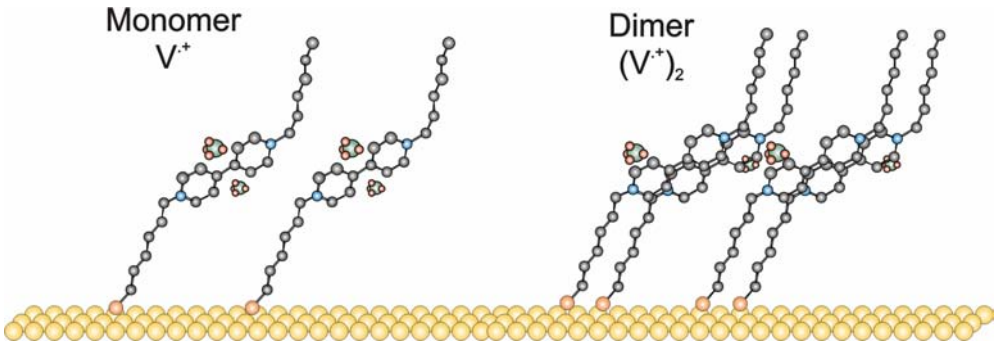

Fig. 6-9: Models of the co-existing monomer/dimer of radical cations in the 6V6 monothiol SAM.

6.4 Kinetics of the 1st Redox Process

The above discussion on the steady-state structures of V^{2+} and $V^{\bullet+}$ monolayers indicates differences between the two redox forms. These structure differences reveal the fundamental mechanism for related phenomena on molecular conductivity and molecular switching [151]. To improve our understanding of the nature of these transition processes, a spectroelectrochemical kinetic study was carried out.

6.4.1 CV scan rate dependence

The fast ET kinetics and the chemical reactions associated with the ET can be analyzed with CV measurements at high scan rates of the potential [12, 173]. As discussed in Section 6.2, the peak separation of the anodic/cathodic traces is constant up to 2 V s^{-1}, indicating the complexity in a rather fast ET process. To reduce the interference of the electrolyte resistance and the interfacial capacitance on the electrode reaction [173, 174], we combined EC studies with macroscopic single crystal electrodes with experiments employing microelectrodes (∅ ~ μm) and nanoelectrodes (∅ < 1 μm).

Fig. 6-10A shows the CV of a 6V6 self-assembled monolayer on an Au microdisc electrode (∅ = 10 μm) recorded in –1.10 V < E < -0.55 V ($V^{2+} \leftrightarrow V^{\bullet+}$) at scan rates ranging between 0.02 and 10 V s^{-1}. Well-defined reversible redox peaks are observed at all scan rates, showing a similar electrochemical response to that of a macro-size Au(111) single crystal or film electrode. The coverage of 6V6 can be estimated to 2.70×10^{-10} mol cm^{-2}, which is slightly lower than that on Au(111). This

is partially attributed to the non-homogeneous polycrystalline surface of the microelectrode.

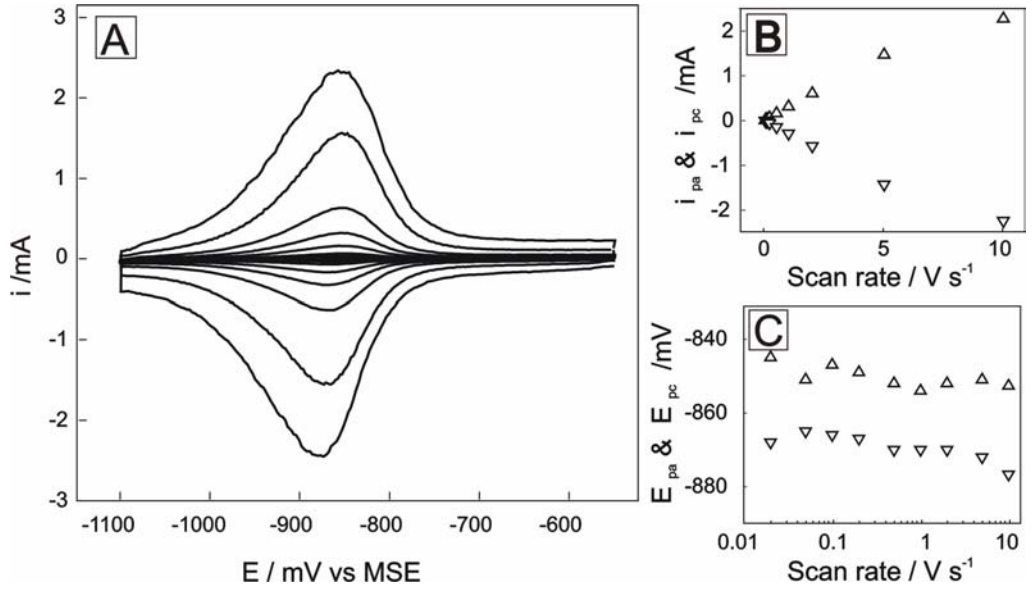

Fig. 6-10: (A) CVs of the 1st ET process for a 6V6 SAM on a gold polycrystalline microelectrode (Ø = 10 μm) in 0.05 M $KClO_4$, pH ~ 10. The scan rates range from 20 mV s^{-1} to 10 V s^{-1}; (B, C) Scan rate dependencies of the peak currents j_{pa}/j_{pc} and the peak potentials E_{pa}/E_{pc}, respectively. The anodic and cathodic scan directions are labeled as (△) and (▽), respectively.

The detailed scan rate dependencies of the CV parameters are plotted in Fig. 6-10B, C. The plots show that the peak current values of the anodic and of the cathodic sweeps scale linearly with the scan rates. The peak potential separation is constant at 19 mV within the experimental range of scan rate. These results support again a reversible one-electron redox process, in which the redox species are immobilized on the substrate surface.

The ΔE_p suggests a kinetic complexity, e.g. the formation of ion-pairs as mentioned in Section 6.2. However, the absence of a further increase of ΔE_p, even at the maximum scan rate (10 V s^{-1}) of our home made potentiostat, shows that the inherent time window of the heterogeneous electron-transfer is shorter than several milliseconds [12], which is outside the detectable time-window of our current EC equipment. We can only give an estimation of the minimum limit of the ET rate constant as k_o (at $E_{P1/P1'}$) > 150 s^{-1} [151].

6.4.2 Current transient measurements

Compared with the microelectrode, the influence from the Ohm drop has to be carefully considered in measurements with macroscopic (∅ > 1 mm) Au electrodes. Although the IR-compensation has been enabled during the chronoamperometry experiments of 6V6/Au(111-25 nm) film electrodes (working area: 1.53 cm^2), the potential of the WE still cannot exactly follow the applied potential step within the transient time scale. An estimation from the current and solution resistance shows that the actual potential jump reaches the correct level after a rather short time delay (initially 0~15 ms). Thus the subsequent current transients (after 15 ms) can be considered as reliable responses of the slow changes in the $V^{\bullet+}$ SAM.

Fig. 6-11 shows the current transients of the Au(111-25 nm) film electrodes modified with 6V6, 8V8, and 10V10 (solid lines), recorded after a potential step from -0.6 V (V^{2+}) to -0.87 V ($V^{\bullet+}$). As a control experiment, they are further compared with the data from a bare Au film electrode (dotted line) in the same electrolyte solution. Each transient includes an initial fast charging process (0 ~ 15 ms), and a subsequent slower one in the long time range (> 15 ms). One shall notice their dependence on the alkyl chain lengths, and the absence of slower process in the single-exponential transient on the bare Au surface. Therefore, the long-time transients clearly contain contributions of the viologen SAMs.

The initial heterogeneous ET from the electrode to the V^{2+} moiety can be considered as fast elastic electron-tunneling along the alkyl chains [175]. Therefore, the initial fast process includes the reductive ET, together with the fast double layer charging, as suggested by the fast CV measurements in a short time window of milliseconds. The slow transient may involve overlapping contributions like migration of cations or anions through the interface, as well as the reorganization of the adlayer structure upon ET. Similar slow current transients have been also observed on viologen-modified Au(111) single crystals and Au microelectrodes.

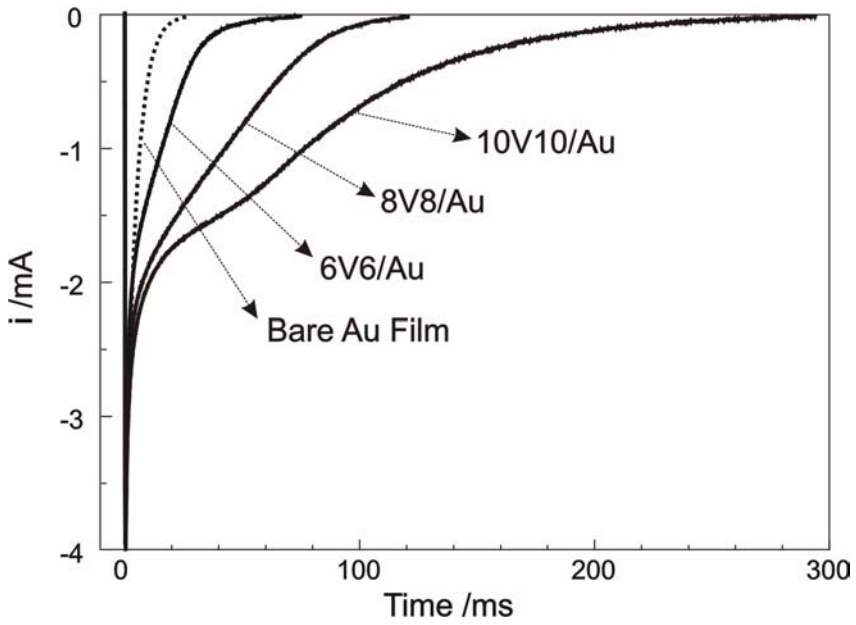

Fig. 6-11: Current transients obtained on a Au(111-25 nm) film electrode recorded simultaneously with time-resolved SEIRA spectra, after a potential step from E_i = -0.60 V (t_w = 0.20 s) to E_f = -0.90 V in the step-scan regime. Dotted line: bare Au(111-25 nm) film electrode in 0.05 M $KClO_4$ supporting electrolyte; Solid lines: Au film electrodes modified with 6V6, 8V8, and 10V10 monothiol viologen adlayers.

As discussed in the analysis of the steady-state SEIRAS and of the CV scan rate dependencies, the structure and chemical composition of the redox centers are different for the reactant (V^{2+}) and the product ($V^{\bullet+}$). Structure or chemical changes, such as the delocalization of radical electrons and the migration of ClO_4^-, play important roles for the rate-determining steps. To decouple the overlapping contributions from the slow part of the chronoamperometric transients, time resolved in situ SEIRAS was applied in the step scan mode.

6.4.3 Time-resolved in situ SEIRAS

Fig. 6-12 shows a 3D time resolved SEIRA spectra after a potential step from -0.6 V to -1.0 V, which triggered the reduction from V^{2+} to $V^{\bullet+}$. The development of the vibration bands at 1638, 1593, 1500, 1193 and 1120 cm^{-1} indicates the formation of the $V^{\bullet+}$ monomer/dimer, and the migration of ClO_4^- anions out of the adlayer to balance the negative charge. These observations are in accordance with qualitative conclusions derived from the voltammetry results and the tentative suggestions from chronoamperometric studies.

Fig. 6-13A shows the detailed plots of the time dependencies of the intensities of the vibration bands at 1638, 1593, 1500 and 1120 cm^{-1}. Within the initial range of 15 ms, no spectroscopic changes are observed. Even with IR-compensation, the initial transient is still somewhat distorted by the Ohmic potential drop due to a rather high charging current caused by the area of the Au film electrode. Therefore, our discussion will be focused on the slow follow-up processes (> 15 ms). The intensities of all positive-going ring vibrational bands and of the negative-going ClO_4^- band increase simultaneously in a time scale of 80 ms for 6V6, indicating the formation of $V^{\bullet+}$ monomers/dimers, and the migration of ClO_4^- anions.

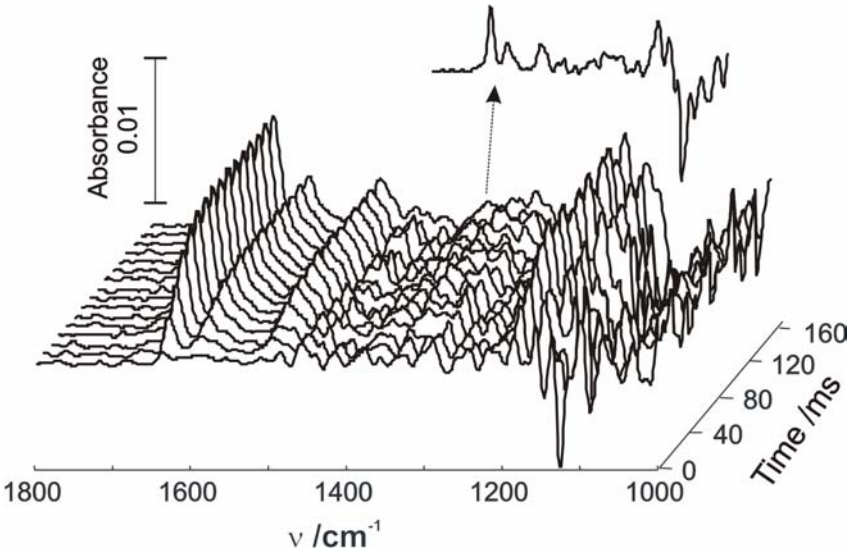

Fig. 6-12: Series of time-resolved SEIRA spectra for the 1st reduction process $V^{2+} \leftrightarrow V^{\bullet+}$ on Au(111-25 nm) in 0.05 M $KClO_4$ at pH~7 after a single potential step from E_i = -0.60 V (t_w = 0.20 s) to E_f = -0.90 V as measured in the step-scan regime. The reference spectrum was obtained at E_i = -0.60 V. Each spectrum plotted represents the average of 200 single spectra. The displayed time resolution was 10 ms. For reason of clarity, the inset shows only one typical single beam spectrum in 1000 $cm^{-1} < \nu < 1800$ cm^{-1}.

Fig. 6-13B and C show the plots of the time-dependent evolution of the vibrational frequency (band positions) and the FWHM of the IR bands are shown in. The monomer band around 1638 cm^{-1} shifts to higher wavenumbers (> 8 cm^{-1}), while the dimer bands at 1593, 1500 cm^{-1} shift with a somewhat smaller frequency value (< 5 cm^{-1}). Such differences indicate an increase in the π-stacking between monomers, whereas the much stronger vibronic coupling within a dimer structure is less influenced by the temporal evolution. The FWHM of the monomer $V^{\bullet+}$ related band at 1638 cm^{-1} increases with time, and reaches a constant value around 60 ms. While the

dimer related bands at 1593, 1500 cm^{-1} show a decreasing FWHM with time. The FWHM values are usually used to estimate the order of a created structure. Such opposite trends in the evolution of FWHM vs. time indicate that the dimers are formed from a network of monomers.

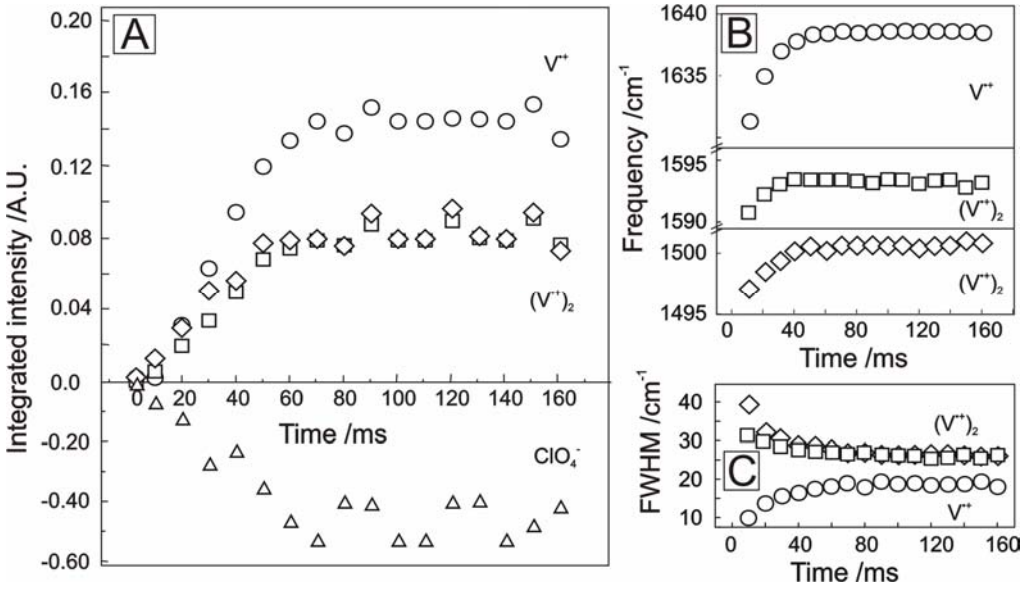

Fig. 6-13: Time dependencies of the intensities (A), the peak positions (B), and the FWHM (C) of the monomer $V^{\bullet+}$ (○, 1638 cm^{-1}), the dimer $V^{\bullet+}$ (□, 1593 and ◇, 1500 cm^{-1}), and the ClO_4^- (△, 1120 cm^{-1}) vibrational bands as obtained from the data plotted in Fig. 6-12.

The net charge flow across the electrode-film interface requires a simultaneous flow of ions across both the film and the film/solution interface. Thus, during the reduction of the redox species, cations of the supporting electrolyte have to migrate into the electrode film, and/or anions initially present in the film have to migrate out of the film in order to maintain electroneutrality [176].

As confirmed by SEIRAS and chronoamperometry, the ClO_4^- migration, the movement of solvent molecules, and the formation of $V^{\bullet+}/(V^{\bullet+})_2$ are all much slower than the double layer charging and the reductive ET. These slow processes may contribute as rate-determining steps to the overall redox process [175,176]. Such an expectation is partially supported by the two-step continuous tunneling mechanism anticipated from the study of asymmetric 6V6 junctions formed between a STM tip and a Au(111) electrode [151]. To explore further details of these complex mechanisms, systematic investigations on counterion concentration and positional changes of the redox centers within the film are essential. Referring to the steady-state

approach in Section 6.2 and 6.3, we carried out exploring experiments with viologens having a different length of the alkyl chains.

6.4.4 Alkyl chain length dependence

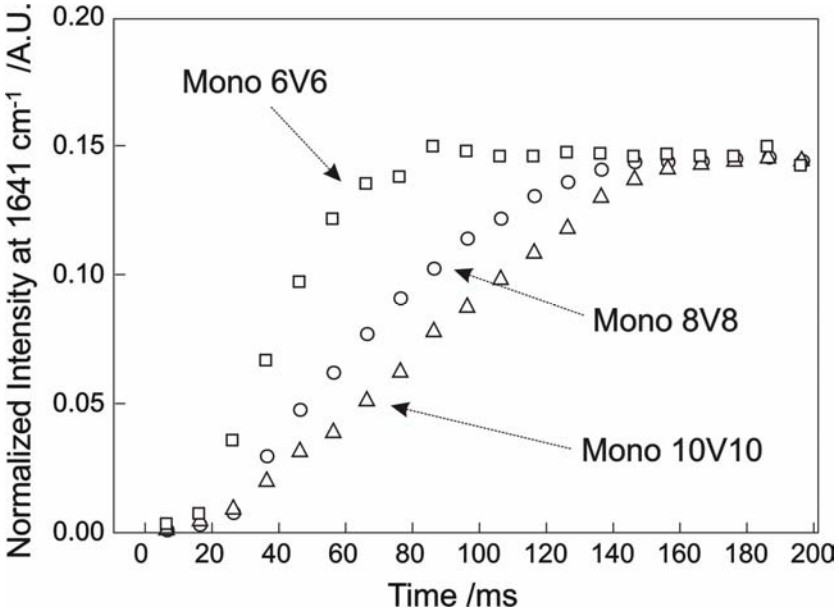

Fig. 6-14: Time dependencies of the ring vibrational intensities of Au(111-25 nm) film electrodes modified with 6V6 (□), 8V8 (○), and 10V10 (△) recorded in step scan measurements. The potential step parameters were the same as those in Fig. 6-11 and 6-12. Only the strongest ring-vibrational bands around 1640 cm^{-1} (Monomeric radical cation) were plotted and normalized with 6V6 as internal standard.

The time resolved SEIRAS of Au film electrodes modified with 8V8 and 10V10 are shown in Fig. 6-14 and are compared with the IR transient of 6V6. For reasons of clarity, only the strongest ring-vibrational bands around 1640 cm^{-1} (monomeric radical cation) were plotted. The data were normalized to the 6V6 modes as an internal standard. All SEIRAS transients have the same trends in the slow process: an increase of the intensities of the $V^{\bullet+}/(V^{\bullet+})_2$ ring vibrational modes and a migration of ClO_4^- away from the interface. The transient time of the slow process becomes longer with increasing length of the alkyl chains in the following sequence: 6V6 < 8V8 < 10V10. The slower migration of ClO_4^- is attributed to the longer penetrating distance across the thicker alkyl chain layer. Alternatively, a strong interaction between the anions and the V^{2+} may also contribute in a hydrophobic environment.

Considering the chain length dependence of the steady-state $V^{\bullet+}/(V^{\bullet+})_2$ structure, the hydrophobic radical cations are more favored by the alignment of the longer alkyl chains. Such a hydrophobic preference to the reduced $V^{\bullet+}$ should have led to a shorter transient time for longer alkyl chains. However, an opposite trend was observed. This trend supports the tentative conclusion, that the overall rate of the redox process is mostly determined by the migration of ClO_4^- anions, and the subsequent molecular reorganization as the slowest steps. Both reductive ET and radical cation formation can be hindered electrostatically or structurally by such a slow anion movement. This is in agreement with the anticipated formation of an ion-pair complex of V^{2+}-$2ClO_4^-$ or $V^{\bullet+}$-ClO_4^- [140].

On the other hand, the SEIRAS transient of 6V6 shows a Langmuir-type kinetic behavior, while the transient of 10V10 shows significant deviation. This indicates the role of stronger lateral interactions in the SAM of viologen with longer alkyl chains.

Because the Ohmic distortion in the initial part of the experimental transients cannot be completely neglected in our spectroelectrochemical cell, we hesitate to fit SEIRAS and EC transients into quantitative theoretical models. However, we propose the following tentative conclusions: i) the overall redox processes start from a fast interfacial ET tunneling from the electrode to the V^{2+} moiety through the alkyl chains. The rate of the ET process is out of the detection range of our current equipments; ii) several follow-up, slower processes, such as dimerization, radical electron delocalization, and ClO_4^- migration take place simultaneously; iii) the overall rate of the redox reaction is determined by the dissociation of possible ion-pairs and the migration of ClO_4^- anions.

6.5 Summary

Self-assembled monolayers of viologen 6V6, 8V8, and 10V10 have been characterized by using cyclic voltammetry, chronoamperometry, and in situ SEIRAS. The electrochemical studies show that the 1^{st} redox process $V^{2+} \leftrightarrow V^{\bullet+}$ is reversible, while the 2^{nd} redox process $V^{\bullet+} \leftrightarrow V^0$ is only quasi reversible. Investigations of steady-state structures were focused on the V^{2+} and $V^{\bullet+}$ redox states. Time-resolved SEIRAS was also employed to explore the kinetics of electron-transfer process $V^{2+} \rightarrow$

$V^{\bullet+}$. The results have been discussed together with EC-STM and STS, and are correlated to molecular junction experiments with single viologen bridges.

The SAM of V^{2+} exhibits a sandwich-like structure: the van der Waals interaction between alkyl chains leads to two well ordered hydrophobic layers, with the redox active bipyridinium V^{2+} layer enclosed in between. The alkyl chains are aligned in an all-trans configuration in a tilted orientation with respect to the surface normal, with some extent of conformation disorder. The long axis of the central bipyridinium rings are also tilted with respect to the surface normal. The positive charge of the bipyridinium dications is balanced by the negatively charged anions (Br^- in original "dry" condition and ClO_4^- in electrolyte solution) located close to the N atoms. The alignment of V^{2+} is stabilized by inter-planar π–π interaction and electrostatic coulombic interactions.

In the SAM of $V^{\bullet+}$, monomer and dimer of $V^{\bullet+}$ co-exist in a similar sandwich structure. The alignment of the radical cations is stabilized by the strong vibronic coupling within the dimers and the π–π stacking between the monomers. The dimerization and the alignment are both favored by the more tilted bipyridinium units with an increase of alkyl chain lengths.

Attempts to investigate the kinetic behavior of the redox electron-transfer process $V^{2+} \rightarrow V^{\bullet+}$ lead to qualitative conclusions. The overall redox process starts with an interfacial ET tunneling from the electrode to the V^{2+} moiety through the alkyl chains. In a subsequent slow process, the dimerization of $V^{\bullet+}$, the delocalization of the radical electrons, and the migration of ClO_4^- take place simultaneously. The overall rate of the redox reaction is determined by the dissociation of the ion-pair complex and the migration of the ClO_4^- anions.

Chapter 7. Conclusions

As a powerful molecule / ion-specific probe, ATR-SEIRAS has been employed together with electrochemistry and in situ STM to explore the interfacial structure and chemical properties under steady-state or dynamic conditions. This dissertation is focused on the two self-assembled systems: TMA adlayer, and viologen SAM on Au/electrolyte interfaces.

In the first part, the adsorption and phase formation of TMA on Au(111-25 nm) film electrodes were comprehensively characterized by EC, STM, and SEIRAS. Depending on the applied electrode potential, TMA molecules were observed with different 2D ordered structures: two physisorbed adlayers with a hexagonal honeycomb pattern and a close packing of linear-dimers of planar oriented molecules, one stripe-like chemisorbed adlayer of perpendicularly oriented molecules. Weakly hydrogen-bonded, strongly hydrogen-bonded, and isolated water species are co-adsorbed. The potential-induced formation of chemisorbed TMA starts from a fast change of orientation from a planar physisorbed phase to a disordered chemisorbed phase with tilted and/or perpendicular molecules. Subsequently, the chemisorbed TMA molecules align slowly into the highly ordered, stripe-like adlayer. Both substrate/adsorbate and intermolecular hydrogen-bonding interactions are strongly dependent on the electrode potential.

A comparison with BA and IA shows that each TMA molecule is chemisorbed via one carboxylate group in the “atop” model leaving the two -COOH side groups available for further hydrogen-bonding between neighboring TMA molecules. The orientation of BA and IA molecules in the respective adlayers shows a similar potential dependence as for TMA.

The second topic of this dissertation is focused on the SAMs of viologens immobilized on Au substrate via Au-S bonds. The electrochemistry shows that the 1st redox process $V^{2+} \leftrightarrow V^{\bullet+}$ is reversible, while the 2nd redox process $V^{\bullet+} \leftrightarrow V^{0}$ is only quasi reversible. The SAM of V^{2+} exhibits a sandwich-like structure: the van der

Waals interaction between alkyl chains leads to two well ordered hydrophobic layers, with the redox active bipyridinium V^{2+} layer enclosed in between. The alkyl chains are aligned in an all-trans configuration in a tilted orientation with respect to the surface normal. The long axis of the central bipyridinium rings is also tilted. The alignment of V^{2+} is stabilized by van der Waals interaction between alkyl chains, inter-planar π–π stacking, and electrostatic coulombic interaction. In the SAM of $V^{\bullet+}$, both monomer and dimer of $V^{\bullet+}$ co-exist. The alignment of the $V^{\bullet+}$ is further stabilized by the strong vibronic coupling within the dimers. The dimerization and the alignment are both favored by the more tilted bipyridinium units with an increase in alkyl chain length.

Attempts to investigate the kinetic behavior of the redox electron-transfer process $V^{2+} \rightarrow V^{\bullet+}$ lead to qualitative conclusions. The overall redox process starts with an interfacial electron transfer tunneling from the electrode to the V^{2+} moiety through the alkyl chains. In a subsequent slow process, the dimerization of $V^{\bullet+}$, the delocalization of the radical electrons, and the migration of ClO_4^- take place simultaneously. The overall rate of the redox reaction is determined by the dissociation of the ion-pair complex and the migration of the ClO_4^- anions.

ATR-SEIRAS has been proved to be a powerful tool to explore the molecular structure and chemical properties of interfacial species. The results from SEIRAS characterization are complementary to those from EC and STM studies. The combination of in situ SEIRAS and other characterization methods provides comprehensive understandings of the structures and functionalities of various 2D self-assembled supramolecular systems on electrode/electrolyte interfaces. It will help to explain the mechanisms of certain molecular electronics, and to design the novel nanoscale devices based on an electrochemical operation.

Self-assembly is happening in all scales, isn't it?

A. List of Figures, Schemes, and Tables

List of Figures

List of Schemes and Tables

B. List of Symbols and Abbreviations

2D	two dimension(al)
3D	three dimension(al)
A	electrode area
	absorbance
AES	Auger electron spectroscopy
AFM	atomic force microscopy
a_{Ox} / a_{Red}	activity of the oxidized (reduced) species
ATR	attenuated total reflection
BA	benzoic acid
BMS	half-beamsplitter
c_A	bulk concentration of species A in solution
CE	counter electrode
C_{Ox} / C_{Red}	concentration of the reduced (oxidized) species
CV	cyclic voltammogram, cyclic voltammetry
D_{Ox}	diffusion coefficient of the reduced species
d_p	penetration depth of an evanescent wave
DSC	differential scanned calorimetry
DTA	differential thermo analysis
E	evanescent wave
EC	electrochemical, electrochemistry
EDL	electrochemical double layer
E_f	final potential of a potential step
E_i	initially pre-conditioned potential of a potential step
E_m	potential drop in the monolayer part,
E_{pa} / E_{pc}	anodic/cathodic peak potentials
E_r	reference potential
E_s	potential drop in solution part
	electrode potential swept to a different value of interest
ET	electron-transfer
EXAFS	extended X-ray absorption fine structure
E_λ	switching potential after passing the redox peak
F	the Faraday constant, charge on one mole of electrons
FT-IR	Fourier Transform Infrared spectroscopy
FWHM	full width at half maximum
g	interaction parameter in adsorption isotherms ($g=\gamma/RT$)
G_A	molar Gibbs free energy of species A in solution
G_{ad}	molar Gibbs free energy of the adsorbate
HOMO	highest occupied molecular orbital
HOPG	highly oriented pyrolytic graphite
HREEL	high resolution electron energy loss
IBN	Institute of Bio- and Nano-Systems
I(δ)	interferogram
I(ν)	single beam spectrum

i_0	exchange current
i_a	anodic current
IA	isophthalic acid
i_c	cathodic current
IHP	inner Helmholtz plane
INS	inelastic neutron scattering
i_{pa} / i_{pc}	anodic/cathodic peak current
IRE	internal reflectance element
IRRAS	infrared reflection absorption spectroscopy
K_a	acid dissociation coefficient
k_b	heterogeneous rate constant of the backward reaction
k_{ET}	electron-transfer rate coefficient
k_f	heterogeneous rate constant of the forward reaction
LB	Langmuir-Blodgett
LEED	low energy electron diffraction
LSV	linear sweep voltammetry
LUMO	lowest unoccupied molecular orbital
MIR	Multiple internal reflection
MSE	mercury sulphate electrode
n	refractive index
NHE	normal hydrogen electrode
OHP	outer Helmholtz plane
Ox	the oxidized partner of a redox couple
PZC	potential of zero charge
Q	charge transfer
Q_{ads}	redox charge transfer of the adsorbed species
QCM/EQCM	(electrochemical) quartz crystal microbalance
Q_d	diffusional charge transfer transient
Q_{dl}	double layer charging charge transfer
Q_t	total charge transfer
RE	reference electrode
Red	the reduced partner of a redox couple
RHE	real hydrogen electrode
S/N	signal-to-noise ratio
SAM	self-assembled monolayer
SCE	saturated calomel electrode
SEIRA/SEIRAS	surface enhanced infrared absorption (spectroscopy)
SHG/SFG	second harmonic generation / second frequency generation
SIMS	surface ion mobility spectrometry/mass spectrometry
SNIFTIRS	subtractively normalized interfacial FT-TR spectroscopy
SPM	scanning probe microscopy
SPR	surface plasmon resonance
S_r	reference spectrum
S_s	spectra at a potential value of interest
STM	scanning tunneling microscopy
T	temperature
t	time
TA	terephthalic acid
THE	trapped hydrogen electrode
TMA	trimesic acid

TOC	total organic content
UHV	ultra high vacuum
UPD	under-potential deposition
UV-vis	ultraviolet-visible
v	potential scan rate
$V^{\bullet+}$	viologen radical monocation
V^{0}	neutral form of viologen
V^{2+}	viologen dication
WE	working electrode
XANES	X-ray absorption near-edge structure
XPS	X-ray photoelectron spectroscopy
η	over potential
θ	angle of incidence,
ΔE_p	voltage separation of anodic and cathodic current peaks
$\Delta E_{p,1/2}$	total width at half-height of current peaks
ΔG_{ad}	Gibbs free energy change in an adsorption process
ΔG_{ad}^{0}	standard Gibbs free energy change in an adsorption process
Γ_{Ox}^{*}	surface excess of the adsorbed reduced species
α	transfer coefficient of an electron transfer reaction
δ	optical retardation
	bending vibration mode
ϕ	electrode potential
ϕ_2	potentials in OHP
ϕ^{M}	potentials in metal electrode
ϕ^{S}	potentials in bulk electrolyte
$\varnothing$	diameter
γ	interaction parameter in adsorption isotherms
λ	reorganization free energy
	wave length
λ_0	solvation contributions in reorganization free energy
λ_i	vibrational contributions in reorganization free energy
ν	stretching vibration mode
θ	surface coverage
θ_c	critical reflection angle

C. Acknowledgements

This achievement could have been a “mission impossible” without the help and support from my colleagues, my family, and my friends through years. At the risk of missing someone, I wish to keep the following names on the short pages here.

First and foremost, I must thank my thesis advisor, Dr. Thomas Wandlowski for his help, guidance, and many useful discussions on numerous topics. His broad vision on the frontiers of electrochemistry, as well as his extremely careful insight into every experimental detail, has always inspired me to go deeper and further in my scientific career. He is so patient that I can reach him with questions almost anytime in the next door. He showed me the first single crystal measurement personally. I had the pleasure of being his first PhD student in Jülich. Besides, Thomas is also one of the most trusted friends of mine. We share the joys in both science and daily lives. I will never forget the beautiful mountains where we were hiking in his hometown in Saxon Switzerland.

I need to acknowledge Prof. Ulrich Simon in RWTH-Aachen University, for his kind offer to be the referee of my dissertation, and inviting me to present my work in his institute. The valuable discussions and suggestions will add great importance to the last revision of my dissertation. Prof. Walter Richtering and Prof. Heiko Lueken are also appreciated for presenting as the 3rd examinator and chairman in my oral examination, respectively.

During my stay in Jülich, I have been excited to watch the development of our group from the early days to the present. I thank everyone in our electrochemical group, past and present, for their help and enjoyable cooperation. I will keep in my “non-erasable” memory all the stories with names: Sergey Pronkin, Gabor Nagy, Zhihai Li, Ilya Pobelov, Gabor Meszaros, Masanori Hara, Antonio Berná, Rocio Aguilar-Sanchez, Guijin Su, Renata Butja, Il-cheol Jeon, Chen Li, Karolina Caban, Zhengyan Wu, Stijn Mertens, and Alexander Putz.

In such a worldwide team, Sergey is especially appreciated not only for his help and teaching me many lab skills when I first started, but also for the proof reading. He showed me the price of good H_2SO_4 spectra in a clean measurement: 2 or 3 beautifully etched holes by acid in our lab-coats every time. He is also the first guy who reminded me how to be a strong “physical” chemist as he is.

Zhihai is my best partner in my PhD work. Thank him for sharing all the nice STM images with me. It was a nice experience with Zhihai to help each other, to share our feelings and ideas, even to cook Chinese dishes.

Gabor (M) helped me a lot with the operation of his small “toy”, a powerful potentiostat to measure extremely low current. In addition, he gave me many useful suggestions on the design of EC cells, and the correction of EC data. Being the best gentleman I have ever met, Gabor also has a great sense of humor which I enjoyed very much.

 C. Acknowledgements

Thanks to our fair lady, Rocio, who remembers the birthdays for every of us. She made the air in Jülich full of joy and Tequila. I will be jealous of her new friends after she moves back to Mexico.

I wish to thank Prof. Robert de Levie, a teacher of both Thomas and me. During his visit in our group in 2002, Bob opened for me the first door to the world of electrochemistry with his introductory lectures. Best wishes to Bob and his new book.

My thanks go to Prof. Tamas Pajkossy from the Institute of Chemistry, Hungarian Academy of Sciences, Budapest, Hungary, and his colleague Dr. Gabriella Lendvay-Győrik for introducing to me the electrochemical impedance measurement. Especially, I am in debt of the thoughtful help from Gabi and her family, for taking care of us during my stay in Budapest and at the beautiful lake of Balaton.

I owe a lot help from Prof. Marcel Mayor and Dr. Alfred Błaszczyk from the Institute of Nanotechnology in Research Center Karlsruhe, Germany. They took great efforts to provide the precious viologen samples for my investigation. I hope I could find much better beer for Alfred's little pub in Poland.

Mr. Udo Linke from IBN-3 is especially acknowledged for the time and patience to prepare all types of gold single crystals. Without Udo sitting downstairs, I would have got much more trouble when the crystals are not lucky enough during flame annealing.

The assistance from Mr. Hermann J. Bierfeld from IFF is also important for my work. I couldn't really count how many times he has helped us to solve the problems with our pumps and the electron beam evaporation equipment.

I thank Prof. Antonio Rodes from the University of Alicante, for his valuable advice to improve the stability of our Au film electrodes, which helped me to overcome one of the greatest difficulties I experienced in my viologen experiments.

I thank Vladimir Stepanenko from the Institute of Organic Chemistry in the University of Würzburg, Germany, and Frank Amberger, Dr. Dirk Mayer from IBN-2 for their kind help in the AFM characterization of Au film electrodes.

My list of acknowledgments would not be complete without mentioning the other colleagues in the IBN-3/4. Prof. Harald Ibach and Prof. Rudolf Merkel are acknowledged for their organization work to create an interdisciplinary atmosphere in our institute. Special thanks to Ms. Sonja Körner, Ms. Marina Tödt, Mr. Hans Bernhard Ix and Ms. Mirjam Gruber who provided a lot of assistance in all sorts of administration problems. I also thank Mr. Friedhelm Schmitz, Mr. Wolfgang Rubner, and many others for the daily maintaining of our building and lab equipments.

Thanks for the help from the electronic workshop of Mr. Rainer Rausch, and the mechanical workshop of Mr. Dieter Strobl. Mr. Norbert Tiefes and Mr. Sascha Thiele are specially acknowledged for their patient help on the problems of our computers and network.

Special acknowledgements are given to the glassblowers in the glassware workshop. They are so skilful that almost any idea on a blueprint can be converted into real masterpieces of glass cells, containers, and connectors.

I thank Yinhua Han from IBN-2 for sharing her experience in writing with Microsoft Word, and the suggestions for the final procedures of my promotion. Best wishes for her future career in the US.

Equal thanks to Ms Janet Carter-Sigglow from the Central Library, for the timely help with the revision of the introduction part.

Thanks to Dr. Melanie Homberger from RWTH-Aachen, who is so nice an organizer for the interesting workshops, in which I came to know many new friends.

I would like to acknowledge the support and friendship of my friends in the Chinese community in Jülich. It is them who let me learn how to enjoy different types of lives, and made me feel like home in a country thousands of kilometers away from my hometown.

Finally, and most of all, this accomplishment is dedicated to my grandmother, my parents, and my girlfriend Yiyi, for their love, understanding, and continuous support of my curiosity of knowledge in the past and present. Their encouragement will give me all the enthusiasm and confidence in my future career.

The financial and academic supports from the Research Center Jülich (FZJ), the Volkswagen Foundation (VW-Stiftung), the Institute of Functional Molecular Systems for Information Technology (IFMIT), and the Center of Nanoelectronic Systems for Information Technology (CNI) are gratefully appreciated.

D. Publications during PhD Work

Li, Z.; Pobelov, I.; **Han, B.**; Wandlowski, T.; Błaszczyk, A.; Mayor, M.
"Conductance of redox-active single molecular junctions: an electrochemical approach"
NANOTECHNOLOGY, accepted on 31st October, 2006

Li, Z.; **Han, B.**; Meszaros, G.; Pobelov, I.; Wandlowski, T.; Błaszczyk, A.; Mayor, M.
"Two-dimensional assembly and local redox-activity of molecular hybrid structures in an electrochemical environment"
FARADAY DISCUSSION, 131: 121-143, 2006

Li, Z.; **Han, B.**; Wan, L. J.; Wandlowski, T.
"Supramolecular nanostructures of 1,3,5-benzene-tricarboxylic acid at electrified Au(111)/0.05 M H_2SO_4 interfaces: an in situ scanning tunneling microscopy study"
LANGMUIR, 21 (15): 6915-6928, 2005

Han, B.; Li, Z.; Pronkin, S.; Wandlowski, T.
"In situ ATR-SEIRAS study of adsorption and phase formation of trimesic acid on Au(111-25 nm) film electrodes"
CANADIAN JOURNAL OF CHEMISTRY-REVUE CANADIENNE DE CHIMIE, 82 (10): 1481-1494, 2004

E. Curriculum Vitae

Bo Han

Born on 02 January,1977, in Luoyang, Henan Province, China
Childhood and all school years in Wuhan, Hubei Province, China
Nationality: Chinese

Oct. 2002 ~ Dec. 2006, Ph.D. student

Institute of Bio- and Nanosystems, Research Center Jülich, Jülich
(PhD Promotion in RWTH-Aachen, Aachen)
Topic: *"Interfacial Electrochemistry and in situ SEIRAS Investigations of Self-Assembled Organic Monolayers on Au/Electrolyte Interfaces"*
Supervisors: Dr. Thomas Wandlowski, Prof. Dr. Ulrich Simon

Sept. 1999 ~ Aug. 2002, M.Sci. in Physical Chemistry

State Key Laboratory of Catalysis, Dalian Institute of Chemical Physics (Chinese Academy of Sciences), Dalian, China
Topic: *"UV Raman Characterization of Supported Vanadium Oxide Catalysts and Iron Substituted Zeolites"*
Supervisor: Prof. Can Li

Sept. 1995 ~ July 1999, B.Sci. in Chemical Physics

Department of Chemical Physics, University of Science and Technology of China, Hefei, China
Thesis: *"Sol-Gel Preparation and Characterization of Ultrafine Ni/Mo and Ni/Mg Composite Oxide Catalysts"*
Supervisors: Dr. Guo-zhu Bian, Prof. Yi-lu Fu

F. List of References

1 Lehn, J. -M. *Supramolecular Chemistry: Concepts and Perspectives*; Wiley-VCH: Weinheim, 1995.

2 Whitesides, G. M. *Science* **2002**, *295*, 2418.

3 Leininger, S.; Olenyuk, B.; Stang, P. J. *Chem. Rev.* **2000**, *100(3)*, 853.

4 Barth, J. V.; Costantini, G.; Kern, K. *Nature* **2005**, *437*, 671.

5 Desiraju, G. R. *Acc. Chem. Res.* **2002**, *35(7)*, 565.

6 Kaifer, A. E.; Gómez-Kaifer, M. *Supramolecular Chemistry*; Wiley-VCH: Weinheim, 1999.

7 Wandlowski, T. in *"Fundamentals of Nanoelectronics"*, Lectures of the 34th IFF Spring School; Jülich, 2003.

8 Heath, J. R.; Ratner, M. A. *Physics Today* **2003**, *May*, 43.

9 Moore, G. *Electronics Magazine* **1965**, *April*, 19.

10 Schmickler, W. *Interfacial electrochemistry*; University press: Oxford, 1996.

11 Finklea, H. O. *Electroanal. Chem.* **1996**, *19*, 109.

12 Bard, A. J.; Faulkner, L. R. *Electrochemical Methods: Fundamentals and Applications*, 2 ed.; John Wiley & Sons: New York, 2001.

13 Wandlowski, T.; Ataka, K.; Mayer, D. *Langmuir* **2002**, *18*, 4331.

14 a) Marcus, R. A. *J. Chem. Phys.* **1956**, *24*, 4966; b) Marcus, R. A. *J. Chem. Phys.* **1965**, *43(2)*, 679; c) Marcus, R. A. *Electrochem. Acta* **1968**, *13*, 955.

15 a) Hush, N. S. *J. Chem. Phys.* **1958**, *28*, 962; b) Hush, N. S. *Electrochem. Acta* **1968**, *13*, 1005.

16 Levich, V. G. *Adv. Electrochem. Electrochem. Eng.* **1966**, *4*, 249.

17 a) Gerischer, H. *Z. Phys. Chem. NF* **1960**, *6*, 223; b) Gerischer, H. *Z. Phys. Chem. NF* **1961**, *27*, 40, 48; c) Gerischer, H. *Annual Rev. Phys. Chem.* **1961**, *12*, 227.

18 Becka, A. M.; Miller, C. J. *J. Phys. Chem.* **1992**, *96*, 2657.

19 Ulman, A. *Chem. Rev.* **1996**, *96*, 1533.

20 Schreiber, F. *Progess in Surface Science* **2000**, *65*, 151.

21 Andreu, R.; Fawcett, W. R. *J. Phys. Chem. B* **1994**, *98*, 12753.

22 Forster, R. J. in *Encyclopedia of Electrochemistry*, Eds. Bard, A. J.; Stratmann, M. Vol. 3: *Instrumentation and Electroanalytical Chemistry*, Ed. Unwin, P.; Wiley-VCH: Weinheim, 2003.

23 Monk, P. M. S. *The Viologens*; John Wiley & Sons: Chichester, 1998.

24 Flink, S.; Van Veggel, F. C. J. M.; Reinhoudt, D. N. *Adv. Mater.* **2000**, *12*, 1315.

25 Love, J. C.; Estroff, L. A.; Kriebel, J. K.; Nuzzo, R. G.; Whitesides, G. M. *Chem. Rev*. **2005**, *105*, 1103.

26 Laviron, E. *J. Electroanal. Chem.* **1979**, *101*, 19.

27 Van Krieken, M.; Buess-Herman, C. *Electrochim. Acta* **1999**, *45*, 675.

28 Schultz, Z. D.; Gewirth, A. A. *Anal. Chem.* **2005**, *77*, 7373.

29 http://www.cheng.cam.ac.uk/research/groups/electrochem/JAVA/electrochemistry/ELEC/l4html/cv.html

30 Ataka, K.; Nishina, G.; Cai, W. -B.; Sun, S. -G.; Osawa, M. *Electrochem. Commun.* **2000**, *417*, 2.

31 Wandlowski, T. in *Encyclopedia of Electrochemistry*, Eds. Bard, A. J.; Stratmann, M. Vol. 1: *Thermodynamics and Electrified Interfaces*, Eds. Gileadi, E.; Urbakh, M.; Wiley-VCH: Weinheim, 2003.

32 Bewick, A.; Fleischmann, M.; Thirsk, H. R. *Trans. Faraday Soc.***1962**, *58*, 2200.

33 Christensen, P.; Hamnett, A. *Electrochim. Acta* **1999**, *45*, 2443.

34 Griffiths, P. R. in *Handbook of Vibrational Spectroscopy: Theory and Instrumentation*, Eds. Chalmers, J. M.; Griffiths, P. R.; John Wiley & Sons: Chichester, 2002.

35 Wandlowski, T.; Ataka, K.; Pronkin, S.; Diesing, D. *Electrochim. Acta*, **2004**, *49*, 1233.

36 Hartstein, A.; Kirtley, J. R.; Tsang, J. C. *Phys. Rev. Lett.* **1980**, *45*, 201.

37 Osawa, M.; Ataka, K.; Yoshi, K.; Nishikawa, Y. *Appl. Spect.* **1993**, *9*, 1497.

38 Suetaka, W. *Surface Infrared and Raman Spectroscopy: Methods and Applications*; Plenum Press: New York, 1995.

39 Hatta, A.; Ohshina, T.; Suetaka, W. *Appl. Phys. A* **1982**, *121*, 71.

40 Osawa, M. *Bull. Chem. Soc. Jpn.* **1997**, *70*, 2861.

41 Anderson, M. R.; Taylor, C. D. in *Encyclopedia of Analytical Chemistry, Applications, Theory, and Instrumentation,* Vol. 11. Eds. Meyers, R. A.; John Wiley & Sons: New York, 2000.

42 Hatta, A.; Sasaki, Y.; Suetaka, W. *J. Electroanal. Chem. Interfacial Electrochem.* **1986**, *215(1-2)*, 93.

43 Osawa, M.; Ikeda, M. *J. Phys. Chem.* **1991**, *95*, 9914.

44 Klibanov, A.; Gheorghiu, M. *MIT's Open Course Ware: Intermediate-Chemical-ExperimentationSpring2003, Qualitative Organic Analysis, Appendix 1: Instrumentation.* http://ocw. mit. edu/NR/rdonlyres/Chemistry/

45 Li, Z.; Han, B.; Wandlowski, T. *Langmuir* **2005**, *21*, 6915.

46 Kern, W. *J. Electrochem. Soc.*, **1990**, *137*, 1887.

47 Hölzle, M. H.; Wandlowski, T.; Kolb, D. M. *J. Electroanal. Chem.* **1995**, *394*, 271.

48 Paikossy, T.; Wandlowski, T.; Kolb, D. M. *J. Electroanal. Chem*. **1996**, *414*, 209.

49 Meszaros, G.; Wandlowski, T.; Wu, Z.; Han, B. *Rev. Sci. Instr.* in preparation.

50 Christensen, P. A.; Hamnett, A. *Techniques and Mechanisms in Electrochemistry*; Chapman & Hall: Glasgow, 1994.

51 Lide, D. R. (Editor-in-chief) *Handbook of Chemistry and Physics*, 82nd Edition; CRC Press: Boca Raton, 2001.

52 Hartwell, J. L.; Pogorelskin, M. A. *J. Am. Chem. Soc.* **1950**, *72*, 2040.

53 a) Haiss, W.; Van Zalinge, H.; Higgins, S. J.; Bethell, D.; Hörbenreich, H.; Schiffrin, D. J.; Nichols, R. J. *J. Am. Chem. Soc.* **2003**, *125*, 15294; b) Haiss, W.; Nichols, R. J.; Van Zalinge, H.; Higgins, S. J.; Bethell, D.; Schiffrin, D. J. *Phys. Chem. Chem. Phys.* **2004**, *6*, 4330.

54 Pearson, A. J.; Hwang, J. J. *J. Org. Chem.* **2000**, *65*, 3466.

55 Scherson, D. A.; Kolb, D. M. *J. Electroanal. Chem.* **1984**, *176*, 353.

56 a) Angerstein-Kozlowski, H.; Conway, B. E.; Hamelin, A.; Stoicoviciu, L. *Electrochim. Acta* 1986, 31, 1051; b) Angerstein-Kozlowski, H.; Conway, B. E.; Hamelin, A.; Stoicoviciu, L. *J. Electroanal. Chem.* **1987**, *228*, 429.

57 Sato, K.; Yoshimoto, S.; Inukai, J.; Itaya, K. *Electrochem. Commun.* **2006**, *8*, 725.

58 Shi, Z.; Lipkowski, J.; Mirwald, S.; Pettinger, B. *J. Electroanal. Chem.* **1995**, *396*, 115.

59 Lipkowski, J.; Shi, Z.; Chen, A.; Pettinger, B.; Bilger, C. *Electrochim. Acta*, **1998**, *43*, 2875.

60 Lipkowski, J.; Wieckowski, A. *J. Electroanal. Chem.* **2001**, *504*, 230.

61 Shi, Z.; Lipkowski, J.; Gamboa, M.; Zelenay, P.; Wieckowski, A. *J. Electroanal. Chem.* **1994**, *366*, 317.

62 Zei, M. S.; Scherson, D.; Lehmpfuhl, G.; Kolb, D. M. *J. Electroanal. Chem.* **1987**, *229*, 99.

63 Zei, M. S.; Qiao, G.; Lehmpfuhl, G.; Kolb, D. M. *Ber. Bunsenges. Phys. Chem.* **1987**, *91*, 349.

64 Mrozek, P.; Han, M.; Sung, Y. E.; Wieckowski, A. *Surf. Sci.* **1994**, *319*, 21.

65 Uchida, H.; Ikeda, N.; Watanabe, M. *J. Electroanal. Chem.* **1997**, *424*, 5.

66 Magnussen, O. M.; Hageböck, J.; Hotlos, J.; Behm, R. J. *Farad. Discuss.* **1992**, *94*, 329.

67 Edens, G. J.; Gao, X.; Weaver, M. J. *J. Electroanal. Chem.* **1994**, *375*, 357.

68 Inukai, J.; Sugita, S.; Itaya, K. *J. Electroanal. Chem.* **1996**, *403*, 159.

69 Drestchkow, T.; Wandlowski, T. *Ber. Bunsenges. Phys. Chem.* **1997**, *101*, 749.

70 Nishizawa, T.; Nakata, T.; Kinoshita, Y.; Miyashita, S.; Sazaki, G.; Komatsu, H. *Surf. Sci.* **1996**, *367*, L73.

71 Cuesta, A.; Kleinert, M.; Kolb, D. M. *Phys. Chem. Chem. Phys.* **2000**, *2*, 5684.

72 Ataka, K.; Osawa. M. *Langmuir* **1998**, *14*, 951

73 Shingaya, Y.; Ito, M. *Electrochim. Acta* **1998**, *44*, 745.

74 Moraes, I. R.; Nart, F. C. *J. Electroanal. Chem.* **1999**, *461*, 110.

75 Ataka, K.; Yoshimoto, T.; Osawa, M. *J. Phys. Chem.* **1996**, *100*, 10664.

76 Futamata, M. *Surf. Sci.* **1999**, *427-428*, 179

77 Scherrer, J. R. in *Advances in Infrared and Raman Spectroscopy*, Vol. 5, Eds. Clark, R. J. H.; Hesters, R. E.; Heyden: Philadelphia, 1978.

78 Nakamoto, K. *Infrared and Raman Spectra of Inorganic and Coordination Compounds*, 4th ed.; Wiley-VCH: New York, 1986.

79 Tanaka, N.; Sugi, H.; Fujita, J. *Bull. Chem. Soc. Jpn.* **1964**, *37*, 640.

80 Iwasita, T.; Nart, F. C. *Progr. Sur. Sci.* **1997**, *55*, 271.

81 Shingaya, Y.; Ito, M. *J. Electroanal. Chem.* **1999**, *467*, 299.

82 Nakamura, M.; Shingaya, Y.; Ito, M. *Surf. Sci.* **2002**, *502-503*, 474.

83 Patrito, E. M.; Paredes-Olivera, P.; Sellers, H. *Surf. Sci.* **1997**, *380*, 264.

84 Paredes-Olivera, P.; Patrito, E. M.; Sellers, H. *Surf. Sci.* **1998**, *418*, 376.

85 Korzeniewski, C. in *Interfacial Electrochemistry. Theory, Experimental and Applications*, Ed. Wieckowski, A.; Marcel Dekker: New York, 1999.

86 Spohr, E. in *Advances in Electrochemical Science and Engineerng*, Eds. Alkire, R. C.; Kolb, D. M. , Vol. 6; Wiley-VCH: Weinheim, 1999.

87 Bailey, M.; Brown, C. J. *Acta Crystallogr.* **1967**, *B 22*, 387.

88 Alcala, R.; Martinez-Carrera, S. *Acta Crystallogr.* **1972**, *B 25*, 1671.

89 De Feyter, S.; Gesquiere, A.; Abdel-Mottaleb, M. M.; Grim, P. C. M.; De Shryver, F. C.; Meiners, C.; Sieffert, M.; Valiyaveettil, S.; Müllen, K. *Acc. Chem. Res*. **2000**, *33*, 520.

90 Melendres, R.; Hamilton, A. D. *Topics Current Chem.* **1998**, *197*, 97.

91 Duchamp, D. J.; March, R. E. *Acta Crystallogr.* **1969**, *B 25*, 5.

92 Herbstein, F. H. in *Comprehenive Supramolecular Chemistry*, Vol. 6, Eds. Atwood, J. L.; MacNico, D. D.; Vögtle, D. D.; Lehn, J. M.; Pergamon: New York, 1996.

93 Kolotuchin, S. V.; Thiessen, P. A.; Fenlon, E. E.; Wilson, S. R.; Loweth, C. J.; Zimmerman, S. C. *Chem. Eur. J.* **1999**, *5(9)*, 2537.

94 Chatterjee, S.; Pedireddi, V. R.; Ranganathan, A.; Rao, C. N. R. *J. Mol. Struct.* **2000**, *520*, 107.

95 Barth, J. V.; Wechesser, J.; Lin, N.; Dmitriev, A.; Kern, K. *Appl. Phys.* **2003**, *A 76*, 645.

96 Ermer, O.; Neudörfl, J. *Chem. Eur. J.* **2001**, *7*, 4961.

97 Dai, J. C.; Hu, S. M.; Wu, X. T.; Fu, Z. Y.; Du, W. X.; Zhang, H. H.; Sun R. Q. *New J. Chem.* **2003**, *27*, 94.

98 Yang, L.; Naruke, H.; Yamase, T. *Inorganic Chem. Commun.* **2003**, *6*, 1020.

99 Kolotuchin, S. V.; Fenlon, E. E.; Wilson, S. R.; Loweth, C. J.; Zimmerman, S. C. *Angew. Chem. Int. Ed. Engl.* **1995**, *34*, 2654.

100 Melendez, R. E.; Shrama, C. V. K.; Zaworotko, M. J.; Bauer, C.; Rogers, R. D.; *Angew. Chem. Int. Ed. Engl.* **1996**, *35*, 2213.

101 Shrama, C. V. K.; Zaworotko, M. J. *Chem. Commun.* **1996**, 2655.

102 Lin, N.; Dmitriev, A.; Weckesser, J.; Barth, J. V.; Kern, K. *Angew. Chem. Int. Ed. Engl.* **2002**, *41*, 4779.

103 Messina, P.; Dmitriev, A.; Lin, N.; Spillmann, H.; Abel, M.; Barth, J. V.; Kern, K. *J. Am. Chem. Soc.* **2002**, *124*, 14000.

104 Griessl, S.; Lackinger, M.; Edelwirth, M.; Hietschold, M.; Heckl, W. M. *Single Mol.* **2002**, *3*, 25.

105 Dmitriev, A.; Lin, N.; Weckesser, J.; Barth, J. V.; Kern, K. *J. Phys. Chem. B* **2002**, *106*, 6907.

106 Ishikawa, Y.; Ohira, A.; Sakata, M.; Hirayama, C.; Kunitake, M. *J. Chem. Soc. , Chem. Commun.* **2002**, 2652.

107 Su, G. J.; Zhang, H. M.; Wan, L. J.; Bai C. L.; Wandlowski, T. *J. Phys. Chem. B* **2004**, *108*, 1931.

108 Ikezawa, Y.; Sekiguchi, R.; Kitazume, T. *Electrochim. Acta* **2000**, *46*, 731.

109 Li, H. -Q.; Roscoe, S. G.; Lipkowski, J. *J. Electroanal. Chem*. **1999**, *478*, 67.

110 Ikezawa, Y.; Yoshida, A.; Sekiguchi, R. *Electrohcim. Acta* **2000**, *46*, 769.

111 Lee, M. W.; Kim, M. S.; Kim, K. *J. Mol. Struct.* **1997**, *415*, 93.

112 Osawa, M. in *Handbook of Vibrational Spectroscopy*, Vol. 1: *Theory and Instrumentation*, Eds. Chalmers, J. M.; Griffiths, P. R.; Wiley-VCH: Chichester, 2002.

113 Noda, H.; Ataka, K.; Wan, L. -J.; Osawa, M. *Surf. Sci.* **1999**, *427-428*, 190.

114 Noda, H.; Wan, L. -J.; Osawa, M. *Phys. Chem. Chem. Phys.* **2001**, *3*, 3336.

115 Ataka, K.; Osawa, M. *J. Electroanal. Chem.* **1999**, *460*, 188.

116 Pronkin, S.; Wandlowski, T. *J. Electroanal. Chem.* **2003**, *550-551*, 131.

117 Arenas, J. F.; Marcos, J. I. *Spectrochimica Acta* **1979**, *35A*, 355.

118 Gonzalez-Sanchez, F. *Spectrochimica Acta* **1957**, *12*, 17.

119 Ataka, K.; Yotsuyanagi, T.; Osawa, M. *J. Phys. Chem.* **1996**, *100*, 10664.

120 Ataka, K; Osawa, M. *Langmuir* **1998**, *14*, 951.

121 Corrigan, D. S.; Weaver, M. J. *Langmuir* **1988**, *4*, 599.

122 Frederick, B. G.; Chen, Q.; Barlow, S. M.; Condon, N. G.; Leibsle, F. M.; Richardson, N. V. *Surf. Sci.* **1996**, *352-354*, 238.

123 Frederick, B. G.; Chen, Q.; Leibsle, F. M.; Lee, M. B.; Kitching, K. J.; Richardson, N. V. *Surf. Sci.* **1997**, *394*, 1.

124 De Feyter, S.; De Schryver, F. C. *Chem. Soc. Rev.* **2003**, *32*, 139.

125 Nichols, R. in: (Eds.), *Adsorption of Molecules at Electrodes*, Eds. Lipkowski, J. Ross P. N.; Wiley-VCH: New York, 1992.

126 Dean, J. A. in Lange´s *Handbook of Chemistry*, McGraw-Hill, 13th ed. , 5-42.

127 Li, Z.; Han, B. to be submitted.

128 Li, H. -Q.; Roscoe, S. G.; Lipkowski, J. *J. Solution Chem.* **2000**, *29*, 987.

129 Bird, C. L.; Kuhn, A. T. *Chem. Soc. Rev.* **1981**, *10*, 49.

130 a) Terrill, R. H.; Hutchison, J. E.; Murray, R. W. *J. Phys. Chem. B* **1997**, *101(9)*, 1535; b) Jernigan, J. C.; Surridge, N. A.; Zvanut, M. E.; Silver, M.; Murray, R. W. *J. Phys. Chem.* **1989**, *93*, 4620; c) Dalton, E. F.; Murray, R. W. *J. Phys. Chem.* **1991**, *95*, 6383.

131 a) Liu, X.; Neoh, K. G.; Cen, L.; Kang, E. T. *Biosensors & Bioelectronics* **2004**, *19(8)*, 823; b) Wang, X. J.; Dzyadevych, S. V.; Chovelon, J. M.; Renault, N. J.; Chen, L.; Xia, S. Q.; Zhao, J. F. *Electrochem. Commun.* **2006**, *8(2)*, 201; c) Juan, Z.; Swager, T. M. *Advances in Polymer Science* **2005**, *177*, 151.

132 Haramoto, Y.; Yin, M.; Matukawa, Y.; Ujiie, S.; Nanasawa, M. *Liquid Crystals* **1995,** *19(3)*, 319.

133 Willner, I.; Eichen, Y.; Frank, A. J.; Fox, M. A. *J. Phys. Chem.* **1993**, *97(28)*, 7264.

134 Sagara, T.; Kato, N.; Toyota, A.; Nakashima, N. *Langmuir* **2002**, *18(18)*, 6995.

135 Yang, C. H.; He, G. F.; Wang, R. Q.; Li, Y. F. *Thin Solid Films* **2000,** *363(1-2)*, 218.

136 Haiss, W.; Van Zalinge, H.; Hörbenreich, H.; Bethell, D.; Schiffrin, D. J.; Higgins, S. J.; Nichols, R. J. *Langmuir* **2004**, *20*, 7694.

137 Gittins, D. I.; Bethell, D.; Schiffrin, D. J.; Nichols, R. J. *Nature* **2000**, *408*, 67.

138 a) Raymo, F. M.; Alvarado, R. J.; Pacsial, E. J.; Alexander, D. *J. Phys. Chem. B* **2004**, *108*, 8622; b) Raymo, F. M.; Alvarado, R. J.; Pacsial, E. J.; *J. Supramol. Chem.* **2002**, *2*, 63; c) Raymo, F. M.; Alvarado, R. J.; Giordani, S.; Cejas, M. A. *J. Am. Chem. Soc.* **2003**, *125*, 2361.

139 Alvarado, R. J.; Mukkerjee, J.; Pacsial, E. J.; Alexander, D.; Raymo, F. M. *J. Phys. Chem. B* **2005**, *109(13)*, 6164.

140 a) De Long, H. C.; Buttry, D. A. *Langmuir* **1990**, *6*, 1319; b) De Long, H. C. Buttry, D. A. *Langmuir* **1992**, *8*, 2491; c) Hiley, S. L. Buttry, D. A. *Colloids and Interfaces A* **1994**, *84*, 129.

141 a) Sagara, T.; Maeda, H.; Yuan, Y.; Nakashima, N.; *Langmuir* **1999**, *15*, 3823; b) Sagara, T.; Kaba, N.; Komatsu, M.; Uchida, M.; Nakashima, N.; *Electrochim. Acta* **1998**, *43*, 2183; c) Sagara, T.; Tsuruta, H.; Nakashima, N. *J. Electroanal. Chem.* **2001**, *500*, 255; d) Wang, H. X.; Sagara, T.; Sato, H.; Niki, K. *J. Electroanal. Chem.* **1992**, *331(1-2)*, 925.

142 a) Sagara, T.; Miuchi, K. *J. Electroanal. Chem.* **2004**, *567(2)*, 193; b) Sagara, T.; Tanaka, S.; Fukuoka, Y.; Nakashima, N. *Langmuir* **2001**, *17(5)*, 1620; c) Sagara, T.; Tanaka, S.; Miuchi, K.; Nakashima, N. *J. Electroanal. Chem.* **2002**, *524-525*, 68.

143 a) John, S. A.; Kitamura, F.; Tokuda, K.; Ohsaka, T. *Electrochim. Acta* **2000**, *45(24)*, 4041; b) John, S. A.; Kitamura, F.; Tokuda, K.; Ohsaka, T. *J. Electroanal. Chem.* **2000**, *492(2)*, 137; c) John, S. A.; Okajima, T.; Ohsaka, T. *J. Electroanal. Chem.* **1999**, *466(1)*, 67; d) John, S. A.; Kasahara, H.; Okajima, T.; Tokuda, K.; Ohsaka, T. *J. Electroanal. Chem.* **1997**, *436(1-2)*, 267; e) John, S. A.; Kitamura, F.; Tokuda, K.; Ohsaka, T. *Langmuir* **2000**, *16(2)*, 876; f) John, S. A.; Ohsaka, T. *Electrochim. Acta* **1999**, *45(7)*, 1127; g) Arihara, M.; Kitamura, F.; Nukanobu, K.; Ohsaka, T.; Tokuda, K. *J. Electroanal. Chem.* **1999**, *473(1-2)*, 138.

144 a) Kim, J. H.; Lee, K. A. B.; Uphaus, R. A.; Cotton, T. M. *Thin Solid Films* **1992**, *210-211*, 825; b) Lu, T.; Cotton, T. M.; Hurst, J. K.; Thompson. D. H. P. *J. Phys. Chem.* **1988**, *92*, 6978; c) Lu, T.; Cotton, T. M.; Hurst, J. K.; Thompson, D. H. P. *J. Electroanal. Chem.* **1988**, *246*, 337.

145 a) Tang, X.; Schneider, T. W.; Buttry, D. A.; *Langmuir*, 1994, *10*, 2235; b) Tang, X.; Schneider, T. W.; Walker, J. W.; Buttry, D. A. *Langmuir*, **1996**, *12*, 5921.

146 a) Osawa, M.; Yoshii, K. *Applied Spectroscopy* **1997**, *51(4***)**, 512; b) Osawa, M. Suëtaka, W. *J. Electroanal. Chem.* **1989**, *270*, 261; c) Osawa, M. Yoshii, K. Ataka, K. Yotsuyanagi, T. *Langmuir* **1994**, *10(3)*, 640.

147 a) Ito, M. Sasaki, H. Takahashi, M. *J. Phys. Chem.* **1987**, *91*, 3932; b) Sasaki, H. Takahashi, M. Ito, M. *Journal of electron Spectroscopy and related phenomena* **1987**, *45*, 161.

148 Li, J.; Chen, G.; Dong, S. *Thin Solid Films* **1997**, *293*, 200.

149 a) Lee, C.; Moon, M. S.; Park, J. W. *J. Electroanal. Chem.* **1996**, *407*, 161; b) Lee, C.; Lee, Y. M.; Moon, M. S.; Park, S. H.; Park, J. W.; Kim, K. G.; Jeon, S. J. *J. Electroanal. Chem.* **1996**, *416*, 139.

150 a) John, S. A.; Ohsaka, T. *J. Electroanal. Chem.* **1999**, *477(1)*, 52; b) Lee, C.; Lee, Y. K.; Lee, Y. M.; Jeon, I. C. *J. Electroanal. Chem.* **1999**, *463*, 224.

151 Li, Z.; Han, B.; Meszaros, G.; Pobelov, I.; Wandlowski, T.; Błaszczyk, A.; Mayor, M. *Faraday Discussion* **2006**, *131*, 121.

152 Anson, F. C.; Blauch, D. N.; Saveant, J. M.; Shu, C. F. *J. Am. Chem. Soc.* **1991**, *113*, 1922.

153 Saveant, J. M. *J. Phys. Chem.* **1988**, *92*, 4526.

154 Monk, P. M. S.; Hodgkinson, N. M. *Electrochim. Acta* **1998**, *43(3-4)*, 245.

155 Creager, S. E.; Rowe, G. K. *Analytica Chimica Acta* **1991**, *246*, 233.

156 Chidsey, C. E. D.; Bertozzi, C. R.; Putvinski, T. M.; Mujsce, A. M. *J. Am. Chem. Soc.* **1990**, *112(11)*, 4301.

157 Widrig, C. A.; Chung, C.; Porter, M. D. *J. Electroanal. Chem.* **1991**, *335*, 310.

158 Kobayashi, K.; Fujisaki, F.; Yoshime, T.; Niki, K. *Bull. Chem. Soc. Jpn.* **1986**, *59*, 3715.

159 Russell, J. H.; Wallwork, S. C. *Acta. Cryst. B* **1972**, *28*, 1527.

160 Polishchuk, I. Y.; Grineva, L. G.; Polishchuk, A. P.; Chernega, A. N. *Russian Journal of General Chemistry* **1996**, *66*, 1530.

161 Esplandiú, M. J.; Hagenström, H.; Kolb, D. M. *Langmuir* **2001**, *17*, 828.

162 Cabrita, J. F.; Abrantes, L. M.; Viana, A. S. *Electrochim. Acta.* **2005**, *50*, 2117.

163 Arihara, K.; Kitamura, F. *J. Electroanal. Chem.* **2003**, *550*, 149.

164 a) Brienne, S. H. R.; Cooney, R. P.; Bowmaker, G. A. *J. Chem. Soc. Farad. Trans.* **1991**, *87(9)*, 1355; b) Brienne, S. H. R.; Boyd, P. D. W.; Schwerdtfeger, P.; Bowmaker, G. A.; Cooney, R. P. *J. Chem. Soc. Farad. Trans.* **1993**, *89(16)*, 3015.

165 a) Ghostal, S.; Lu, T.; Feng, Q.; Cotton, T. M. *Spectroelectrochim. Acta*, **1988**, *44A*, 651; b) Hester, R. E.; Suzuki, S. *J. Phys. Chem.* **1982**, *86*, 4626.

166 a) Duan, L.; Garrett, S. J. *Langmuir* **2001**, *17(10)*, 2986; b) Reipa, V.; Yeh, S. -M. L.; Monbouquette, H. G.; Vilker, V. L. *Langmuir* **1999**, *15(23)*, 8126.

167 Rong, H. T.; Frey, S.; Yang, Y. J.; Zharnikov, M.; Buck, M.; Wühn, M.; Wöll, C.; Helmchen, G. *Langmuir* **2001**, *17*, 1582.

168 a) Fujii, A.; Fujimaki, E.; Ebata, T.; Mikami, N. *J. Chem. Phys.* **2000**, *112(14)*, 6275; b) Briscoe, B. J.; Stuart B. H.; Thomas, P. S.; Williams, D. R. *Spectrochimica Acta A: Molecular Spectroscopy* **1999**, *47(9-10)*, 1299; c) Yu, K. H.; Rhee, J. M.; Lim, J. -H.; Yu, S. -C. *Bull. Korean Chem. Soc.* **2002**, *23(4)*, 633.

169 Porter, M. D.; Bright, T. B.; Allara, D. L.; Chidsey, C. E. D. *J. Am. Chem. Soc.* **1987**, *109*, 3559.

170 Nuzzo, R. G.; Dubois, L. H.; Allara, D. L. *J. Am. Chem. Soc.* **1990**, *112(2)*, 558.

171 a) Poirier, G. E. *Langmuir* **1997**, *13*, 2019; b) Poirier, G. E. *Langmuir* **1999**, *15*, 1167; c) Yang, G.; Liu, G. *J. Phys. Chem. B* **2003**, *107*, 8746.

172 a) Ulman, A.; Scaringe, R. P. *Langmuir* **1992**, *8(3)*, 894 (1992); b) Shnidman, Y.; Ulman, A.; Eilers, J. E. *Langmuir* **1993**, *9(4)*, 1071.

173 Andrieux, C. P.; Hapiot, P.; Saveant, J. -M. *Electroanalysis* **1990**, *2*, 183.

174 a) Montennegro, M. I.; Queirós, M. A.; Daschbach, J. L. *Microelectrodes: Theory and Applications*, Kluwer: 1991; b) Heinze, J. *Angew. Chem. Int. Ed. Engl.* **1993**, *32*, 1268.

175 Miller, C. J.; Cuendet, P.; Graetzel, M. *J. Phys. Chem.* **1991**, *95(2)*, 877.

176 Majda, M. in: *Molecular Design of Electrode Surfaces*, Ed. Murray, R. W., *Techniques of Chemistry Series*, Vol XXII. John Wiley & Sons: 1992.

Forschungszentrum Jülich
in der Helmholtz-Gemeinschaft

50 Jahre / Zukunft

Jül-4236
Dezember 2006
ISSN 0944-2952